

Enhancement of Tensile Fracture Resistance of Metal-Injection-Molded β Titanium Alloys Biomaterials via Diverse Sintering Pathways

Von der Fakultät für Maschinenbau, Elektro- und Energiesysteme
der Brandenburgischen Technischen Universität Cottbus–Senftenberg
zur Erlangung des akademischen Grades eines
Doktor der Ingenieurwissenschaften

genehmigte Dissertation

vorgelegt von

Master of Engineering

Peng Xu

geboren am 05, October 1990 in Mudanjiang, Heilongjiang, P.R. China

Vorsitzender: Prof. Markus Bambach

Gutachter: Prof. Florian Pyczak

Gutachterin: Prof. Sabine Weiß

Tag der mündlichen Prüfung: 12, Februar 2021

DOI: 10.26127/BTUOpen-5512

Acknowledgements

There are many people I want to thank for their support and effort. This contribution means a great deal not only to my Ph.D. thesis, but also to my personal development.

First and foremost, I would like to express my sincere appreciation to my supervisor Dr. Thomas Ebel, head of Powder Based Materials Development department, for his patience, encouragement and instruction to me during the whole Ph.D. study in Helmholtz-Zentrum Hereon (Geesthacht). His personality and charisma inspire me to devote myself to learning and innovation. He always makes me interested in, and hungry for, technology research. My regards also to my second supervisor, Prof. Pyczak Florian, who is head of Metal Physics department. He is an enthusiastic, thoughtful and insightful advisor. He has given me critical guidance and valuable suggestions for my research work and paper publication.

In addition, I would like to thank Dr. Andreas Stark for the support in the *in situ* high-energy X-ray diffraction experiments at the synchrotron beamline; Petra Fischer for the assistance in electron backscatter diffraction; Wolfgang Limberg, Andreas Dobernowsky, Dr. Jonathan Paul, Kay Erdmann, Stefan Riekehr and Dirk Matthiessen for their technical help in metal injection molding, tensile tests and impurities determination; Dr. Alexandra Hidalgo for familiarizing me with the operation of various basic experimental facilities; Prof. Regine Willumeit-Römer, Prof. Ming Yan and Prof. Fantao Kong for reviewing my journal papers; Christopher Gloeckle for language polishing. Many thanks also to other colleagues in Helmholtz-Zentrum Hereon.

Here the China Scholarship Council (CSC) program is acknowledged for my scholarship funding.

Finally yet also importantly, I want to thank my parents for giving me life and raising me. Their love is great and allowed me to pursue my dreams without any worries. Thanks also goes to my girlfriend, cousins and friends for their concern and comfort.

We are in a very difficult period at the moment. The COVID-19 virus is sweeping across the world. But I firmly believe that we can overcome all obstacles eventually. We will see the black clouds fade and the sun shine all over Germany again in short future.

Abstract (in English)

The powder metallurgically produced β titanium alloys (traditional PM β Ti-alloys) have long been plagued by high impurities contamination. For binder-based powder technologies, they originate from the sintering atmosphere, the debinding processes and the starting powders. In general, a normal carbon residual of binder-based powder technologies is capable of incurring the formation of aligned TiC_x particles along β grain boundaries (GB- TiC_x) in most classes of β Ti-alloys. Whereas, oxygen atoms are likely to deteriorate the ductility of PM Ti alloys by promoting the formation of diverse brittle phases and/or altering the deformation modes. Such materials exhibiting rather low toughness to strain ratios are not an option for critical structural applications, where catastrophic damage is completely unacceptable.

In this study, biotolerant metastable β Ti-20Nb-10Zr alloys, containing a certain amount of carbon, oxygen residuals originated from materials processing and consequently 0.5 vol.% *in situ* synthesized TiC_x particles, were fabricated via metal-injection-molding (MIM). With varying yttrium (Y) addition, the effects of Y-induced oxygen scavenging, β -grain refinement and porosity increment on tensile properties were systematically investigated. To scavenge oxygen from the β Ti-matrix, the Y elemental powder with a maximum particle size of 15 μm (e.g. <12 μm or 1200 mesh) is more appropriate than the commonly used <45 μm (i.e. 325 mesh) sized powder or larger ones and without significant detrimental effect on the as-sintered density of β Ti-alloys.

A novel toughening strategy was proposed by regulating TiC_x precipitation evolution and resultantly adjusting particles distribution pattern. Synchrotron radiation identified that two separate TiC_x precipitation-type reactions occurred at the β phase region and the α/β region. In a narrow temperature range between these two precipitation reactions, dissolution of carbides was observed just below α/β transus. Y addition can postpone TiC_x precipitation. On the basis of those mechanisms, adjusting TiC_x particle distribution was proposed for the first time, specifically a combination of yttrium addition (Y) and carbide spheroidization reprecipitation annealing (CSRA). As a result, aligned GB- TiC_x particles were adjusted to dispersed intragranular TiC_x particles. An apparent toughening effect ($\approx 113\%$ increment reaching $\epsilon_f = 8.3\%$) was achieved after TiC_x redistribution, while non-optimally aligned TiC_x pattern seriously limited tensile toughness of materials. Here, the mechanisms of TiC_x redistribution behavior and its toughening are elucidated systematically.

Zusammenfassung (auf Deutsch)

Die pulvermetallurgisch hergestellten β -Legierungen (d. h. Titanlegierungen der β -Klasse) leiden seit Langem unter hohen Verunreinigungsgraden. Für Pulvertechnologien auf Bindemittelbasis stammen diese Verunreinigungen aus der Sinteratmosphäre, dem Entbinderungsprozess und den Ausgangspulvern. Im Allgemeinen kann ein normalerweise verbleibender Kohlenstoffrest von Pulvertechnologien auf Bindemittelbasis in den meisten Klassen von β -Legierungen zur Bildung ausgerichteter TiC_x -Partikel entlang früherer β -Korngrenzen (GB- TiC_x) führen, während Sauerstoffatome wahrscheinlich die Duktilität von PM-Ti-Legierungen verschlechtern, indem sie die Bildung verschiedener spröder Phasen fördern und / oder die Verformungsmodi verändern. Solche Materialien mit relativ niedrigen Zähigkeits zu Dehnungs Verhältnissen sind keine Option für kritische strukturelle Anwendungen, bei denen katastrophale Schäden völlig inakzeptabel sind.

In dieser Studie wurden biotolerante metastabile β -Ti-20Nb-10Zr-Legierungen, die eine bestimmte Menge Kohlenstoff, Sauerstoffreste und folglich 0,5 Vol.% in situ synthetisierte TiC_x -Partikel als zusätzliche Phase enthielten, mittels Metallspritzguss (MIM) hergestellt. Bei variierender Yttrium (Y)-Zugabe wurden die Auswirkungen der Y-induzierten Sauerstoffbindung, der Verfeinerung der Mikrostruktur und der Erhöhung der Porosität auf die Zugeigenschaften systematisch untersucht. Um Sauerstoff aus der β -Ti-Matrix abzufangen, ist das Y-Elementpulver mit einer maximalen Partikelgröße von weniger als 15 μm (z. B. 12 μm oder 1200 mesh) geeigneter als das üblicherweise verwendete Pulver mit einer Größe von 45 μm (325 mesh) oder größer und ohne signifikante nachteilige Auswirkung auf die Sinterdichte von β titanium-Legierungen.

Eine neuartige Härtingsstrategie wurde vorgeschlagen, indem die Entwicklung der TiC_x -Ausscheidungen reguliert und das Partikelverteilungsmuster angepasst wurden. Mit Synchrotronstrahlung wurde festgestellt, dass zwei getrennte TiC_x -Ausscheidungsreaktionen im β -Phasenbereich und im α/β -Bereich auftraten. In einem engen Temperaturbereich zwischen diesen beiden Ausscheidungsreaktionen wurde eine Auflösung von Carbiden knapp unterhalb des α/β -Transus beobachtet. Die Zugabe von Y kann die TiC_x -Ausscheidung verzögern. Auf der Grundlage dieser Mechanismen wurde erstmals eine Anpassung der TiC_x -Partikelverteilung vorgeschlagen, insbesondere eine Kombination aus Yttrium-addition (Y) und Carbidsphäroidisierungs-Umfällungsglügen (CSRA). Als Ergebnis wurden ausgerichtete GB- TiC_x -

Partikel in homogen verteilte intragranulare TiC_x -Partikel umgewandelt. Eine offensichtliche Verbesserung der Duktilität ($\sim 113\%$ Zunahme entsprechend $\varepsilon_f = 8,3\%$) wurde nach TiC_x -Umverteilung erreicht, während eine nicht optimal verteilte TiC_x -Population die Zugzähigkeit von Materialien stark einschränkte. Hier werden die Mechanismen der TiC_x -Umverteilung und ihre Auswirkungen auf die Duktilität und Zähigkeit systematisch aufgeklärt.

Contents

1.	Introduction	1
2.	State of the art	3
2.1	Development and application of β Ti-alloys	3
2.1.1	Development status	3
2.1.2	Applications	6
2.2	Powder metallurgy route	11
2.2.1	Overview of powder metallurgy Ti-alloys	11
2.2.2	Starting powder of β Ti-alloys	13
2.2.3	Metal injection molding (Ti-MIM)	15
2.2.4	Fusion powder technologies (non-sintered Ti-alloys)	16
2.3	Major processing defects of MIM β Ti-alloys	17
2.3.1	Residual porosity	18
2.3.2	Coarse-grained structure	20
2.3.3	Interstitial impurities levels	22
2.4	Advanced sintering pathways	28
2.4.1	RE-containing sintering cycle	28
2.4.2	Boron-containing sintering cycle and its particle distributions	30
3.	Experimental	32
3.1	Alloy design and nomenclature	32
3.2	Materials processing	33
3.2.1	Starting materials	33
3.2.2	Polymeric binder system	34
3.2.3	Feedstocks preparation	35
3.2.4	Metal injection molding (MIM)	35
3.2.5	Chemical debinding (1st step)	35
3.2.6	Thermal debinding (2nd step) and sintering	36
3.2.7	Traditional press-and-sintering	37
3.3	Materials tests and characterization	37
3.3.1	Mechanical properties tests	37
3.3.2	Interstitial levels determination	38
3.3.3	Porosity / relative density	38
3.3.4	Microstructural characterization	39
3.3.5	<i>In situ</i> high energy X-ray diffraction (synchrotron)	40
4.	Results	41
4.1	Y-containing sintering cycle of MIM β Ti-alloys	41

4.1.1	Oxygen equivalent O_{eq} and solid solution oxygen equivalent O_{sseq}	41
4.1.2	Influence of Y on microstructural features	42
4.1.3	Influence of Y on tensile properties	47
4.2	Design of TiC redistribution sintering cycle.....	49
4.2.1	Carbon contamination sources.....	49
4.2.2	Analyses of particle characteristics of TiC_x	51
4.2.3	Mechanical properties	59
4.2.4	Fractography	61
4.2.5	Precipitation evolution of TiC particles.....	65
5.	Discussion.....	67
5.1	Rationality of using Y-containing sintering in PM/MIM β Ti-alloys.....	67
5.1.1	Mechanisms influencing tensile properties	67
5.1.2	Optimized Y-containing method and its significance for application.....	70
5.2	TiC_x redistribution sintering cycle for MIM β Ti-alloys.....	72
5.2.1	Particle redistribution behavior	72
5.2.2	Microcrack initiation and crack propagation mechanisms in specimens with different TiC_x partial distributional patterns	77
5.2.3	Additional effects of CSRA and Y addition on the Ti-matrix except for TiC_x redistribution	82
5.2.4	Influence of geometrical characteristics of TiC_x particles	84
6.	Technical perspectives.....	87
6.1	A comparison among various powder metallurgical processing of β Ti-alloys	87
6.2	Comparison with literature of MIM β Ti-alloys and effectiveness assessment for post-sintering treatments	89
7.	Conclusions and future work	93
	References	96

1. Introduction

The β Ti-alloys (viz. β alloys), are reported as the most versatile class of titanium alloys in literature and are a key structural material. They usually provide an attractive combination of mechanical properties. Furthermore, generated from their inherently deep workability, β Ti-alloys have enormous potential to further enhance their strengths through deep processing and/or deep heat-treating. Besides, β Ti-alloys can be engineered to allow for tuning the chemical composition of non-toxic alloying elements in such a way that low Young's moduli as well as good biocompatibility can be achieved. These abilities mostly contribute to the profound implications that β Ti-alloys have in both the lightweight structural and biomedical materials fields.

Metal injection molding (MIM) has remarkable industrial application potential and technical advantages to fabricate small-to-medium-shaped precision Ti-components, comprised of mass production, high-performance, sophisticated shape and cost-savings.

However, the commercialization of the metal-injection-molded (MIM) β Ti-alloys has long been restricted. In view of materials processing technologies MIM-fabricated β Ti-alloys often demonstrate an inferior crack resistance that can be basically attributed to the three major processing defects; (i) sintered porosity, (ii) coarse-grained structure, and (iii) high number of impurities. They are the common defects of most powder metallurgical processing of Ti-alloys as well. A detrimental effect of them is that a rather low damage tolerance to strain ratios can be easily observed, despite β Ti-alloys themselves are inherently ductile derived from the bcc-lattice structure of β -phases.

This work mainly deals with one of these three major issues. That is impurities contamination consisting of oxygen and titanium-carbides induced by excessive oxygen and carbon uptake respectively during processing procedure. Both the oxygen and carbide issues are considered as adverse factors for toughness performance of MIM-processed β Ti-alloys. Here, the strategies are to adopt an optimized and/or newly-designed sintering pathway instead of a conventional sintering cycle. It is widely recognized that such a scheme is superior to the technically preventive means (e.g. upgrade starting materials or special furnace) and the targeted post-sintering treatments (e.g. HIP, water quenching or thermo-mechanical processing).

In this work, two kinds of sintering pathways (briefly introduced below) will be studied for the purpose of the enhancement of fracture resistance to strain ratios of metal-injection-molded β Ti-alloys biomaterials.

Optimized Y-containing sintering cycle

Rare earth elements (RE) addition is commonly used for sintering some metals or alloys in order to optimize their as-sintered microstructures. Nevertheless, their effects on β Ti-alloys are not well-defined. In this work, yttrium (Y) as the most effective element for scavenging oxygen is chosen in order to improve the toughness. Through exploring MIM β Ti-alloys (Ti-20Nb-10Zr) produced by optimizing Y-containing sintering cycles, the influence on the mechanical properties were tested for the first time. Furthermore, the detailed effects of Y on oxygen scavenging, microstructure refinement and porosity increment will be investigated. The influence of using Y-containing (sintering cycle) on tensile properties of MIM β Ti-alloys will be thoroughly investigated.

Novel TiC_x -redistribution sintering cycle

In the first place, the sources of carbon uptake in MIM manufacturing β Ti-alloys, i.e. Ti-20Nb-10Zr(-0.1Y) herein, will be clarified. What is more, the precipitation evolution of TiC_x second phase and the embrittlement induced by *in situ* synthesized GB- TiC_x will be completely understood. Based on these observations, a novel toughening strategy by regulating TiC_x precipitation evolution and resultantly adjusting particles spatial distribution is suggested. A special sintering pathway capable of achieving this target will be engineered. Moreover, the corresponding mechanisms will be illustrated systematically.

2. State of the art

2.1 Development and application of β Ti-alloys

2.1.1 Development status

The β Ti-alloys (usually called “ β alloys”), especially the metastable type, have been reported as the most versatile class of titanium alloys [1], and are a key structural material in engineering. They are capable of providing a very attractive combination of mechanical properties, especially toughness and fatigue [1]. Furthermore, they have enormous potential to further enhance their strengths through deep processing and/or deep heat-treating. In addition, the material can be engineered to allow for biocompatible adjustability of non-toxic chemical composition and lower Young’s modulus [2, 3]. These two abilities mainly contribute to the profound implications that β Ti-alloys have in both the lightweight structural and biomedical materials fields. Nevertheless, their shortcomings also likely inhibit the widespread commercial utilization [4]. The advantages and disadvantages of β Ti-alloys are summarized in **Table 1** [5].

Table 1 - Advantages and disadvantages of β Ti-alloys [5].

Advantages	Disadvantages
-high strength-to-density ratio	-high density
-low modulus	-low modulus
-high strength/high toughness	-poor low and high temperature properties
-high fatigue strength	-small processing window (some alloys)
-good deep hardenability	-high formulation cost
-low forging temperature	-segregation problems
-strip producible – low-cost TMP* (some alloys)	-high springback
-cold formable (some alloys)	-microstructural instabilities
-easy to heat treat	-poor corrosion resistance (some alloys)
-excellent corrosion resistance (some alloys)	-interstitial pick up
-excellent combustion resistance (some alloys)	

*TMP: Thermo-mechanical processing

Despite these existing unsettled issues, the satisfactory performance of metastable β Ti-alloys led to the first commercial use of one of them in the Lockheed SR-71 blackbird (American surveillance aircraft) in the mid-1950s [6]. This β Ti-alloy (Ti-13V-11Cr-3Al) was developed by “Rem Cru Titanium” [7], and its special β lattice structure enables it to facilitate deforming and/or aging processes to a higher strength level. Therefore, a “formageable” (i.e. the ability to

form and to age at once) concept was proposed, synchronously arousing the research and development of a number of β Ti-alloys [8, 9]. In addition, the concept of gum alloys, reported by Saito et.al [10] in 2003, led to increasing studies on β Ti-alloys with low Young's moduli, super-elasticity, and shape memory effects [3, 11-13].

Definition

The universally accepted definition of a β Ti-alloy is, a Ti-based alloy containing sufficient β stabilizer content able to suppress the martensitic phase transformation and retain a hundred percent β phases during quenching to room temperature [14], as illustrated by **Figure 1** [15].

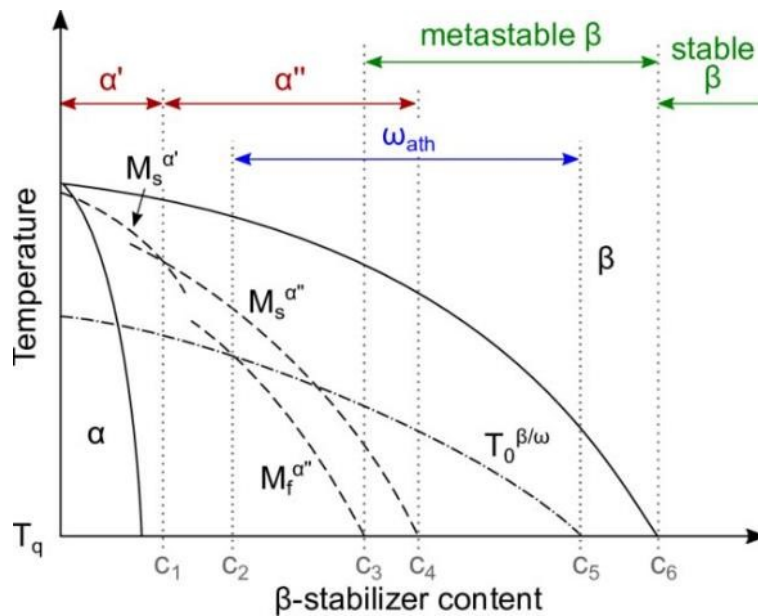


Figure 1 - Schematic illustration of the α - β Ti phase diagram in a isomorphs-type β Ti-alloys [15].

In addition, the β stability could be described by the concept of “Mo equivalent”, employed to assess the β stabilizing effects of diverse β elements [1]. To some extent, the β stabilizing effects can also be mirrored in the binary phase diagrams in **Figure 2** [16]. Recently originated from the gum alloys, a new burgeoning method (i.e. $\overline{Bo} - \overline{Md}$ diagram) arises to evaluate β stability by using electronic parameters [11, 17]. This kind of evaluation approach, in many cases, can correlate elastic properties or plastic deformation modes of β Ti-alloys, with their β stability [17]. Based on this approach, representative powder-metallurgical β Ti-alloys from literature are mapped in **Figure 3** (i.e. $\overline{Bo} - \overline{Md}$ diagram).

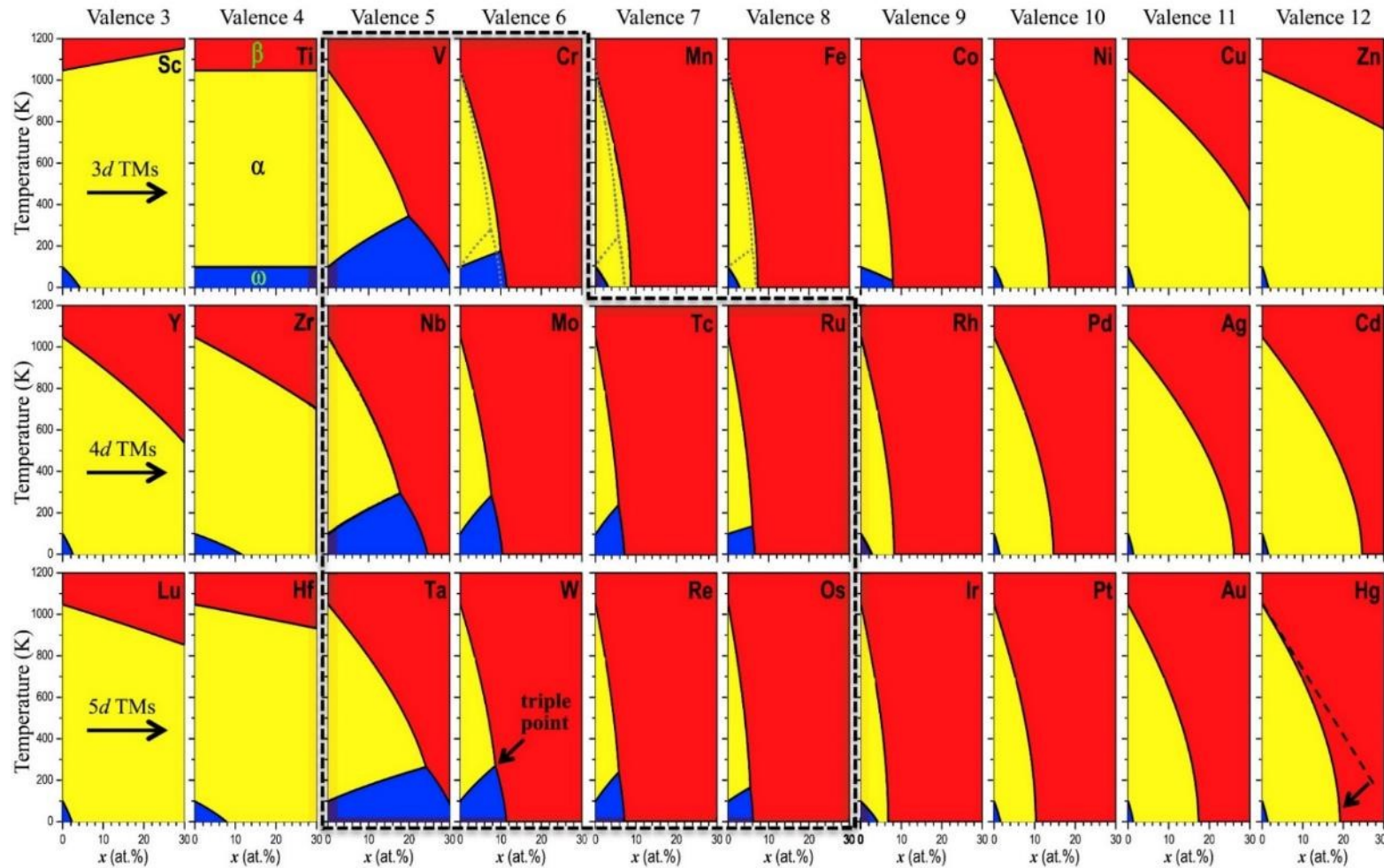


Figure 2 - Metastable binary phase diagrams of Ti–transition metal (TM) alloys computed from “*ab initio*”. Three phases are indicated there: α (yellow region), β (red), and ω (blue). The displayed α phase field corresponds to a large part to the α' or α'' phase, i.e., to the hcp or tetragonally distorted hcp phase obtained after quenching from the β phase field below the martensitic transformation temperature. The phase diagrams highlighted by the black dashed lines contain the special feature of a triple point at which the three phases meet as indicated for W [16].

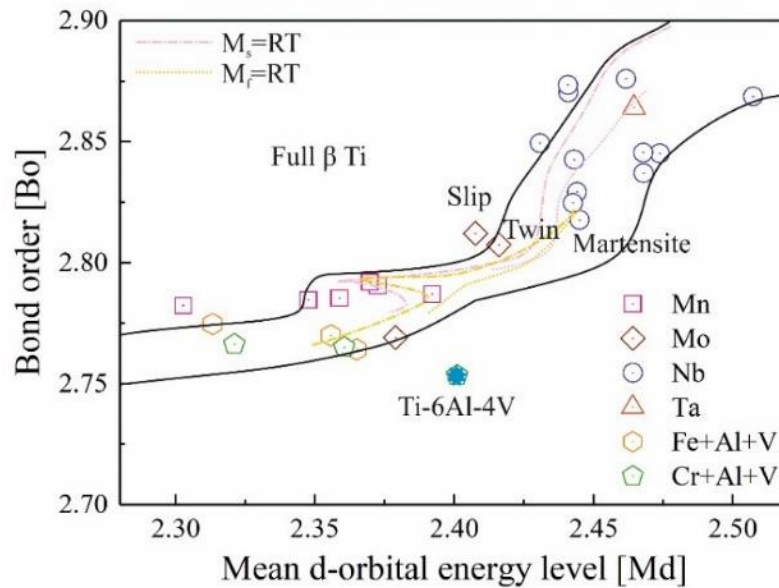


Figure 3 - Typical powder metallurgical β Ti-alloys investigated in literature indicating their deformation modes in $\overline{Bo} - \overline{Md}$ diagram, the original reference values of \overline{Bo} and \overline{Md} of typical elements are available in the Ref. [17].

Apart from a well-engineered β stability and certain chemical composition, an economical manufacturing route and a fracture-resistant microstructure is a key for the commercial success of a β Ti-alloy [1]. A traditional ingot metallurgical processing route of β Ti-alloys, more often than not, includes a thermomechanical processing operation followed by a heat-treatment, as the conventional processing pathways [6, 18]. Moreover, the final hot working step is carried out in the $\alpha+\beta$ field for the leaner β Ti-alloys, whereas preferentially in the β field for the richer β Ti-alloys [4, 7, 19, 20]. The heat treatment usually consists of a solution treatment followed by quenching and a subsequent ageing treatment [14, 21, 22]. To establish a technically sound processing window, systematic correlations among processing, microstructure, and mechanical properties have to be derived [1].

2.1.2 Applications

Technical field

Ti alloys are usually employed as lightweight structural materials, ascribed to high specific strengths and good chemical properties, but consistently high processing expenditure of fairly complex-shaped Ti-components hinders their widespread civilian use [1]. Among them, the most representative is the aerospace industry, which was their initial field of use as well [23-

26]. It has been witnessed that the use of titanium materials in the operating empty weight in the civil aircrafts increased from 1% to 19% over the last four decades [27, 28]. This trend can be obviously seen in **Figure 4**.

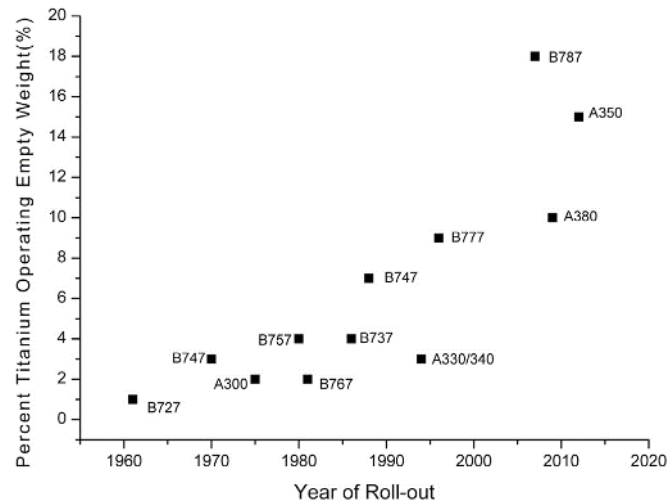


Figure 4 - The application proportion of Ti alloys in the major civil aircrafts [28].

Since the 1980s, β Ti-alloys started to be committed to the commercial airframe, principally, Ti-10V-2Fe-3Al, Ti-15V-3Al-3Sn-3Cr and Beta (β) C in the USA and Europe, and Ti-5Al-5V-5Mo-1Cr-1Fe (VT-22) in Russia [7]. In addition, Alloy C and Beta 21S, which have excellent elevated temperature performance, were applied for the nozzle system of many aircraft [29]. In the late 1990s, Ti-5Al-5V-5Mo-3Cr-0.5Fe (Ti-5553) was developed by VSMPO. It originated from the Russian VT-22 alloy and was officially commercialized on the Boeing 787 Dreamliner in the 2000s [26]. In particular, Ti-5553 offers a modest improvement in strength and toughness over Ti-10V-2Fe-3Al, to be more competitive [30]. Detailed data of some outstanding aerospace β Ti-alloys is listed in **Table 2**, adopted from [23, 26, 28].

Table 2 - Outstanding aerospace (beta) β Ti-alloys' products and applications [23, 26, 28].

The β Ti-alloys	Developer and date	Nominal composition (wt.%)	β transus ($^{\circ}$ C)	Applications
Ti-5553	VSMPO 1997	5Al5V5Mo3Cr0.5Fe	855-870	Aircraft landing gear; fuselage components and high lift devices
Ti-10V-2Fe-3Al	TIMET 1971	10V2Fe3Al	790-805	Aircraft landing gear
Ti-15V-3Al-3Sn-3Cr	TIMET 1978	15V3Cr3Al3Sn	750-770	Landing gear; springs; sheet; plate; airframe castings and environmental control system ducting
Beta 21S	TIMET 1989	15Mo2.7Nb3Al0.2Si	795-810	Nozzle assembly parts in Boeing 777
Beta C	RTI 1969	3Al8V6Cr4Mo4Zr	730	Springs and fasteners
Alloy C	P&W 1990	35V15Cr		Compressor and exhaust nozzle components

Biomedical field

From the perspectives of non-toxicity and low Young's moduli, biomedical β -Ti alloys have been indicated to have the highest biocompatibility for orthopedic applications among the mainstream metallic implant-materials, e.g. stainless steels, cobalt-chromium alloys, and Ni-Ti alloys. [13, 31].

- i) Toxic issue:** On the basis of "V-free" $\alpha+\beta$ type of titanium alloys (e.g. Ti-6Al-7Nb) [32, 33], V- and Al-free β Ti-alloys are developed, due to aluminum having been linked to Alzheimer's disease [11, 13]. The different kinds of toxicity of the major β stabilizers are briefly reviewed as presented in **Figure 5** [34]. Note that Al, Sn and Zr have been considered as β stabilizing elements in β Ti-alloys by some authors [17, 35-37]. It can be seen that Ti, Au, Sn, Ta, Nb, Ru and Zr can be classed as highly biocompatible. Hf and Re hold promise for further research, but must be treated with caution at present [34]. All other elements reviewed were considered less satisfactory.

Periodic position	Element	Biocompatible	Carcinogenic	Genotoxic	Mutagenic	Cytotoxic	Allergenic	Prone to corrosion	Other*	
3d	Ti	Yes	No	No	No	Med	No	No	No	
	V	No	Yes	Yes	Yes	High	Disputed	No	No	
	Cr	No	Disputed	Yes	Yes	High	Yes	No	No	
	Mn	No	No	Yes	No	High	No	Yes	No	
	Fe	No	No	Yes	Disputed	Med	No	Yes	No	
	Co	No	Yes	Yes	Yes	High	Yes	Yes	Yes	
	Ni	No	Yes	Yes	Yes	High	Yes	Yes	Yes	
	Cu	No	No	Yes	Yes	High	Yes	Yes	Yes	
4d	Zr	Yes	No	No	No	Low	No	No	No	
	Nb	Yes	No	No	No	Low	No	No	No	
	Mo	No	Disputed	Yes	Yes	Low	Yes	Yes	Yes	
	Tc	No	- Radioactive -							
	Ru	Yes	No	No	No	Med	No	No	Yes	
	Rh	No	Yes	Yes	Yes	High	Unknown	No	No	
	Pd	No	Yes	No	Disputed	Med	Yes	No	No	
	Ag	No	No	No	No	High	Yes	No	Yes	
5d	Hf	Unknown	Unknown	Unknown	Unknown	Med	No	No	Unknown	
	Ta	Yes	No	No	No	Low	No	No	No	
	W	No	Yes	Yes	No	Med	No	Yes	No	
	Re	Unknown	Unknown	Unknown	Unknown	Unknown	No	No	Unknown	
	Os	No	Unknown	Yes	Yes	High	No	Yes	No	
	Ir	No	No	No	Yes	High	No	No	Yes	
	Pt	No	Yes	Yes	Yes	High	Yes	No	No	
	Au	Yes	No	No	No	High	No	No	No	
Other	Al	No	No	Yes	No	Low	No	No	Yes	
	Zn	No	No	No	No	High	No	No	Yes	
	Sn	Yes	No	No	No	Low	No	No	Yes	

Figure 5 - Biological impact: Red indicates a serious concern; Yellow indicates a moderate concern; Green indicates minimal/no concern; *other refers to issues beyond those already listed, e.g. hemolysis, neurological effects, etc. [34].

ii) Elastic property: The bcc-lattice structure enables β Ti-alloys to theoretically achieve an extremely low elastic modulus. It has been demonstrated that Nb, Zr, Ta, Mo, and Sn are the most suitable alloying elements to decrease the modulus of elasticity of β Ti-alloys without compromising the strength [3, 11, 38]. Taking this into consideration, biomedical β Ti-alloys with a low modulus, e.g. Ti-13Nb-13Zr (the first biomedical β Ti-alloy) [4], Ti-12Mo-6Zr-2Fe [39], Ti-15Mo-3Nb-3O [40], Ti-29Nb-13Ta-4.6Zr [41], and Ti-35Nb-7Zr-5Ta [37] were widely investigated in the 1990s. In general, these early-developed biomedical β Ti-alloys were fabricated by the ingot metallurgical processing route, accompanied by thermomechanical processing (TMP). Ti-35Nb-7Zr-5Ta exhibited the lowest elastic modulus of 55 GPa and good fatigue performance [42]. Over the past two decades, some β Ti-alloys of the Ti-Nb system, regardless of processing way, have been found to achieve less than 50 GPa due to martensitic phase transformation induced via stress [21, 43-45]. In very recent years with the increase of powder-based additive manufacturing (e.g. SLM and EBM), specially structured (or configurational) parts from β

Ti-alloys can reach only ≈ 1 GPa Young's moduli, through building a specially geometrical porous structure, e.g. rhombic dodecahedron structure [46-48].

Ti-Ni was the early β Ti-alloy system used for super elastic and shape memory effects [12, 38]. Since 2003, the new concept of gum metal, represented by Ti-12Ta-9Nb-3V-6Zr-O (mol.%) and Ti-23Nb-0.7Ta-2Zr-O (mol.%) with ultralow elastic moduli, was proposed [10]. The research on Ni-free super elastic and shape memory β Ti-alloys biomaterials has been increased rapidly then. The binary Ti-Nb alloys are very representative of this. Specifically super elasticity emerges for 40–42 wt.% Nb content, whereas shape memory phenomenon appears for 35–40 wt.% Nb content [17, 49]. However, neither the super elastic nor shape memory effect emerges in the fully stable β Ti-alloys, i.e. >42 wt.% Nb content. Very recently, β Ti-alloys with a self-tunable modulus have been proposed, which are beneficial for the removability for orthopedic implants [3, 50-52].

The elastic moduli of typical powder-metallurgical β Ti-alloys reported in literature over the past decade are shown in **Figure 6**.

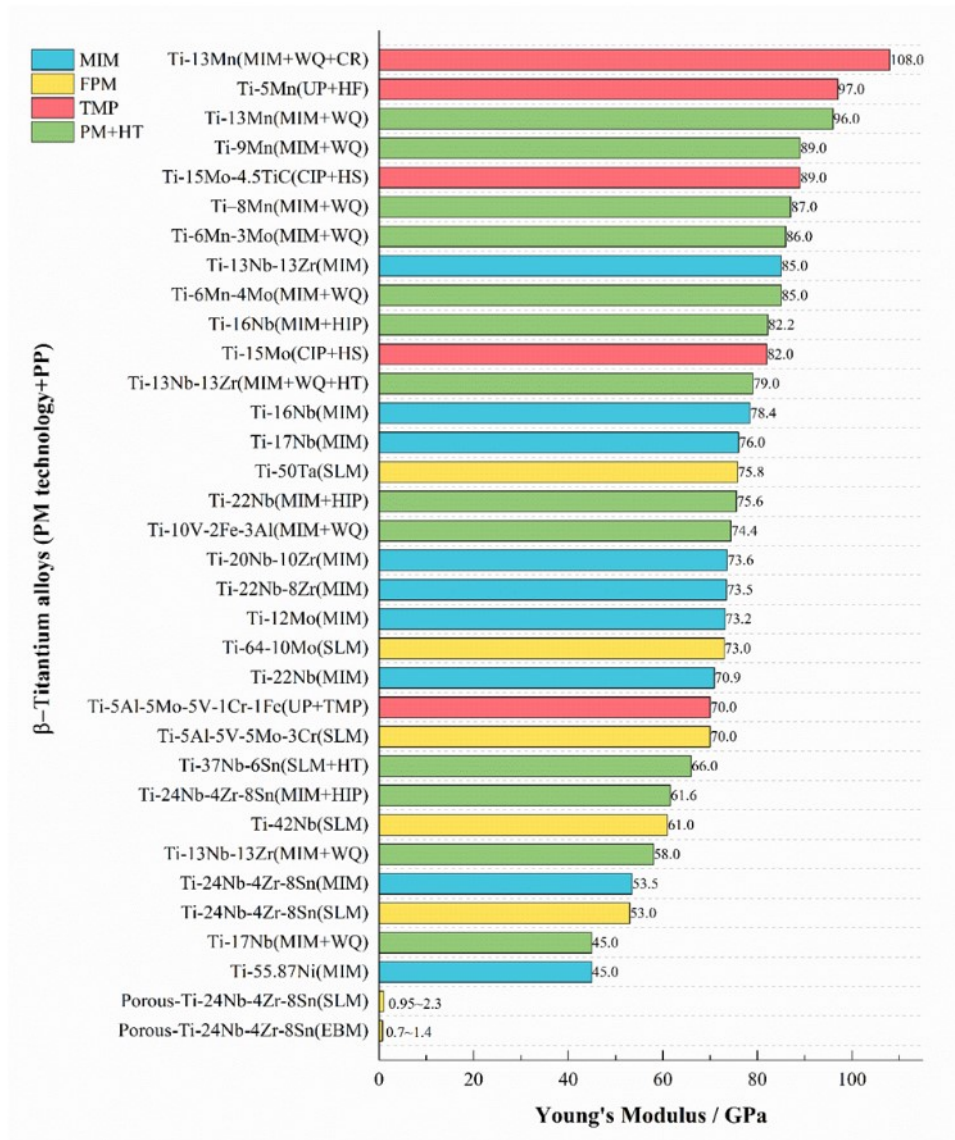


Figure 6 - Summary of Young's moduli of typical powder-metallurgical β -titanium alloys (β Ti-alloys) together with an indication of the processing. FPM: fusion-based powder metallurgy (corresponding introduction in section 2.2.4); PP: post-processing; PM+HT: powder metallurgy route plus heat treatment.

2.2 Powder metallurgy route

2.2.1 Overview of powder metallurgy Ti-alloys

The average “buy-to-fly” ratio of ingot metallurgy (IM) Ti is consistently high, approximately 12:1, indicating an extremely inefficient materials-consumption. However, powder metallurgy (PM) is able to fabricate the Ti-parts with complicated end-use shape via near-net shaping (NNS). Additionally, PM Ti alloys fabricated by some advanced sintering pathways are very

likely to achieve rather good mechanical properties in the as-sintered state, thereby eliminating traditionally energy-intensive and costly wrought processes (WP). Since the 1970s, achieving a high “performance-to-cost” ratio is the largest challenge for the PM-Ti field to overcome. If achieved, it would become a cost-effective alternative to traditional IM+WP route. The processes of PM Ti are comprised of the powder production, compaction and shaping, sintering, as well as post-sintering processes. This process and the WP route to produce Ti-products are both illustrated in **Figure 7** [53].

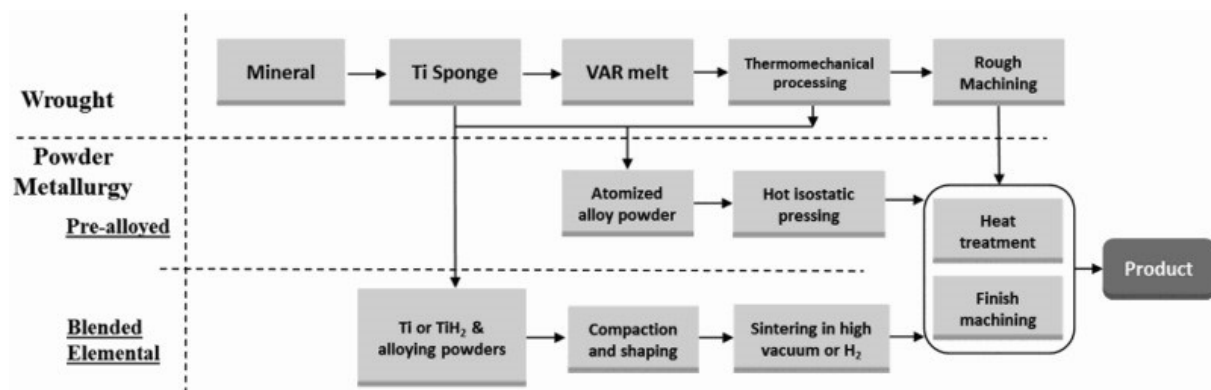


Figure 7 - Flow chart of conventional melt-wrought and powder metallurgy routes for manufacturing Ti products [53].

Powder metallurgical Ti-alloys seem to have substantial advantages, e.g. streamlining manufacturing procedures among others, but the reality is not optimistic. Its commercialization is still very limited, due to their expensive raw materials (high-value starting powders), energy-consuming post-sintering treatment (e.g. HIP), and commonly unsatisfactory mechanical performance (fracture toughness and fatigue). Generally speaking, poor mechanical performance is caused by the three major processing defects: i) residual porosity, ii) high impurities and iii) coarse-grained structure. The key issues of starting powders of β Ti-alloys will be reviewed in this section, as well as the forming technology – metal injection molding (MIM) – used in this Ph.D. project. The major processing defects (in Section 1.3) that significantly affect mechanical properties and the advanced sintering pathways (in Section 1.4) to cope with these defects will be systematically elaborated. However, the topics of; powder production technologies, conventional powder forming/shaping technologies, binder system and its debinding methods, traditional sintering cycles, and post-sintering processes will not be repeated in detail in this Ph.D. thesis. Numerous related reviews have been completed with respect to these topics [53-64].

2.2.2 Starting powder of β Ti-alloys

From the literature [22, 65, 66], the current powder production for β Ti-alloys mainly includes high energy gas atomization (via plasma melting induction gas atomization (PIGA), or electron melting induction atomization (EIGA)) and mechanical pulverization (e.g. hydride-dehydride (HDH)). Generally, gas-atomized (GA) powders have much higher costs than the HDH powders, but readily achieve a more satisfactory mechanical performance.

It is well-known, that there are two common methods to fabricate PM β Ti-alloys: the blended elemental (BE) method (in some cases, blending elemental and master alloy powders, i.e. BE/MA [67]) and the pre-alloyed (PA) method [68]. Although using PA powder likely produces relatively high mechanical properties, it is a major issue when using the traditionally uniaxial cold pressing plus vacuum sintering approach which results from a poor powder-formability caused by a high hardness. Therefore, to use PA powder, the special forming or consolidation technologies, e.g. binder-based powder forming and the CIP-sinter-HIP (CHIP) process, likely are necessary. For starters, **Table 3** shows some representative β stabilizing element powders used in the literature.

Table 3 – Already applied β stabilizing element powder data in the literature over the past decade.

β -stabilizer	Shape	Size (μm)	Particle size distribution (PSD) (μm)	Purity or C/O levels (ppm)	Production methods	Manufacturers
Nb	A ¹		D ₁₀ =25, D ₅₀ =41, D ₉₀ =67	O=720 C=20		H.C. Starck Tantalum and Niobium GmbH, Germany
Nb	S ²	<45		O=4000 C=200		Haines & Maassen Metallhandelsgesellschaft mbH, Germany
Nb	A	M ⁴ 4.9		O=4500 C=180	HDH	Centro Te'cnico Aeroespacial (CTA), Brazil
Zr	A	M 2.57		O=10900 C=220	HDH	Centro Te'cnico Aeroespacial (CTA), Brazil
Zr	S		D ₁₀ =18, D ₅₀ =35, D ₉₀ =52	O=1740 C=100	GA	TLS Technik GmbH & Co. Spezialpulver KG, Germany
Zr	I ³	<45		O=5075 C=142		Aber GmbH, Germany
Mo		<25		O=2000 C=500	hydrogen-reducing	Beijing Xing Rong Yuan Technology Co. Ltd. China
Mo	I	<2		O=3800		
Mn	A	<45		O=7700	mechanically grinding Mn flakes	Tohoku University, Japan

¹A: angular; ²S: spherical; ³I: irregular; ⁴M: mean particle size; marked in red: Max; mark in green: Min

In the past ten years, the β stabilizing element powders were mainly produced by mechanical pulverization, which invariably resulted in irregular shape and high impurity levels, in particular

some refractory metals, e.g. Mo, Nb, Ta and Zr, incorporating more than ≈ 3800 ppm oxygen in many starting elemental powders. These factors will eventually deteriorate the mechanical properties of β Ti-alloy parts. Unfortunately, so far, the PA powder market of β Ti-alloys is not optimistic either. Owing to the fact that so few PA powders of β Ti-alloys have been successfully industrialized, their PA powder production is far less mature than that for traditional Ti-6Al-4V alloys. The PA powders of β Ti-alloys reported in the literature are listed in **Table 4**. In the view of impurities, data in **Table 4** suggests that the plasma atomization (from PA wire) technique can offer improved pre-alloyed β Ti-powders [69, 70].

Table 4 - The PA powders data of β Ti-alloys reported in the literature.

β -stabilizer	Shape	Size (μm)	Particle size distribution (PSD) (μm)	Purity or C/O levels (ppm)	Production methods	Manufacturers
Ti-42Nb	S	<63	$D_{10}=6.3, D_{50}=19, D_{90}=44.8$	O=2674 C=37	EIGA	H.C. Starck Tantalum and Niobium GmbH, Germany
Ti-42Nb	S	<45		O=3103 C=63	EIGA	H.C. Starck Tantalum and Niobium GmbH, Germany
Ti-45Nb	S	20 ~ 100			EIGA	TLS Technik GmbH & Co. Spezialpulver KG, Germany
Ti-Ni	S	<20	$D_{10}=3.7, D_{50}=10.3, D_{90}=21.5$	O=1230 C=860	GA	Nanoval GmbH, Germany
Mo-C	NS ¹	<5		P=98%		[71]
Ti2448	S	<45			GA	TLS Technik GmbH & Co. Spezialpulver KG, Germany
Ti2448	S	45 ~ 106	$D_{10}=47.2, D_{50}=79.4, D_{90}=130.2$	O=1900	EIGA	[72]
Ti185	A		$D_{10}=21, D_{50}=51, D_{90}=68$	O<7800	BM ² elemental mixture	McMaster University, Canada
Ti-25Nb-3Zr-Mo-2Sn	S	30 ~ 55	$D_{50}=42$		GA	[73]
Ti5553	S	25 ~ 45	$D_{50}=35.71$		EIGA (from extruded rods)	IFW Dresden, Germany
Ti55511	S	100 ~ 300		O<1000 C<240	plasma atomization (from PA wire)	[22, 74, 75]
Ti15333	S	<45	$D_{50}=69$	O=1050	EIGA (from rods of wrought)	Helmholtz-Zentrum Geesthacht, Germany

¹NS: near spherical; ²BM: balls milling; marked in red: Max; mark in green: Min

Even though using low-cost BE (purely or mixing MA powders) methods consistently results in unsatisfactory mechanical properties, especially toughness and fatigue as compared to the PA method, it is still considered to be the most cost-effective methods. The BE methods contain the enormous potential to enhance mechanical performance through optimal powder metallurgical processing [53]. Many efforts thus have been devoted to optimize and upgrade processing parameters, e.g. advanced sintering pathway and low-energy post process, to deal with the major PM Ti defects.

2.2.3 Metal injection molding (Ti-MIM)

As a well-established powder metallurgy technology for a variety of metallic materials, metal injection molding (MIM) was used to manufacture β Ti-alloy parts in this investigation. MIM has remarkable industrial application potential and technical advantages to produce Ti alloy parts (often called Ti-MIM). The advantages of MIM include the ability for mass production, high-performance, sophisticated shape, and cost-savings. At present, Ti-MIM is of growing interest in the healthcare, aerospace, instruments and apparatus, and automobile industries [19, 55, 76, 77].

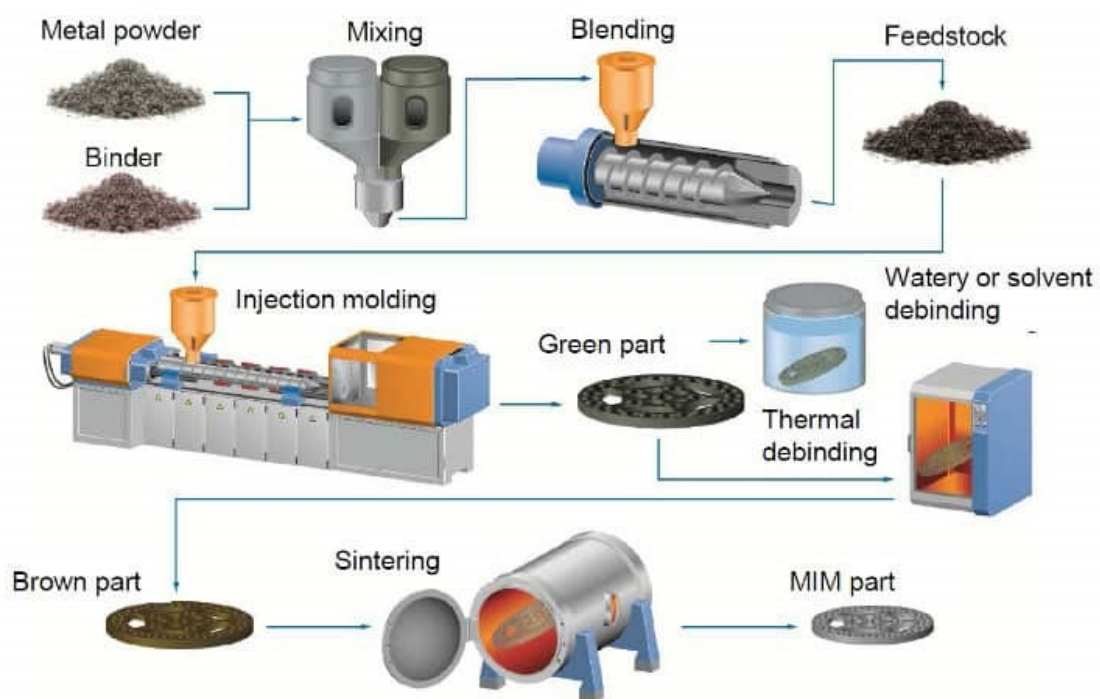


Figure 8 - Schematic diagram of metal injection molding (MIM) [78].

From MIM schematic diagram as detailed in **Figure 8**, it can be seen that MIM process includes feedstock preparation, injection molding, chemical and thermal debinding, sintering, and possible post-processing and surface finishing. This process is not without its flaws. For MIM fabrication, one of the major PM processing defects (directly related to the mechanical properties) that people are most concerned about is an increased interstitial uptake. There is no direct evidence that the use of binders causes additionally residual porosity and coarsened microstructure, compared with other PM technologies, as documented in the literature. This high impurity contamination is a long-standing issue for Ti-MIM, stemming from the usage of

the polymeric binder and imperfect debinding process. Although various binder systems and debinding techniques have been optimized and upgraded to some degree, impurities are still present. Apart from efforts on basic issues of Ti-MIM, current work is mainly forced on issues of oxygen pick up for $\alpha+\beta$ Ti alloys (e.g. Ti-6Al-4V [76, 79-81] and Ti-6Al-7Nb [82]) and carbon pick up for β Ti-alloys (e.g. Ti-Nb [83, 84] and Ti-Mo [85]).

2.2.4 Fusion powder technologies (non-sintered Ti-alloys)

The present work only concerns the traditional powder consolidation route (i.e. sintering). This refers to the sintering-based powder metallurgy (SPM). Currently, other powder consolidation routes, i.e. additive manufacturing (AM) have attracted much attention. Many studies regarding AM-processed β Ti-alloys have been reported [30, 46, 86-93]. To establish a complete understanding of the relationships between processing, structure and performance, additive manufacturing (AM) technologies as for example SLM, EBM and LMD, have to be taken into account. In this article, these processes shall be referred to as fusion-based powder metallurgy (FPM). The different and sometimes complicated processes of fusion and further processing as well as the resulting microstructures will be introduced below.

Fusion-based powder metallurgy (FPM) technology makes up the majority of AM, but excludes some AM techniques such as feeding metallic wire. Compared with sintering, the significant difference comes in the form of a localized heat source (laser or electron beam) which is used to fuse metallic powders. Therefore, metallic powders are melted during FPM processing, while there is normally solid sintering in SPM technology. On the one hand, the starting powders can be from a pre-paved powder bed, and be fused via a heat source, referring to powder bed fusion technologies, e.g. SLM (or LBM) and EBM, etc. On the other hand, powders can be ejected from a nozzle at the same time as fusion occurs, this method refers to directed energy deposition, e.g. LMD, etc. The starting powders are locally melted under a certain absorption power and heat source scanning velocity (i.e. P+V combination) and welded to adjacent metallic solid, and finally consolidated into an integral part by fast cooling. Each small unit volume of metal powders undergoes a fairly complex thermal cycling that involves rapidly rising to the melting point, followed by fast cooling to consolidation, and then multiple re-heating and re-cooling cycles. A complex temperature gradient throughout the FPM-component processing is also subject to factors such as energy density, layer thickness, and possibly applied preheat-temperature.

Since FPM β Ti-alloys parts are consolidated by a very fast cooling rate (10^3 K/s, or even as fast as 10^8 K/s), it is normal to obtain a fine-grained microstructure, which is finer than the majority of ingot metallurgic (IMed) and SPMed Ti-alloys [94, 95]. Owing to the absence of high-temperature holding as well as the atmospheric protection of inert Ar or He, the oxygen uptake in FPM Ti is much lower than that of SPM Ti (e.g. 800 ppm to 1000 ppm) and usually negligible. Low oxygen uptake and the use of expensive pre-alloyed powders in FPM, result in acceptable impurity levels in as-printed β Ti-alloys parts, e.g. 0.2 wt.% residual oxygen in SLMed Ti-24Nb-4Zr-8Sn [46], 0.19 wt.% residual oxygen in EBMed Ti-24Nb-4Zr-8Sn [96], and 0.11 wt.% residual oxygen in LMDed Ti-5Al-5Mo-5V-1Cr-1Fe [22, 75]. In the view of processing porosity, after optimizing the "P+V" combination, the relative densities of as-printed FPM β Ti-alloys parts can reach more than 99.5%. Recently, a re-melting approach has been proven to increase relative density to 99.964% from 99.2% [94, 97]. All in all, the three issues (i.e. coarse-grained structure, high impurities, and residual porosity) that SPM β Ti-alloys face, hardly occur in FPM β Ti-alloyed parts. However, there is a serious anisotropy in these parts which include orientation-dependent and location-dependent mechanical performance. In other words, the mechanical properties parallel to building direction are superior to the ones perpendicular to building direction. The inherently fast cooling step, large temperature gradients, and complex thermal cycles are prone to produce residual stresses, and an undesired brittle phase (α' martensitic phase) which may enhance the strength, decrease the ductility and cause, in some cases, deflection deformation.

2.3 Major processing defects of MIM β Ti-alloys

It is widely recognized that traditional PM Ti alloys consistently need to tackle the three major processing defects: i) residual porosity, ii) high impurities and iii) coarse microstructures, whereas they rarely are a problem in IM route [53, 57]. Unfortunately, for binder-based PM techniques like; MIM, Binder Jetting, or Fused Filament Fabrication (FFF), they have to utilize polymeric binder. These technologies hence unavoidably introduce extra interstitials uptake during the debinding process, where improper removal of residuals after pyrolysis of polymers often occurs [98]. What's worse, in regards to β Ti-alloys, immature commercialization of β Ti-starting powders leads to more serious processing defects of MIM β Ti-alloys than traditional Ti-6Al-4V powders. This is caused by the refractory β -stabilizing elements with poor diffusivity (a higher temperature sintering is required [99]) and the inherently coarse-grained nature of β Ti-alloys [100]. All in all, with respect to major processing defects, MIM β Ti-alloys

tend to have much more severe defects than those in traditional PM Ti-6Al-4V alloys. In this section, the origins of major processing defects of MIM β Ti-alloys and their effects on mechanical properties are elaborated, which is conducive to seek an economical and effective dispose to mitigate their negatives.

2.3.1 Residual porosity

Residual porosity, as a processing defect, is a basic microstructural feature of PM metallic materials. PM Ti alloys can be deemed as composites of Ti-matrix and porosity. In addition to capturing small amounts of inert gas, the formation of pores can also be due to incomplete volume and grain boundary diffusion processes, which can close gaps between particles, as shown in **Figure 9** [101].

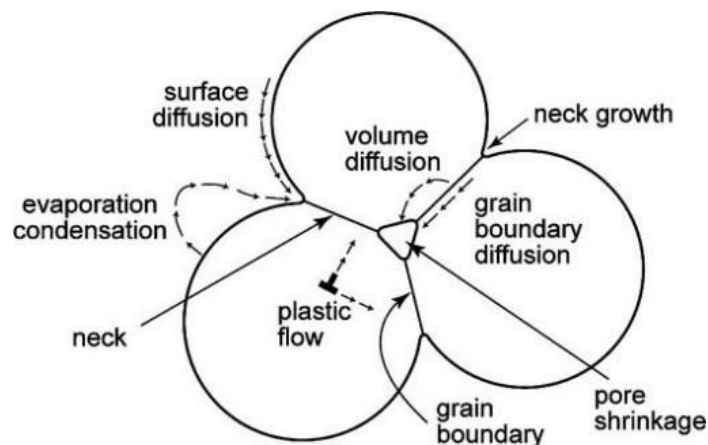


Figure 9 - The various mass transport paths affecting neck growth and pore shrinkage. Generally, surface diffusion, which gives no densification, and grain boundary diffusion, which gives densification, are the most common transport processes [101].

For PM β Ti-alloys, some refractory elemental powders (high melting points) are frequently used, such as Nb, Mo, Ta (see **Table 4**). These refractory elements have very poor diffusivity which weakens the grain boundary densification process during sintering, thereby causing a higher residual porosity than traditional Ti alloys. Normally, the porosity of PM β Ti-alloys is 1~3% higher than that of PM Ti-6Al-4V [57]. Note that some binder-based PM technologies (e.g. FFF), due to the technical limitation of low powder loading, have a significantly higher porosity.

In general, residual porosity exists in the two forms of common internal pores and external pores (i.e. surface roughness) in as-sintered Ti alloys [55]. The studies from Ferri et al. [102] have demonstrated that the effects of these two kinds of porosity on mechanical properties of MIM Ti alloys are different. An optical photograph of internal and external porosity in MIM β Ti-alloys is given in **Figure 10**.

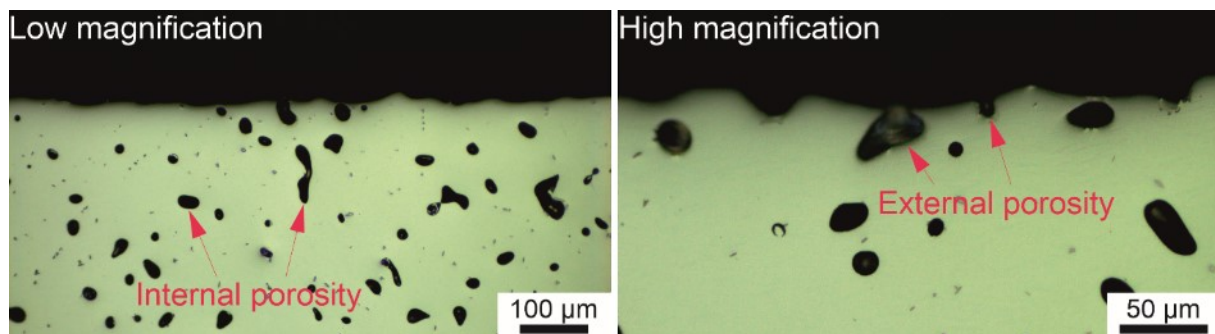


Figure 10 - The internal and external porosity of MIM β Ti-alloys (as-sintered Ti-20Nb-10Zr-0.1Y).

The effects of residual porosity (external and internal) on the mechanical properties of MIM Ti-6Al-4V, compared with MIM β Ti-alloys explored by this investigation are summarized in **Table 5**. Obviously, the internal residual porosity can remarkably decrease the tensile strength and slightly reduce the elongation [56]. Specifically, the UTS of MIM Ti-6Al-4V can degrade approximately 30% as porosity increases from near 0% to 6%, accompanied by a modest decline in ductility [76]. The effect of internal pores on the tensile properties of MIM β Ti-alloys shows a similar result [84, 99]. Whereas, surface roughness (i.e. external porosity) has been proved to have a negligible effect on tensile properties [102]. The biggest harm caused by external residual porosity on the mechanical properties is on fatigue strength. Compared with untreated MIM Ti-6Al-4V, shot peening to improve surface quality is capable to increase the fatigue endurance limit by around 100 MPa [102], while untreated MIM β Ti-alloys in the present study just show less than 1% of the fatigue life at 600 MPa of the shot peened ones. Interestingly, residual pores in some cases can limit grain growth [103].

Table 5 - Effects of residual porosity on mechanical properties of PM Ti alloys [104-107].

Pore types	Tests	Mechanical properties	Ti-6Al-4V	β Ti-alloys
Internal	Tensile test	UTS	--	--
		ϵ_f	-	-
	High cycle fatigue	Fatigue endurance limit (10^7)	-	--
External	Tensile test	UTS	O	O
		ϵ_f	\approx O	\approx O
	High cycle fatigue	Fatigue endurance limit (10^7)	---	---

*-: slight deterioration; --: modest deterioration; ---: severe deterioration; O: basically no influence

Up to now, porosity has been effectively controlled by using metallic powders with small particle size, high sphericity, and high compaction density. Employing PA powder has also been shown to reduce porosity. Furthermore, optimized or advanced sintering pathways via promoting diffusion rate or enhancing densification effect are capable of effectively reducing residual porosity. Examples of this involve using a higher sintering temperature, adding sintering-aid (e.g. iron), and HSPT pathway. In addition, many post-sintering treatments aiming to reduce residual porosity, e.g. HIP (heat isostatic pressing), GIF (gaseous isostatic forging) or even conventional TMP (thermo-mechanical processing), are applied on PM Ti alloys.

2.3.2 Coarse-grained structure

For traditional processing routes, the as-cast state offers thermal residual-stress and the as-forged state provides mechanical residual-stress. Both are beneficial to recrystallization for refinement effect. Nonetheless, the longtime homogenization diffusion treatment at high temperature and subsequent very slow furnace cooling rate in a conventional sintering cycle lead to a serious microstructure coarsening behavior in PM Ti alloys. Unlike the as-cast and as-forged states, there is basically nothing limiting the grain growth, e.g. pinning effect from high-density dislocation walls (the as-forged) or rapid cooling procedure (both).

Generally, the mean diameter of α/β colonies of as-sintered MIM Ti-6Al-4V is in the range of $90 \mu\text{m} \sim 150 \mu\text{m}$ [61, 108, 109]. However, the prior β grain size for as-sintered MIM β Ti-alloys is even higher. Examples include Ti-Nb alloys with a grain diameter of $\approx 300 \mu\text{m}$ [110], and Ti-24Nb-4Zr-8Sn with grain diameters of $350 \sim 410 \mu\text{m}$. A brief explanation of this growth is given below. In the first place, this rapid grain coarsening is caused by enhanced diffusion in the β structure at elevated temperatures. On the other hand, most β Ti-alloys contain scarcely any primary equiaxed α grains, therefore no independent α grain appears amid β grains above

the α/β transus. For some β Ti-alloys containing slowly diffusing elements, the grains are further coarsened by consequently high-temperature sintering program. Due to specific microstructural features of metastable β Ti-alloys, this coarsening behavior also occurs in the grain boundary α phase (α_{GB}) and the acicular secondary α phase (α_s) within the prior β grain. The α_{GB} is generally considered as a toughness-disadvantageous phase, controversially, it recently has been found to enhance fracture resistance in certain cases [22].

Very recently, Limberg et al. reported at the PMTi-2019 conference that MIM Ti-6Al-4V alloys, which vary in their grain size produced by several advanced sintering cycles, exhibited apparently different tensile and fatigue properties as summarized in **Table 6**. Simply speaking, with the decrease of an order of magnitude from an initial grain size around 150 μm , the tensile strength was increased by about 100 MPa, as well as the fatigue strength was increased by 125 to 200 MPa. Interestingly, the elongation to fracture did not increase significantly even though the grain size decreased by two orders of magnitude.

Table 6 - Effects of grain size on conventional mechanical properties of MIM Ti-6Al-4V.

Sintering cycle	Conventional sintering	B sintering cycle or SBS	HSPT pathway	Refinement effect
Grain size (α/β colony)	90~150 μm	15~23 μm	≈ 4.5 μm	
Tensile strength	810 MPa	900 MPa	1020 MPa	++
Elongation to fracture	-----All $\varepsilon_f = 12\sim 14\%$ -----			O
Fatigue limit strength @10 ⁷ N	450 MPa	650 MPa	775 MPa	++

*+: slight increase; ++: modest increase; +++: significant improvement; O: basically no influence

One of the most commonly used strategies of controlling grain overgrowth of PM Ti alloys is to sinter to just higher than 95% relative density at lower temperatures or in shorter time to inhibit its grain growth [55]. Afterwards, a post-sintering process, such as HIP or GIF, is then performed to achieve completely closed pores [57]. The current trend in the PM Ti field is to upgrade these traditional sintering pathways. One of the purposes of many newly designed sintering cycles is to refine the microstructure of PM Ti alloys. For example, prevalent rare-earth (RE) sintering cycle system [79, 81, 109, 111-114], the boron sintering cycle developed by Ferri et al. [115], the SBS (Selective Bead Sintering) developed by Element 22 GmbH, Germany, and the HSPT pathway developed by Fang et. al [116] have been indicated to refine

effectively the grain size of PM Ti alloys, by an order of magnitude or even to submicron scale. Apart from adjusting the sintering program, post-processing (e.g. TMP and STA (solution treatment and aging)) is a traditional way to obtain fine grains. However, this comes at the expense of energy-consumption, extra cost, interstitial uptake, and possibly the compromise of NNS complex shapes.

2.3.3 Interstitial impurities levels

Oxygen

High oxygen level has always been a technical issue for PM Ti alloys. Also, it is the most representative interstitial impurity, thus the oxygen equivalent (O_{eq} , [54]) is often used to describe the overall impurities level in PM Ti alloys [117, 118]. C_C , C_N and C_O denote the content of carbon, nitrogen and oxygen, respectively.

$$O_{eq.} = \frac{3}{4}C_C + 2C_N + C_O \quad (1)$$

As can be seen from the Ti-O binary phase diagram (**Figure 11**) [119], owing to a rather high solubility of oxygen in titanium, oxygen atoms generally exist as interstitial solute in the Ti-matrix [53]. This implies that during the sintering process, the titanium oxide (TiO_2) on the surface of the starting Ti powder, as well as the oxygen atoms originating from the sintering atmosphere or the thermal pyrolysis by imperfect debinding (in some cases), are readily dissolved into the Ti-matrix. Lefebvre et al. [120] found that in MIM-processed Ti-6Al-4V by using 45 μm PA powder, the oxygen pickup sources are the sintering process (the most part), starting powder and the debinding steps (the least part).

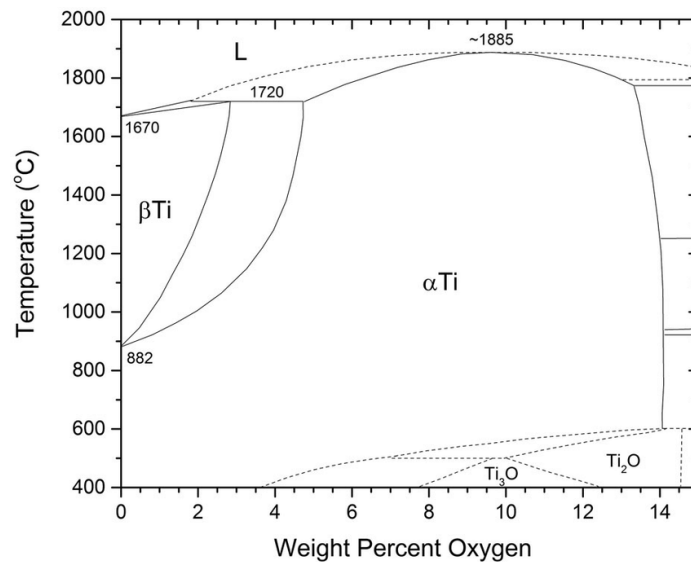


Figure 11 - Titanium-oxygen binary phase diagram [119].

Normally, the oxygen levels in PM Ti parts can be regulated below an acceptable content, e.g. ≈ 1500 ppm according to the literature [76, 121], when PA or high purity powders are used as starting materials. The oxygen levels worsen when low-cost mechanical milling powders, e.g. HDH [79] or refractory β elemental powders are used. Strong β -phase stabilizers Nb and weak stabilizers such as Zr, Ta and Hf [16], may also possess high oxygen levels (e.g. GA Nb $< 45\mu\text{m}$ ≈ 2200 ppm, Zr $< 45\mu\text{m}$ ≈ 5000 ppm). In effect, higher oxygen residuals are more possible to remain in final as-sintered Ti parts. However, even a trace amount of oxygen, e.g. ≈ 1200 ppm [122], still can radically alter phase constitution, microstructure and mechanical properties [123].

The oxygen atoms in the solution state are most likely to deteriorate the ductility of PM Ti alloys by the formation of brittle phases and/or by changing the deformation mechanisms [124]. Specifically, oxygen is likely to promote the formation of α_{GB} (controversial [22]), carbon-deficient GB- TiC_x , martensitic phase, α_2 phase (Ti_3Al in Al-containing Ti alloys) and oxygen-enriched region, consequently degrading ductility. With respect to the issue of whether oxygen promotes the ductility-unfavorable ω -phase, so far there is a controversy. Some studies [45, 123-125] suggest that oxygen can suppress or even eliminate the formation of the ω -phase, while the latest research [126] shows that oxygen atoms increase its stability. Furthermore, oxygen was found to inhibit the deformation modes of twinning and slipping. Therefore, it seems highly probable that the effects of oxygen atoms on the mechanical properties of either $\alpha+\beta$ Ti alloys or β Ti-alloys are different.

As a result, it has been verified that the critical oxygen levels for ε_f (elongation to fracture) are beyond ≈ 3300 ppm for MIM-processed Ti-6Al-4V [121, 127], while at ≈ 3800 ppm for MIM-processed Ti-6Al-7Nb [128]. Differing from tensile properties of $\alpha+\beta$ type traditional Ti alloys, β Ti-alloys are consistently considered to have a higher oxygen tolerance up to ≈ 8000 ppm, with merely a modest increase in strength and a mild decline in ductility [124]. In addition, it is thought that oxygen atoms can also form zirconium-oxygen atom clusters which provide the gum effect in Zr-containing β Ti-alloys [10]. When it comes to how oxygen effects the fatigue behavior, the situation in different Ti alloy types becomes very interesting. For CP-Ti (α -type) [129] and β Ti-alloys [130], it has been demonstrated that oxygen is able to enhance high cycle fatigue (HCF) performance. Conversely, for $\alpha+\beta$ types, e.g. Ti-6Al-4V [131, 132], Ti-6Al-7Nb [128], oxygen obviously deteriorates HCF strength indirectly by changing the α lamellae width [133-135] and the morphology of other relevant phase.

To avoid catastrophic fracture failure when used as structural materials, the control of oxygen uptake in PM Ti processing is always a main priority. At present, the means to confine oxygen uptake in PM Ti mainly include technical precautions, optimizing raw materials and the sintering cycle (or chemical reactions during sintering processes), and using high vacuum furnaces, etc. Furthermore, in the early stage of alloy design, a trace amount of rare earths (REs), as the oxygen-scavenger [109], can be added into the composition of Ti-based materials and mixed with the main starting powders, to form the O-bound (RE-oxides) compounds during high temperature sintering. As a consequence, the O-content in the Ti-matrix declines. In addition, there are many technical precautions such as running a “burn-out” program prior to the formal sintering program. This is the most common way. However, for laboratory manufacturing, putting O-traps in the furnace surrounding the green (or brown in MIM case) Ti-specimens, as well as careful handling, is considered to be able to reduce the oxygen content to ≈ 500 ppm, etc. [56, 57, 136]. For Ti-MIM, using MA Ti powders with a particle size of <45 μm is a compromise that accounts for oxygen uptake and densification [55]. Apart from the powders quality control and binders selection, etc., high vacuum sintering atmosphere is currently considered to be superior to inert gas sintering [55].

Carbon and carbide-phase

Among all impurities in PM Ti alloys, carbon uptake has not aroused the same concern as the others. This is because carbon atoms exist in the form of interstitial solutes in traditional Ti alloys, e.g. Ti-6Al-4V, and their effect is usually considered weaker than oxygen (oxygen

equivalent $\frac{3}{4}$). Moreover, for as-sintered Ti-parts, the carbon content normally is much lower than the oxygen level, e.g. <800 ppm [106]. Therefore, the adverse effects of carbon are often simply classified as a weak oxygen effect (i.e. $\approx \frac{2}{3} O_{eq.}$) and considered to contribute like a small amount of oxygen impurity level, and are thus often overlooked for most PM Ti alloys. However, completely unlike the behavior of carbon in $\alpha+\beta$ Ti alloys, carbon contamination is a serious issue in PM β Ti-alloys. Almost all β Ti-alloys fabricated via PM technologies (incl. the press and sintered and MIMed) have long suffered from embrittlement induced by carbon contamination. Typical contamination sources are generally the starting powder and the sintering furnace atmosphere in traditional PM technologies [53, 120]. Since, binder-based powder metallurgy technologies, such as MIM and binder jetting, utilize polymeric binder; it can be assumed that extra carbon uptake commonly takes place during the thermal debinding process, where improper removal of residuals after pyrolysis of polymers likely occurs [55, 61] and the temperature is relatively high (typically around 600 °C). Thus, diffusion of carbon into the alloy can occur easily.

Carbon with a rather large atomic radius (≈ 70 pm) has a low solubility in the interstitial sites of the Ti-lattice, unlike oxygen (≈ 60 pm) which is highly soluble [137]. Furthermore, the tetrahedral interstitial sites with $r_{void}/r_{atom} = 0.291$ in the β -Ti body-centered cubic lattice is $\approx 30\%$ smaller than the octahedral interstitial sites with $r_{void}/r_{atom} = 0.414$ in the α -Ti hexagonal closed packed lattice, which both are the largest sites in the respective Ti-lattices [124, 138-140]. The total solubility of carbon thus could be significantly reduced when a high concentration of β -stabilizers is added (see **Figure 12** [141]).

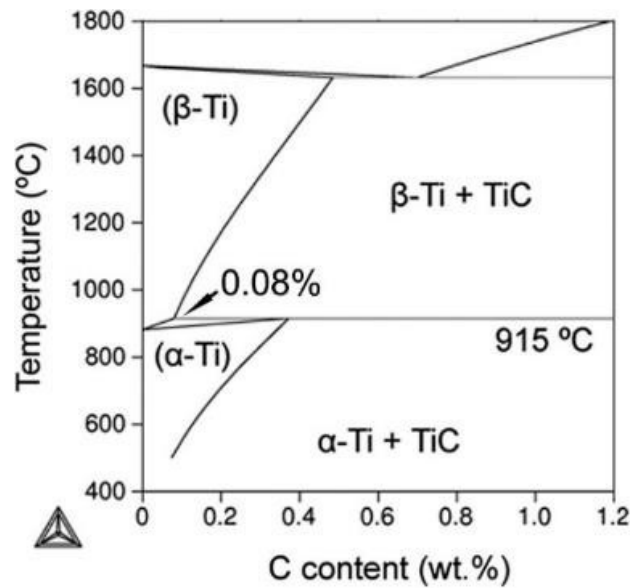


Figure 12 – Calculated Ti-C binary phase diagram up to 1.2 wt.% C [141].

In general, titanium-carbides (TiC_x) precipitate along grain boundaries (GB), i.e. in the form of GB-TiC_x (e.g. **Figure 13**) when carbon concentration exceeds the solubility limit in the Ti-matrix. This low solubility limit is a dominant factor of the high susceptibility of β Ti-alloys for embrittlement induced by carbon contamination. It has been widely recognized that GB-TiC_x second-phase particles cause brittle and premature intergranular fracture of powder metallurgically processed β Ti-alloys [19, 61, 110, 141-143]. Such materials exhibiting rather low toughness to strain ratios are not an option for critical structural application, where catastrophic damage is completely unacceptable. Therefore, commercializing them has been severely obstructed until now.

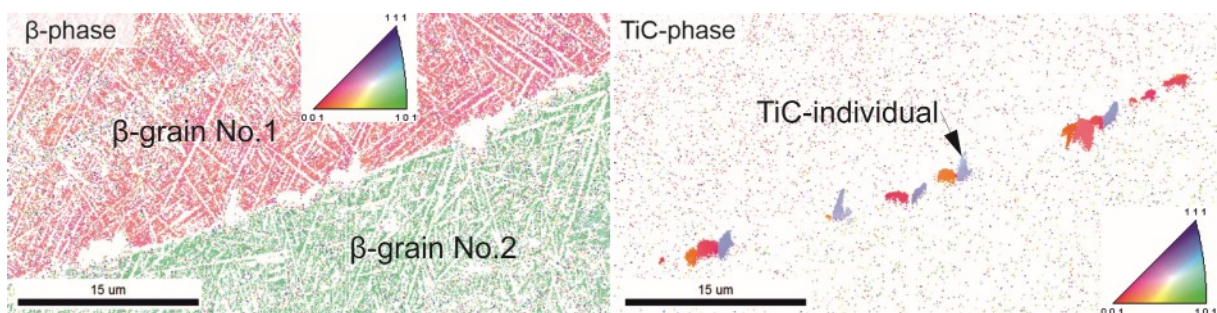


Figure 13 - EBSD images of aligned GB-TiC_x second-phase precipitate along grain boundaries of MIM Ti-20Nb-10Zr.

Many works to characterize the atomic-scale lattice configuration of TiC_x have been undertaken. Researches demonstrated that TiC_x exists as stoichiometric compositions with diverse carbon contents under various conditions [141, 144-147]. Goretzki et al. [148], claimed that carbon atoms occupy ordered positions of $\text{TiC}_{0.5}$, which is a supercell with a twofold lattice constant of the subcell. It also was pointed out that a lower C/Ti atomic ratio (viz. x in TiC_x) can weaken atomic bonding strength (viz. Ti-Ti covalent bonds) in TiC_x to further reduce strength and hardness of TiC_x [149]. A face centered cubic structure of GB- $\text{TiC}_{0.5}$ (see **Figure 14**) and its platelet shape in β Ti-alloys was revealed and reconstructed by Yan et al. [141].

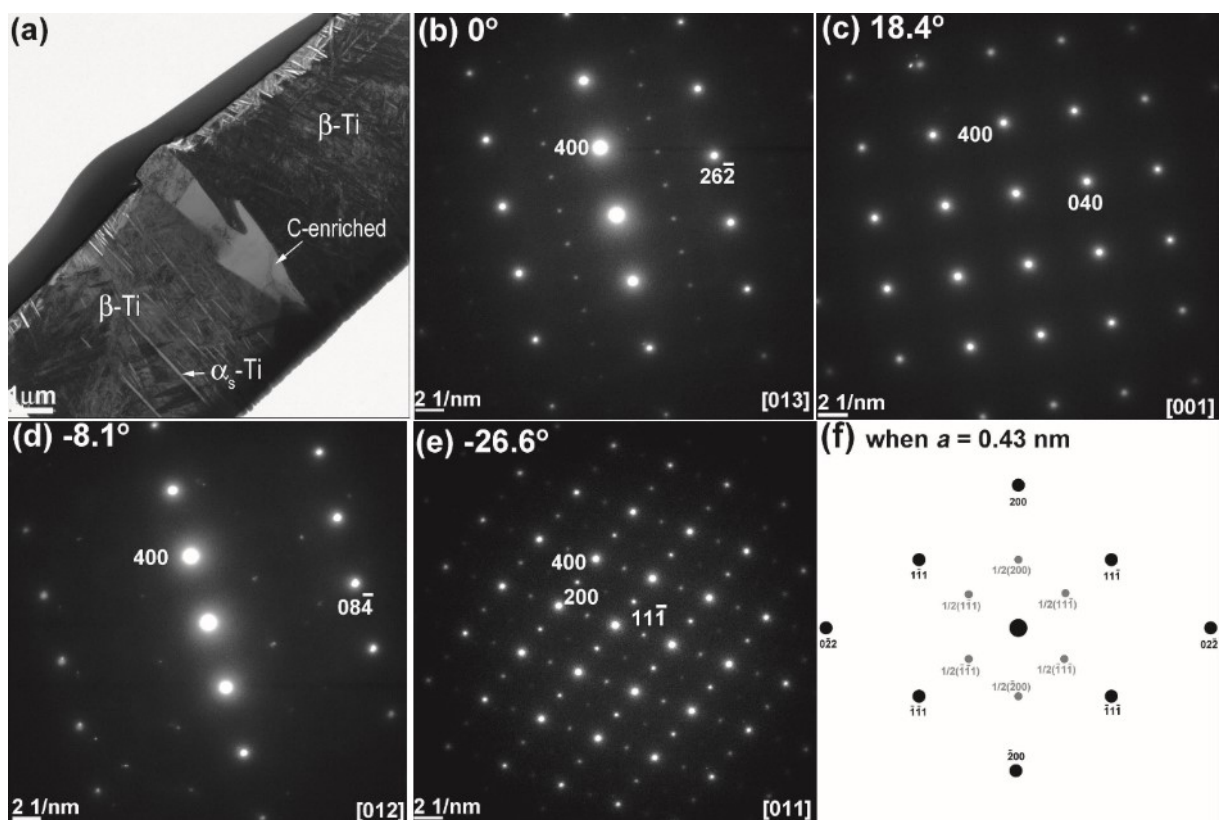


Figure 14 - (a) TEM-BF image of the β -Ti matrix, secondary α -Ti (α_s) and carbon-enriched GB phase (GB- $\text{TiC}_{0.5}$); (b) to (e) TEM-SAED patterns for GB- $\text{TiC}_{0.5}$; (f) Schematic graph [141].

A few researchers have proposed a solution to the premature fracture induced by GB- TiC_x by technical precautions against TiC_x formation and carbon contamination [61]. Water quenching and high-concentration alloying were indicated as effective to reduce the amount of TiC_x precipitation [110]. To use high-purity original powder, extremely high-purity argon flow in thermal debinding [55] and to run a thorough cleaning program for the debinding-sintering furnace (e.g. hydrogen charging burn-out/burn-off) are able to mitigate carbon uptake. However,

they may not be completely successful; these methods are typically cost-consuming and technically difficult to perform, or occasionally deteriorate certain mechanical properties.

Instead, a practical alternative that is much more feasible is to accept the existence of TiC_x and distribute the particles not at the grain boundaries but in the grain interior by optimized processing. A small quantity of intragranular TiC_x in β Ti-alloys was also observed in some studies [19, 99, 146, 150]. Optimizing the distribution of second-phase particles, e.g. adjusting aligned GB- TiC_x to dispersed intragranular TiC_x , was advised to likely enhance toughness [151, 152]. Lately, Lefebvre et al. [153] observed a positive effect from amorphous graphite addition on sintering densification, strength and elongation of PM CP-Ti and Ti-6Al-4V. All these properties were prominently improved due to even particle distribution combined with refinement mechanism. Nevertheless, there are only a few studies with respect to adjusting particle distribution, like TiB/ Al_2O_3 second-phase via thermomechanical processing [154, 155], which is not appropriate to low-cost near-net-shape powder technologies. Thus, the feasibility of adjusting TiC_x particles distribution will be investigated in this study.

2.4 Advanced sintering pathways

Establishing and updating sintering cycles aims to practically solve the three major processing defects of PM Ti alloys [156]. The other purpose of the advanced sintering pathways is to create engineered microstructures and application-tailored mechanical properties, directly in the as-sintered state of Ti-alloys [157]. Thereby avoiding unnecessary post-sintering treatment incl. thermomechanical processing and technically difficult heat treatments being more cost-saving by this.

2.4.1 RE-containing sintering cycle

In the past decades, there has been continuously increasing research on a variety of advanced structural materials where rare earth (RE) elements (or their compounds) were added to improve their mechanical properties or to realize specific functionalities [158-163]. Effects of RE addition can be summarized into at least the following three major points:

- i) A small amount of RE addition is capable of effecting mechanical properties of various materials through precipitation hardening [164]. For instance, RE has been introduced into unalloyed titanium and various titanium alloys for achieving enhanced mechanical

- performance at both room temperature and elevated temperatures. They can be processed by different routes such as rapid solidification [165], forging [166, 167], selective electron beam melting [168], metal injection molding [81] and so forth;
- ii) The presence of RE ceramic-phase is capable to refine the grain size of Ti-alloys by heterogeneous nucleation, grain boundary pinning effect [169] and/or growth restriction at high temperature [170, 171]. The resultant mechanical properties are much better than those without RE addition. In particular, microstructure refinement is of crucial importance for ensuring good fatigue performance of Ti alloys [115, 127]. Thus, grain refinement is one of the reasons why RE has been introduced to powder metallurgy (PM) of Ti-alloys [18, 111, 163, 164, 172-174].
 - iii) Different from ingot metallurgy (IM), oxygen contamination is not readily controllable in most PM-Ti alloys. It is well known that some important engineering materials such as Ti-6Al-4V and intermetallic Ti-Al display low tolerances for oxygen [127, 175]. For instance, a critical oxygen content of 3300 ppm (0.33 wt.%) is determined as the tough-brittle transition limit for the Ti-6Al-4V alloy. This value can be even lower (1500 ~ 2200 ppm) in the case of additively manufactured Ti-6Al-4V, if the microstructure consists of α' martensitic phase [124]. Oxygen degrades the ductility of titanium alloys via multiple mechanisms as summarised in Ref. [124]. To scavenge oxygen from Ti and mitigate its detrimental impact, a variety of RE elements have proved to be effective. It is shown that adding a small amount of RE can markedly increase the ductility of PM-Ti by 60% ~ 90% [111, 173].

To mitigate the oxygen problem, Y is a plausible choice, according to the oxygen scavenging capability of REs: $Y > Er > Dy > Tb > Gd$ [176, 177]. In addition, there is a benefit of low-cost [123]. The Ellingham diagram [178] confirms that Y_2O_3 (yttria) has a lower formation energy than TiO_2 , suggesting it can effectively scavenge oxygen from the Ti-matrix. A successful example of using Y can be found in [79], which shows that MIM Ti-6Al-4V alloys containing more than 4000 ppm oxygen can be fabricated by using inexpensive HDH master alloy powder (USD \$25/kg) and 0.5 wt.% Y addition (USD \$800/kg) with excellent tensile properties (UTS of 939 MPa, ϵ_f of 13.5%).

Y addition, however, may lead to an adverse effect, which is a higher amount of porosity [169, 179]. It is suspected that increasing porosity by Y addition is linked to the particle size of the used RE elemental powder. This issue still remains unclear to date. Also, no systematic work

was performed on the combined effect of oxygen scavenging, microstructure refinement and porosity increase by adding Y on tensile properties of PM Ti alloys. This study investigates the impact of added Y on the oxygen scavenging, β grains refinement, resultant porosity and tensile properties on MIMed β Ti-alloys, to acquire a systematic comprehension of the impact mechanisms of Y-containing methods.

2.4.2 Boron-containing sintering cycle and its particle distributions

The boron sintering cycle, as the name implies, through adding trace boron-containing powder to titanium-based powders to trigger *in situ* synthesis of titanium boride (TiB), can significantly affect the sintering process. It has been demonstrated by Ferri et al. [76, 115] in MIM Ti-6Al-4V to improve tensile and fatigue properties.

The distribution patterns of the TiB_w whiskers in PM Ti alloys that have been reported to date include: a) dispersed mode in most cases [115]; b) aligned adjustment by post-sintering hot extrusion [155]; c) quasi-continuous network architecture through *in situ* synthesizing TiB_w whiskers around particles boundaries that have a large particle size and a narrow range of particle size distribution (PSD) [180, 181]. Typical microscopic photographs are given below.

- a) The dispersed TiB_w whiskers are normally obtained by adding trace amounts of boron into as-sintered Ti alloys, which is able to improve the tensile strength, slightly reduces elongation, and significantly improves the fatigue endurance limit. For MIM Ti-6Al-4V, the tensile strength increased from 806 MPa to 902 MPa, the elongation decreased from 13.7% to 11.8%, and the fatigue strength increased from 450 MPa to 650 MPa in 10^7 cycles by adding merely 0.5 wt.% amorphous boron powder [115].
- b) Ti alloys with an aligned TiB_w whiskers microstructure result in anisotropic material properties, of which longitudinal specific stiffness and tensile strength can be significantly increased. For example, in PM Ti-6Al-4V containing 20 vol.% TiB_w whiskers after post thermomechanical processing, the TiB_w whiskers distribution was adjusted to be aligned. Its UTS increased from 1018 MPa to 1215 MPa and the stiffness increased from 145 GPa to 170 GPa [155].
- c) The concept of *in situ* synthesis TiB whiskers in Ti alloys filled by a network architecture was first proposed by Panda et al. [182] and Morsi et al. [183] as early as in 2002. Its main

purpose is to enhance the bonding strength of grain boundaries or particle boundaries. In 2009 and 2011, Huang et al. successfully prepared PM Ti-6Al-4V containing 2 vol.% TiB whiskers in network structure, which could increase the UTS from 855 MPa to 1021 MPa, and the elongation slightly decreased from 11.3% to 9.2%. When the volume fraction of TiB whiskers increased to 8.5 vol.%, the tensile strength increased to as high as 1288 MPa, but the elongation decreased to 2.6% [180, 181].

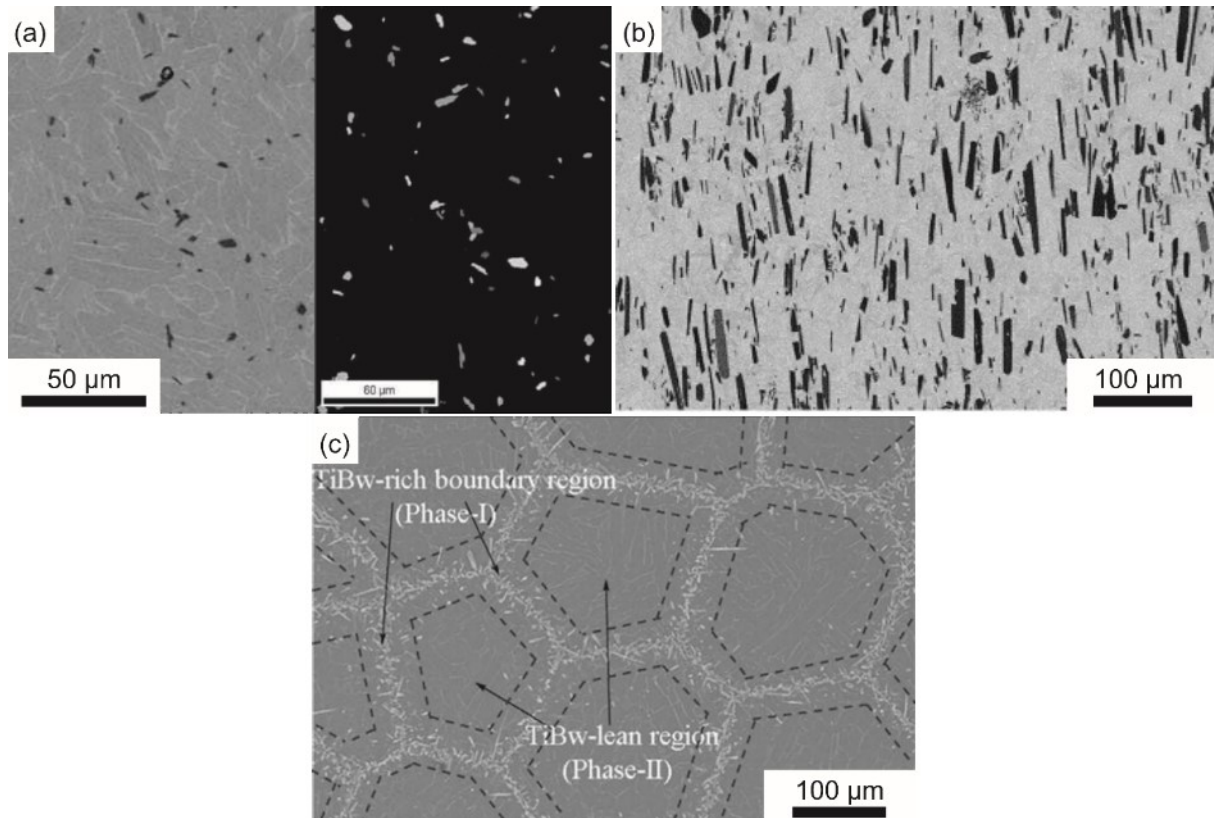


Figure 15 - Different distribution patterns of the TiB_w whiskers in PM Ti alloys including: a) dispersed mode in most cases [115]; b) aligned distribution [155]; c) quasi-continuous network architecture [180, 181].

3. Experimental

3.1 Alloy design and nomenclature

In this Ph.D. project, the original purpose of alloy design is to develop a biomedical Ti-alloy with low young's modulus, non-toxicity (or extremely low toxicity), and high biocompatibility for orthopedic applications. Considering the various toxicity of the β stabilizers (Section 1.1.3), their ability to lower elastic modulus of Ti alloys, the sinterability, and the long-term accumulated experience of the present lab in the relevant field, a further development of a metastable type Ti-20Nb-10Zr alloy (a β Ti-alloy) was undertaken. The research background (Section 1.3) has mentioned that there frequently are three major processing defects in the PM β Ti-alloys produced by the conventional sintering cycle pathways. Therefore, this study will aim on the development of advanced sintering pathways, i.e. a) to optimize the *Y-containing sintering cycle* (the most common RE-containing sintering cycle) to solve the problems of the coarse-grained structure and high oxygen pick up, and b) to design a new sintering cycle (*TiC_x-redistribution sintering cycle*) to deal with the embrittlement issue induced by carbon uptake to enhance the tensile and/or fatigue properties. The optimized and newly designed sintering pathways, the corresponding materials designation and their specific sintering programs are shown in **Table 7**.

Table 7 - The two developed sintering pathways, alloy abbreviations, the corresponding compositions and processing parameters.

Sintering pathways	Alloy abbreviations	Compositions (wt.%)	Sintering programs
a) Y containing (sintering cycle)	TZN20 (prototype)	Ti-20Nb-10Zr	1500 °C/4 hr (conventional)
	TZN20-0.3Y	Ti-20Nb-10Zr-0.3Y	1500 °C/4 hr
	TZN20-0.5Y	Ti-20Nb-10Zr-0.5Y	1500 °C/4 hr
	TZN20-0.7Y	Ti-20Nb-10Zr-0.7Y	1500 °C/4 hr
	TZN20-1.0Y	Ti-20Nb-10Zr-1.0Y	1500 °C/4 hr
b) TiC redistribution (sintering cycle)	TZN20 (prototype)	Ti-20Nb-10Zr	1500 °C/4 hr
	TZN20-CSRA	Ti-20Nb-10Zr	1500 °C/4 hr + CSRA step
	TZN20-0.1Y	Ti-20Nb-10Zr-0.1Y	1500 °C/4 hr
	TZN20-0.1Y&CSRA	Ti-20Nb-10Zr-0.1Y	1500 °C/4 hr + CSRA step
	*TZN18-0.1Y	Ti-18Nb-10Zr-0.1Y	1500 °C/4 hr
	*TZN18-0.1Y&CSRA	Ti-18Nb-10Zr-0.1Y	1500 °C/4 hr + CSRA step

*TZN18-0.1Y(&CSRA): reference group; CSRA: carbide spheroidization reprecipitation annealing, which is a behavior of phase transformation induced TiC redissolution.

3.2 Materials processing

3.2.1 Starting materials

Commercially-available pure Ti powder, usually called CP-Ti powder, (ASTM Gr.1, <45 μm , gas-atomized; spherical; TLS Technik, Bitterfeld, Germany), Ti-42Nb master-alloyed powders (<45 μm and <63 μm , spherical; H.C. Starck, Goslar, Germany [66]), elemental Zr powders (<45 μm , irregular; abcr GmbH, Karlsruhe, Germany and <45 μm , spherical; TLS Technik, Bitterfeld, Germany) and elemental Y powder (<45 μm , irregular; Edgetech Industries, Miramar, USA) were used as starting materials. The composition of the alloys was achieved by blending these metallic powders in the corresponding amounts. Ti-42Nb (wt. %) master powder was selected to support homogeneous sintering compared to using elemental powders. Additionally, according to the literature [184-186] yttrium (Y) and its oxide form (yttria, Y_2O_3) are moderately biocompatible and beneficial for maintaining the homeostatic equilibrium of human beings. In particular, the finer Ti-42Nb master-alloyed powder and the spherical Zr elemental powder are only employed for a few feedstocks, for the purpose of further reducing porosity, and those β Ti-alloys are specially labeled.

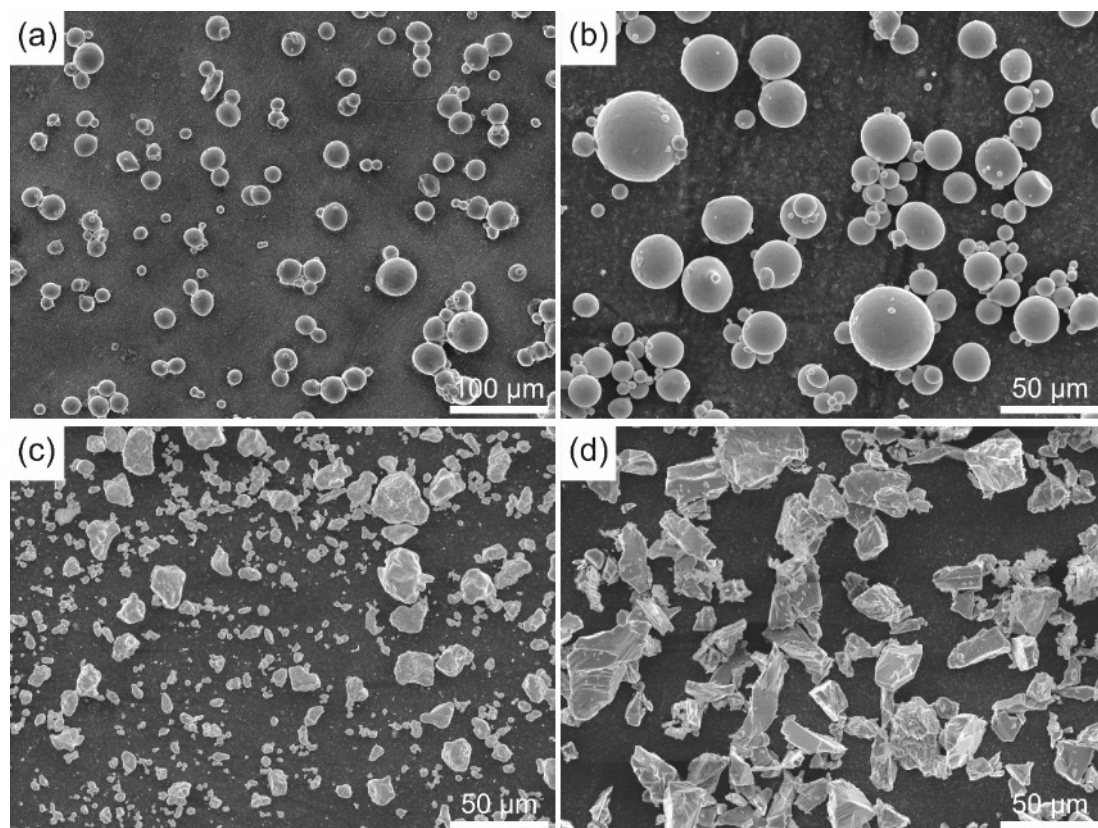


Figure 16 - Starting powders for most feedstocks: (a) CP-Ti powder; (b) Ti-42Nb; (c) Zr; (d) Y.

The SEM-SE images of CP-Ti powder, Ti-42Nb MA powder (<63 μm), elemental Zr powder (irregular) and elemental Y powder are shown in **Figure 16**. In addition, their interstitial impurities levels determined at HZG (as-measured) and those documented by the suppliers (as-received) are given in **Table 8**, revealing some differences. It is worth noting that the nitrogen content of powders obtained by the measurement of the inert gas fusion method applied at HZG tends to scatter in a rather large range in some cases.

Table 8 - Impurities levels of the starting powders.

Powder	Source	Carbon (ppm)	Oxygen (ppm)	Nitrogen (ppm)
CP-Ti powder	As-measured	59	1254	353
	As-received	80	900	50
Ti-42Nb MA powder	As-measured	63	3103	1237
	As-received	37	2674	90
Zr powder	As-measured	142	5075	2663
Y powder	As-measured	394	9928	13216

3.2.2 Polymeric binder system

A traditional binder system, i.e. EVA-backbone polymer, wax-based binder, was chosen in this study. The composition of the binder system was 35 wt.% polyethylene-co-vinyl acetate (EVA), 60 wt.% paraffin wax (PW) and 5 wt.% stearic acid (SA). Their physical and chemical properties are given in **Table 9**. The present binder system had been applied successfully before to other MIM-processed titanium alloys and titanium aluminides intermetallics resulting in sound mechanical properties [79, 99, 150, 187-189].

Table 9 - Ingredients of the binder system and their physical and chemical properties.

Ingredient	Melting point	Freezing point	Density	Chemical formula	Percentage
PW #1	42-44 °C	51-53 °C	0.9 g/cm ³	C _n H _{2n+2}	10 wt.%
PW #2	42-72 °C	57-60 °C	0.9 g/cm ³	C _n H _{2n+2}	50 wt.%
EVA	97 °C	n	0.93 g/cm ³	(C ₂ H ₄) _n (C ₄ H ₆ O ₂) _m	35 wt.%
SA	68-70 °C	n	0.94 g/cm ³	CH ₃ (CH ₂) ₁₆ COOH	5 wt.%

3.2.3 Feedstocks preparation

A mixture that comprised 65 vol.% the metallic powders (according to its specific composition) and 35 vol.% the binder system was blended in a double sigma-blades kneader (Femix KM 0.5K, Misch- und Knettechnik GmbH, Waiblingen, Germany) for 4 hours at a set temperature of 120 °C (112 °C measured) under controlled argon atmosphere. The atmosphere ($\text{H}_2\text{O} < 1$ ppm and $\text{O}_2 < 1$ ppm) was purified by a gas purification system (Böhler AG, Wien, Austria). The feedstocks of metal injection molding that consist of rather small-sized granulates were finally acquired after granulating in a crushing mill (Wanner Technik, Wertheim, Germany).

3.2.4 Metal injection molding (MIM)

According to the ISO 2740 specified standard, the “dog bone” shaped tensile specimens (see **Figure 17**) were metal-injection-molded by using a conventional ARBURG 320 S machine (Arburg GmbH & Co., Lossburg, Germany). The Ti-part after injection molding is usually called the green part. A maximum injection pressure of 135 MPa, a set injection muzzle temperature of 112 °C and mold temperatures of 43~45 °C were adopted during processing.

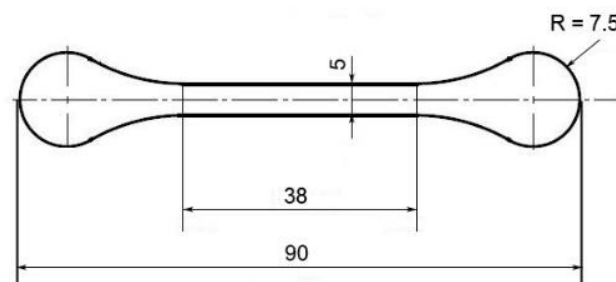


Figure 17 - The “dog bone” shaped cavity geometry of the molds for tensile tests, the dimensions are in (mm) [104].

3.2.5 Chemical debinding (1st step)

For traditional wax-based binder system, a two-stage debinding process (chemical and thermal debinding) is generally conducted on the green parts. Specifically, the chemical debinding firstly extracted the paraffin wax, and then thermal debinding vaporized the remaining polymers. In the solvent debinding, the green parts were immersed under hexane (VWR CHEMICALS, Radnor, USA) flow in a commercial debinding device (LÖMI LRA/EBA-50, Grossostheim, Germany) at 40~45 °C for 15 hours to remove the paraffin wax to create the capillarity effect in the next step.

3.2.6 Thermal debinding (2nd step) and sintering

The programs including thermal debinding, conventional-sintering cycle and newly-designed extra sintering cycle, i.e. carbide spheroidization reprecipitation annealing (CSRA), were continuously run in a high-vacuum debinding-sintering integrated furnace (XERION XVAC 1600, Freiberg, Germany). This cold-wall furnace was equipped with tungsten heating elements and shield packs of molybdenum, and all specimens were on the sintering support with a coated Y₂O₃ layer. In addition, a conventional high-temperature burn-out program was carried out, in order to technically keep the impurities contamination (mainly carbon and oxygen uptakes) as low as possible.

Thermal debinding (2nd debinding step) was performed with a heating rate of 2 K/min to 600 °C maximum temperature under slight argon flow (purity 99.996%, Linde AG, Munich, Germany) at a stable 5 mbar pressure. The as-sintered parts of all MIM β Ti-alloys in this study were obtained from a conventional-sintering cycle (1500 °C/4 h under 10⁻⁴ Pa vacuum, 5K/min heating rate and 10 K/min cooling rate). Such a controlled cooling rate is beneficial to near-equilibrium phase transition and to avoid overgrowth of β grains. Regarding the layout of the TiC_x-redistribution sintering cycle, the novel CSRA (800 °C/1 h under vacuum, 10K/min heating rate and 2 K/min cooling rate, here both mentioned thermal profiles are given in **Figure 18**) was performed subsequently on some of the as-sintered parts of β Ti-alloys incl. TZN20, TZN20-0.1Y and TZN18-0.1Y, which are referred to as: TZN20-CSRA, TZN20-0.1Y&CSRA and TZN18-0.1Y&CSRA, respectively. In order to ensure comparable carbon uptakes for all specimens in the TiC_x redistribution investigation, the CSRA program was conducted separately from the sintering cycle instead of being incorporated.

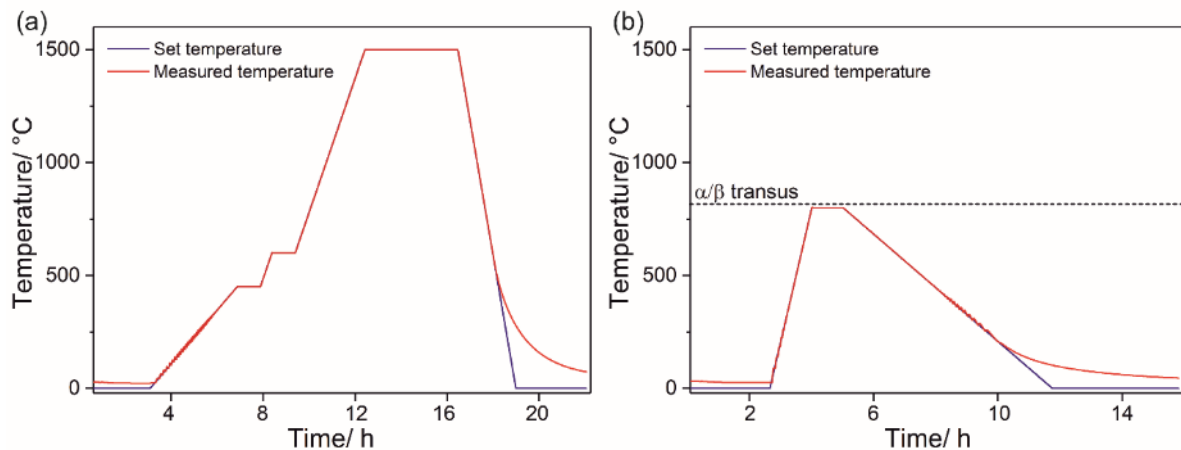


Figure 18 - Thermal profiles of the sintering programs used for: (a) the conventional sintering cycle; (b) the CSRA heat treating step in the novel TiC_x -redistribution sintering pathway, where the α/β transus is at ≈ 810 °C [107].

3.2.7 Traditional press-and-sintering

To investigate the additional pick up of impurities, when binder is used in PM Ti alloys, binderless pressed and sintered samples (\varnothing 8 mm \times height \approx 6 mm) were molded by using a press force of 2.5 kN via a hydraulic press (Enerpac, Menomonee Falls, USA). The utilized powders were exactly the same as the above-described MIM TZN20 and TZN20-0.1Y alloys. These cylindrical samples were consolidated via running the conventional sintering program as described before. A vacuum burn-out program, for cleaning the furnace, was also carried out prior to every sintering cycle.

3.3 Materials tests and characterization

3.3.1 Mechanical properties tests

The uniaxial tensile tests of all MM β Ti-alloys were conducted in air at ambient temperature in a servo-hydraulic tensile testing machine (RM-100, Schenck-Trebel, Deer Park, USA). This machine is modernized with a Zwick DUPS electronic testing system and equipped with a 100 kN load cell and a non-contact laser extensometer (WS 160, Fiedler Optoelektronik GmbH, Lützen, Germany). Tensile properties (incl. yield strength (YS), ultimate tensile strength (UTS), ε_f (elongation to fracture) and Young's modulus) were determined for three “dog bone” MIM β Ti-alloys-parts under strict quality control (i.e. parts with abnormal density will be discarded) with a changing strain rate (specifically 0.2 mm/min in elastic region, 0.3 mm/min at yield point,

and 0.5 mm/min during plastic deformation). The gauge length was ≈ 30 mm and the gauge diameter was ≈ 4.2 mm. The true stress-strain curves were derived from the engineering stress-strain curves. The area underneath the engineering stress-strain curves was determined as a measure for the tensile toughness of MIM TZN20-xY alloys by using OriginLab software.

3.3.2 Interstitial levels determination

The concentrations of carbon, oxygen and nitrogen were determined of: i) starting powders, ii) pressed and sintered parts and iii) MIM-processed parts (incl. as-sintered and CSRAed) for unveiling impurity levels and the sources of contamination. In brief, six ultrasonic-cleaned specimens corresponding to each state were measured with two analysis devices (LECO CS-444 and TC-436AR, Saint Joseph, USA).

The oxygen equivalent, $O_{eq.}$, of TZN20-xY was calculated from the mean value of the measurements by Eq. (1). Besides, the partial $O_{eq.}$ value contributed by carbon and nitrogen of MIM β Ti-alloys produced by Y-containing method were also calculated, as represented by blue symbols in **Figure 19** in Section 4.1.1 and listed in **Table 11**. The solid solution oxygen equivalent, $O_{sseq.}$, was estimated by Eq. (2), according to the principle of oxygen scavenging by Y particles, i.e. 0.1 wt.% Y to react with 0.027 wt.% oxygen [79]. And C_Y denotes the concentration of Y.

$$O_{sseq.} = O_{eq.} - 0.27 \times C_Y \quad (2)$$

3.3.3 Porosity / relative density

The densities and porosities of the as-sintered β Ti-alloys parts were determined by the Archimedes' principle specified in ASTM B962 using an electronic balance (Sartorius AG, Göttingen, Germany). The theoretical compact densities were calculated considering the density of each element and its volume fraction [190]. The theoretical densities of main β Ti-alloys in the study on the TiC_x redistribution sintering cycle are given in **Table 10**.

Table 10 - Theoretical densities of main β Ti-alloys.

β Ti-alloy	Composition	Theoretical density (g/cm ³)
TZN20(-CSRA)	Ti-20Nb-10Zr	5.15402
TZN20-0.1Y(&CSRA)	Ti-20Nb-10Zr-0.1Y	5.15398

In order to estimate the mean diameter and the form factor of porosity, three images containing approximately 150 pores for each alloy were analysed by Image J pro software. For analyzing the irregular degree of porosity, the shape of these pores was defined by Eq. (3) [187, 188]. A form factor of 1 represents a circular pore in the planar view.

$$Form\ factor = \left(\sqrt{\frac{area}{\pi}} \times \frac{2\pi}{perimeter} \right)^2 \quad (3)$$

3.3.4 Microstructural characterization

To explore the as-sintered microstructure of MIM β Ti-Ti-Nb-Zr alloys produced by the Y-containing method and TiC_x redistribution pathway, all metallographic samples were cut from MIM-processed “dog bone” tensile specimens. After completing tensile tests, for preparing the metallographic samples to investigate the fracture profile (i.e. the longitudinal section of fractured tensile samples) of β Ti-alloys, the MIM-parts exhibiting the median elongation value in every group were cut along the central axis. They were ground with SiC abrasive papers (Schmitz-Metallographie, Herzogenrath, Germany), polished with neutral OPS solution (Cloeren Technology, Wegberg, Germany) by an automatic grinding and polishing machine (TegraPol-35, Struers GmbH, Willich Germany), then ultrasonically cleaned in pure ethanol (Merck KGaA, Darmstadt, Germany). Additionally, the corresponding samples with the tensile fracture surface are also cut to the appropriate size for facilitating materials characterization by the microscopes.

An optical microscope (OM) (Olympus PMG3, Tokyo, Japan) and a scanning electron microscope (SEM) (Tescan Vega3 SB, Brno, Czech) equipped with energy-dispersive spectroscopy (EDX) were used for microstructural characterization and tensile-fractured (strain-induced) fractographic study. Furthermore, chemical element mappings focusing on the GB- TiC_x phase, the intragranular TiC_x phase, the pore- Y_2O_3 particles and the interior- Y_2O_3 particles are performed. These compositional analyses to preliminarily determine the consistency of chemical composition of two kinds of TiC_x phases or two kinds of Y_2O_3 particles. The mathematical conversion of the elemental weight percentages from the mapping data was carried out by Iridium Ultra software. Electron backscatter diffraction (EBSD) (Zeiss Ultra 55, Carl Zeiss AG, Germany) was applied to verify the location of TiC_x precipitates, which are either on the grain boundaries or inside the β grains. An area of $150 \times 300 \mu m^2$ was scanned at

15 kV for 22 h in TZN20, TZN20-CSRA, TZN20-0.1Y, and TZN20-0.1Y&CSRA to investigate the TiC_x redistribution.

Average prior β grain size determined for three images of etched samples (via using “Kroll Reagent”) were measured manually with the 'intercept module' of Olympus Soft Imaging Solutions analysis Pro. The volume fraction of TiC_x second-phase particles was calculated from five 200x optical pictures, and their particle features such as aspect ratio, mean particle size, and corresponding distribution curves were acquired by using Image J analysis and OriginLab software. The particle size distribution of two kinds of yttria was determined from three 500x SEM-images and analyzed by Image J analysis.

3.3.5 *In situ* high energy X-ray diffraction (synchrotron)

In order to investigate the evolution of precipitation of TiC_x during cooling, *in situ* high-energy X-ray diffraction experiments were performed at the HEMS beam line run by Helmholtz-Zentrum Hereon (Geesthacht) at the PETRA III of Deutsches Elektronen-Synchrotron (DESY) in Hamburg. The X-ray beam had a cross-section of $5 \times 5 \text{ mm}^2$ and photon energy of 87.1 keV corresponding to a wavelength of 0.14235 Å. The cylindrical specimens ($\varnothing \approx 4.5 \text{ mm} \times$ height 10 mm) of MIM-processed TZN20 and TZN20-0.1Y were measured in transmission. The diffractograms of Debye-Scherrer diffraction rings with an exposure time of 0.5 s were recorded every 15 s using a PerkinElmer XRD 1622 flat panel detector (2048×2048 pixels, pixel size = $200 \times 200 \mu\text{m}^2$). The specimens were heated up to 1000 °C in a vacuum and held for 15 minutes until all carbides were dissolved and no carbide peak was detectable anymore. Subsequently, these specimens were cooled to 600 °C at 2 K/min, and afterwards quenched to 25 °C by fast cooling. As a measure for the precipitation percentage of carbides, the reflection intensities of the carbide peak of the (220) reflection was taken at different temperatures and compared to the intensity of that peak at ambient temperature. However, the strong intensities of the (111) and (200) reflections from the carbides were not used to quantify the carbide fraction, due to the interferential surrounding background intensity from α -Ti and β -Ti peaks. The series of two-dimensional diffraction data obtained from the flat panel detector were converted into series of one-dimensional diffraction patterns (2θ versus intensity) using an analysis software (Fit2D, Andy Hammerley).

4. Results

4.1 Y-containing sintering cycle of MIM β Ti-alloys

4.1.1 Oxygen equivalent $O_{eq.}$ and solid solution oxygen equivalent $O_{sseq.}$

Impurity levels (including carbon, nitrogen and oxygen) in the MIM-processed TZN20-xY alloys ($x = 0, 0.3, 0.5, \dots, 1$) are summarized in **Table 11**. The alloys differ only slightly in the content of C, N and O. It is also worth mentioning that NRC-IMI laboratory has found that even if the elemental analysis test by inert gas fusion method is performed under a good training and monitoring condition, the experimental error of LECO device is still as high as 4.4% (a relative deviation of 1.5% of measured values is given by the manufacturer) [120]. This is higher than the difference of values in **Table 11**. The calculated oxygen equivalent values ($O_{eq.}$) of all MIM-processed TZN20-xY alloys (see **Figure 19**) are basically unchanged.

Table 11 - Measured impurities levels of TZN20-xY alloys ($x = 0, 0.3, \dots, 1$), oxygen equivalent ($O_{eq.}$) and calculated solid solution oxygen equivalent ($O_{sseq.}$) (unit: weight %) [191].

Materials composition	C	O	N	$O_{eq.}$	$O_{sseq.}^*$
TZN20	0.047 ± 0.003	0.265 ± 0.001	0.082 ± 0.003	0.460	0.460
TZN20-0.3Y	0.043 ± 0.001	0.266 ± 0.003	0.081 ± 0.014	0.457	0.376
TZN20-0.5Y	0.049 ± 0.003	0.265 ± 0.009	0.081 ± 0.003	0.460	0.325
TZN20-0.7Y	0.045 ± 0.004	0.253 ± 0.004	0.075 ± 0.004	0.433	0.244
TZN20-1.0Y	0.050 ± 0.001	0.271 ± 0.010	0.077 ± 0.001	0.458	0.188

* The solid solution oxygen equivalent, $O_{sseq.}$, was calculated by Eq. (2), according to 0.1 wt.% yttrium (Y) scavenging 0.027 wt.% oxygen (O) from solid solution in Ti-matrix. And C_Y denotes the concentration of yttrium (Y).

The corresponding $O_{sseq.}$ (solid solution oxygen equivalent), however, changes due to the formation of yttria particles (Y_2O_3) and the resultant reduction in solid solution oxygen (Dissolved-O) in the Ti-matrix (**Figure 19**). It is noted that, after adding 1 wt.% Y, the $O_{sseq.}$ in the MIMed TZN20-1.0Y is reduced by as much as almost 60% compared with the original TZN20 without Y addition.

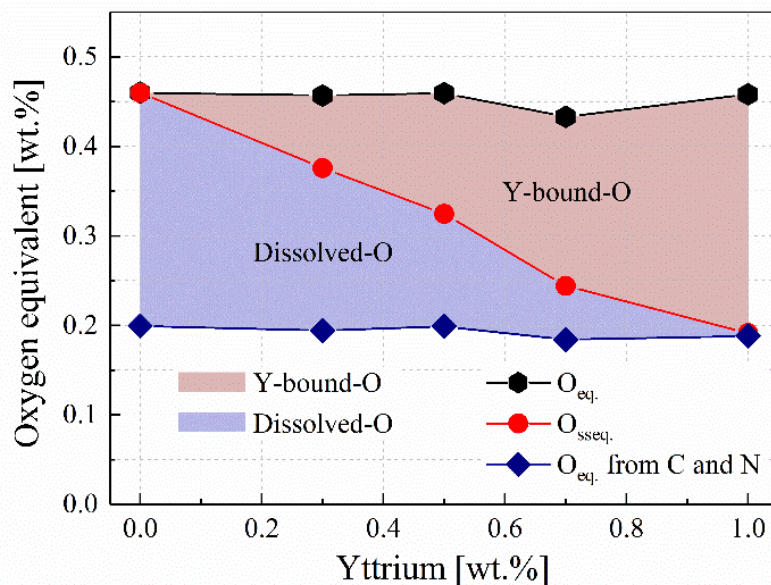


Figure 19 - The solid solution oxygen equivalent $O_{sseq.}$ (red symbols), oxygen equivalent $O_{eq.}$ from all interstitials incl. C, N, O (black symbols) and oxygen equivalent $O_{eq.}$ from C and N segments (blue symbols) in MIM-processed TZN20-xY alloys with different Y weight fractions ($x = 0, 0.3, 0.5, \dots, 1$). The light red-colored region represents how much oxygen has reacted with Y to form yttria and become Y-bound-O, whereas the light blue-colored region represents how much oxygen was in solid solution in the Ti-matrix (dissolved-O) [191].

4.1.2 Influence of Y on microstructural features

The typical microstructures of the as-sintered MIM-TZN20-xY alloys pictured by optical microscopy are shown in **Figure 20**, where the black-colored areas are the residual porosity and the gray-colored spots are for TiC second-phase precipitates. As-sintered Y free TZN20 (**Figure 20** (a)) exhibits apparently less pores than the alloy variants with Y addition (**Figure 20** (b) to (e)). More, larger and interconnected pores (marked by red triangles in **Figure 20** (e)) appear in TZN20-1.0Y alloys with high concentrations of Y. The detailed mechanism of TiC second phase precipitation resulting from carbon contamination is described in the discussion sections.

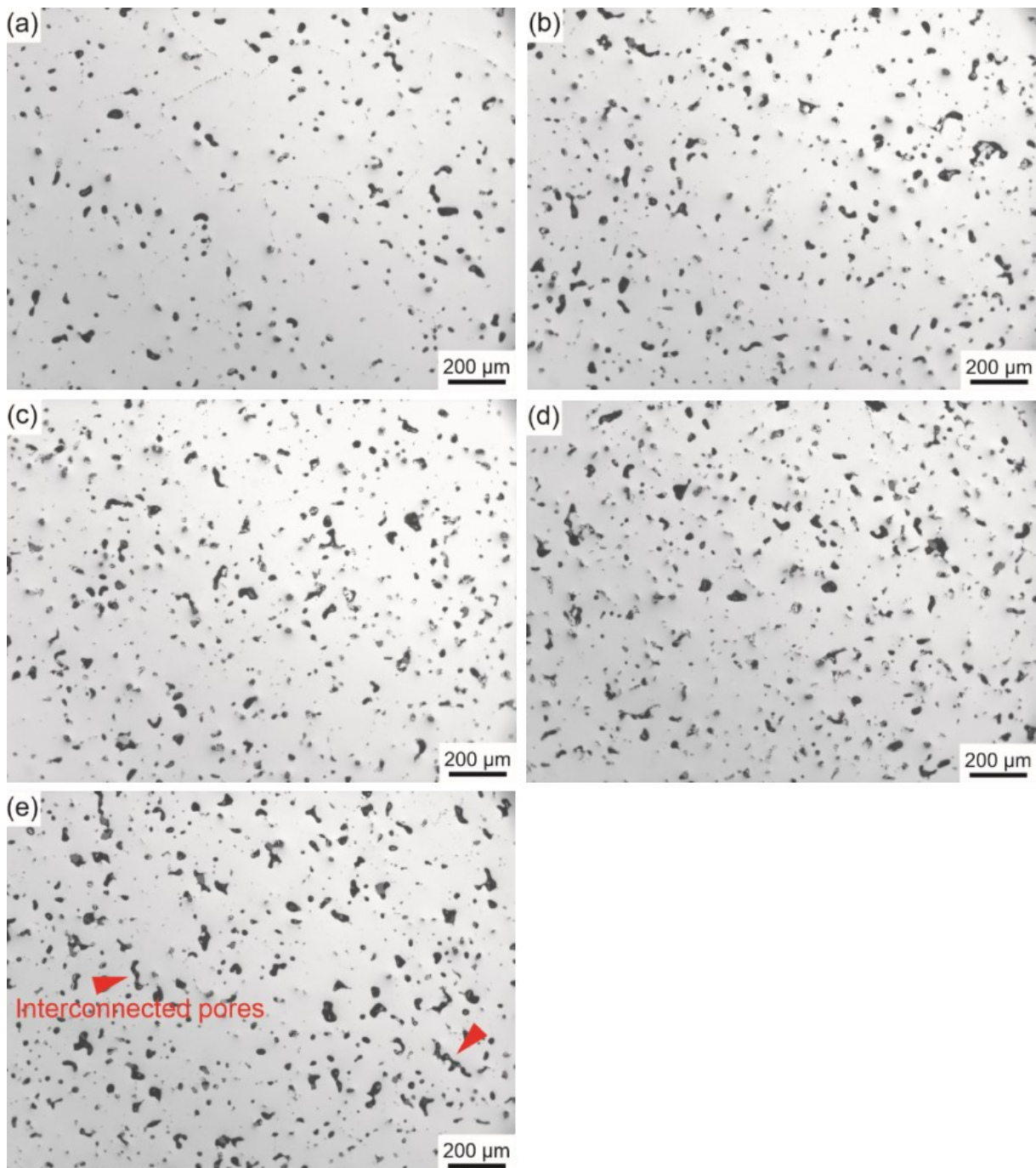


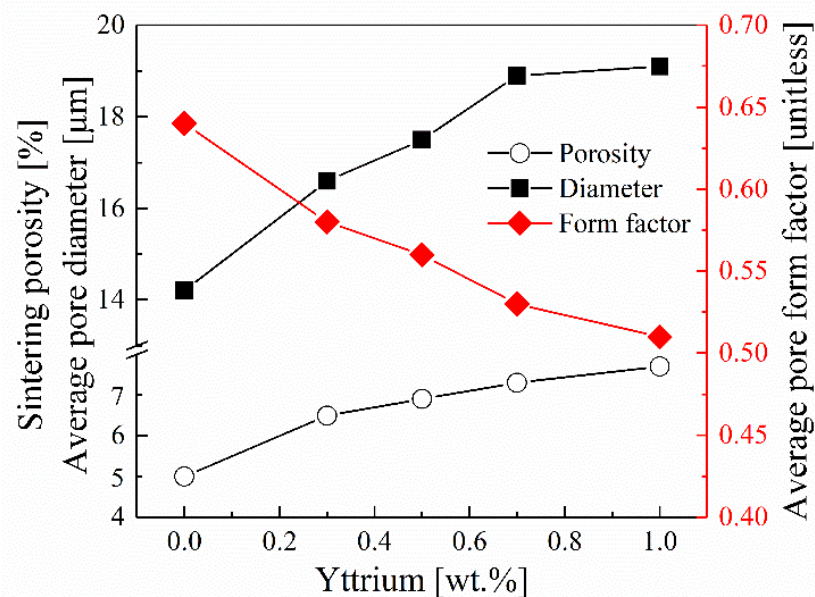
Figure 20 - Optical micrographs of TZN20-xY alloys: (a) TZN20; (b) TZN20-0.3Y; (c) TZN20-0.5Y; (d) TZN20-0.7Y; and (e) TZN20-1.0Y. The interconnected pores appear in high-Y-added TZN20-1.0Y alloys, pointed out by red triangles [191].

Table 12 lists the corresponding physical and microstructural characteristics, including sintering densities, porosities, average pore diameter and their form factor, mean β -grain size and titanium carbides (TiC) area fraction of MIM-fabricated TZN20-xY alloys.

Table 12 - Physical and microstructural properties of MIM-fabricated TZN20-xY alloys [191].

Alloy	Sinter density (g/cm ³)	Porosity (%)	Average pore diameter (μm)	Average pore form factor (-)	Grain size (μm)	TiC (area fraction %)
TZN20	4.89	5.0	14.2	0.64	373 ± 12	0.53 ± 0.05
TZN20-0.3Y	4.82	6.5	16.6	0.58	222 ± 5	0.52 ± 0.02
TZN20-0.5Y	4.80	6.9	17.5	0.56	212 ± 15	0.55 ± 0.07
TZN20-0.7Y	4.77	7.3	18.9	0.53	201 ± 20	0.58 ± 0.06
TZN20-1.0Y	4.75	7.7	19.1	0.51	187 ± 17	0.54 ± 0.11

The porosity parameters (including mean porosity size and pores form factor) of TZN20-xY alloys with different Y additions are analyzed and plotted in **Figure 21**. A rather strong relationship is found between the Y content and the porosity parameters. Adding 1 wt.% Y causes the sintering porosity fraction to rise by more than 50% and the average pore diameter to increase by ≈35%, respectively, compared with the Y free alloy variant. On the other hand, as Y concentration increases, the overall pores tend to be more irregular, according to the calculated pore form factor.

**Figure 21** - Influence of yttrium (Y) concentration on the porosity features (including mean porosity size and pores form factor) of the as-sintered MIM-TZN20-xY alloys [191].

On the basis of the metallographic observation regarding the morphology and spacial distribution (i.e. site relationship with porosity) of the yttria particles, it is discovered that yttria particles distribute either in the interior of the Ti-matrix (denoted as interior-yttria) or close to the pores (pore-yttria). In order to determine their chemical composition, an EDS mapping analysis is shown in **Figure 22**. From sample preparation some metal debris can be deposited in larger pores which is encircled by a dashed line.

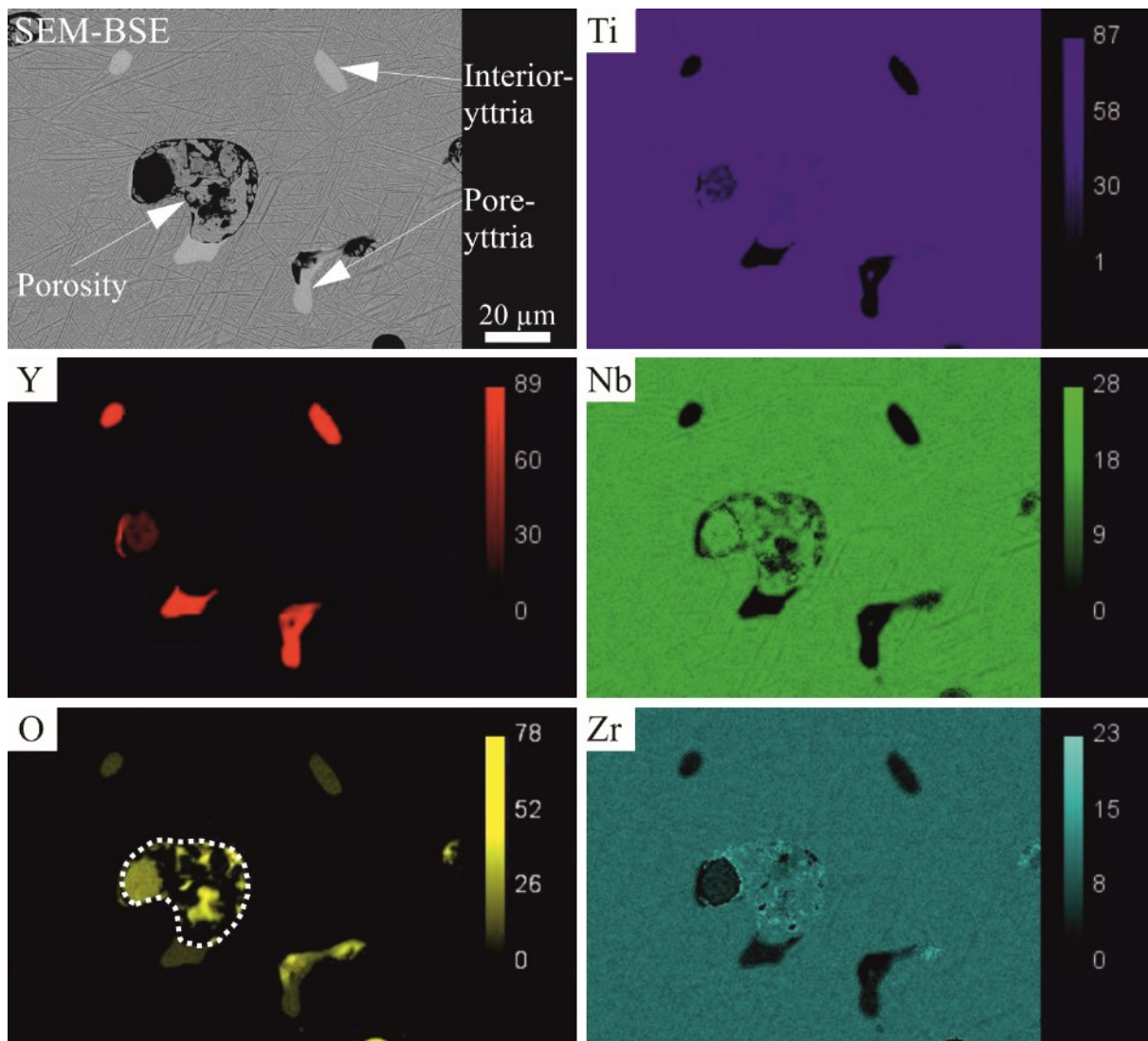


Figure 22- SEM-BSE image and chemical element mappings of two kinds of yttria particles (interior-yttria and pore-yttria) in MIMed TZN20-1.0Y alloy. Unavoidable metallic debris is encircled by white-colored dash line [191].

Y and oxygen contrasts are readily detectable, regardless of stemming either from interior-yttria or from pore-yttria. Since no significant difference between these two kinds of yttria is

visible, they are considered as compositional equal, suggesting only one type of Y-O oxide is formed. Furthermore, the Ti, Nb and Zr concentrations are considerably reduced in the yttria particles (see **Figure 22**). This result is in good agreement with the previous research that no Y-titanate such as $Y_2Ti_2O_7$ and Y_2TiO_5 was found in Y-added Ti-6Al-4V alloys by high-energy X-ray diffraction [112]. It further implies that yttria may have hindered the elemental diffusion and pore closing during sintering. However, the size and amount of interior-yttria are small, thus, it is unclear how large this effect actually is.

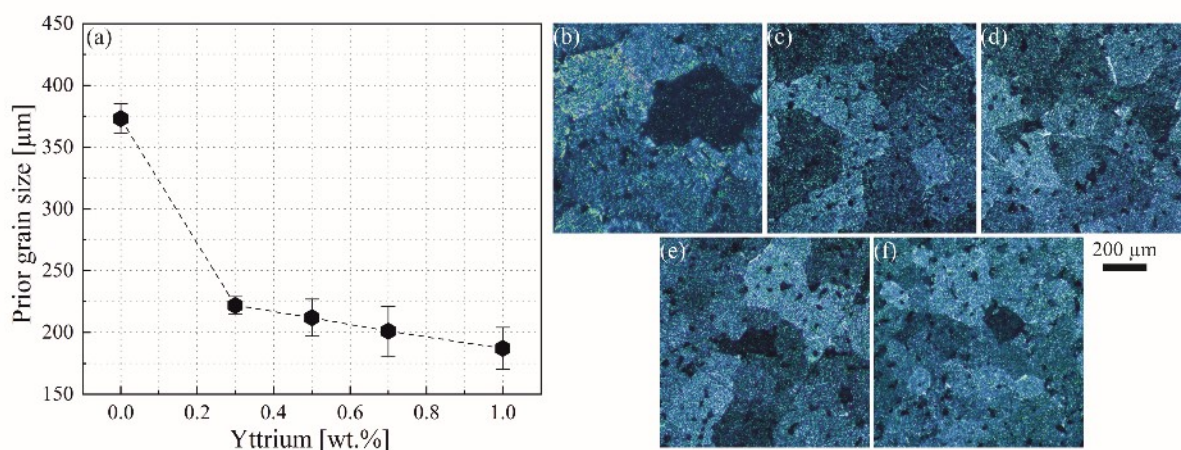


Figure 23 - Influence of yttrium (Y) on prior β grain size of as-sintered MIM TZN20-xY alloys. With only a small amount of Y addition, the prior β grain size is reduced significantly. (a) Mean value of prior β -grain size; Representative micrographs of etched specimens of (b) TZN20; (c) TZN20-0.3Y; (d) TZN20-0.5Y; (e) TZN20-0.7Y; and (f) TZN20-1Y, indicating the change of grain size [191].

Figure 23 indicates a significant difference between β grain size of the Y free TZN20 alloy variant and that of the TZN20 alloys with Y addition. Even a small amount of Y (0.3 wt.%) can cause a significant grain refinement effect by approximately 40%. The reduction of prior β grain size is likely attributed to two kinds of refinement mechanisms caused by the formation of yttria phases. From the inspection of micrographs of Y-added TZN20 alloys, only the pore-yttria (large yttria combined with porosity) is present at the grain boundaries (GBs), and few separate interior-yttria located at GBs are discovered. It is thus plausible that the early-formed interior-yttria acts as additional nucleation sites, whereas large pore-yttria particles associated with porosity work as β grain growth inhibitors. Moreover, there is no evidence that yttria particles can independently inhibit prior β grain growth via pinning grain boundaries. Because the number of yttria particles depends on the Y concentration, the TZN20-1.0Y alloy exhibits

the finest grain size. The refined microstructure in turn should have an impact on the mechanical performance, which will be detailed in the next section.

Figure 24 shows the carbon content and area fraction of the TiC second phases in the MIM TZN20-xY alloys. It is noted that an increase of Y concentration has no significant effect on the precipitating fraction of the TiC phase or carbon solubility in the Ti-matrix. It can be inferred that at room temperature solid solution oxygen (dissolved-O) has no practical influence on the carbon solubility, even though more interstitial sites are present due to oxygen atoms being scavenged by Y.

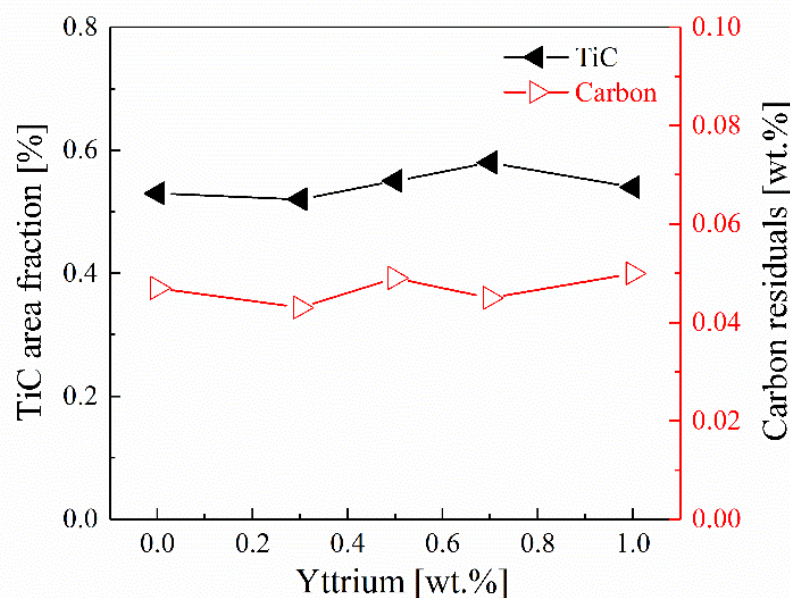


Figure 24 - Total carbon content and area fraction of the TiC phase precipitates in MIM TZN20-xY alloys are basically unchanged [191].

4.1.3 Influence of Y on tensile properties

Tensile properties of the MIM-processed TZN20-xY β Ti-alloys biomaterials are summarised in **Table 13**. The increase in porosity reduces the effective cross-sectional area for load bearing, leading to physical reduction in strength and Young's modulus. This decrease in Young's modulus is in general agreement with a previous study [84]. Ytria (Y_2O_3), although its Young's modulus is 170 GPa high [192], does not practically increase Young's modulus. Instead, the measured Young's modulus values of TZN20-xY alloys (≈ 67 GPa) are rather low

compared to other Ti-alloys [3, 11, 12], which is beneficial to avoid the “stress-shielding” effect in orthopaedic applications.

Table 13 - Tensile properties of MIM TZN20-xY alloys [191].

Alloy	Young's modulus (GPa)	Yield strength (MPa)	Ultimate tensile strength (MPa)	Elongation (%)	Toughness ($\text{J}\cdot\text{mm}^{-3}$)
Ti2010	71 ± 2.9	768 ± 3.9	889 ± 3.9	3.9 ± 0.5	39.3 ± 4.7
Ti2010-0.3Y	69 ± 2.5	715 ± 7.1	843 ± 4.8	5.0 ± 1.1	46.0 ± 8.1
Ti2010-0.5Y	67 ± 3.5	690 ± 3.3	816 ± 1.5	4.4 ± 0.6	40.0 ± 4.4
Ti2010-0.7Y	62 ± 2.7	649 ± 4.4	776 ± 5.3	4.1 ± 0.7	35.3 ± 4.7
Ti2010-1.0Y	61 ± 2.0	612 ± 7.5	738 ± 2.2	3.3 ± 0.6	28.1 ± 3.6

The results shown in **Table 13** of the mechanical properties (incl. yield strength (YS), ultimate tensile strength (UTS), elongation (ϵ_f) and tensile toughness) are plotted in **Figure 25**.

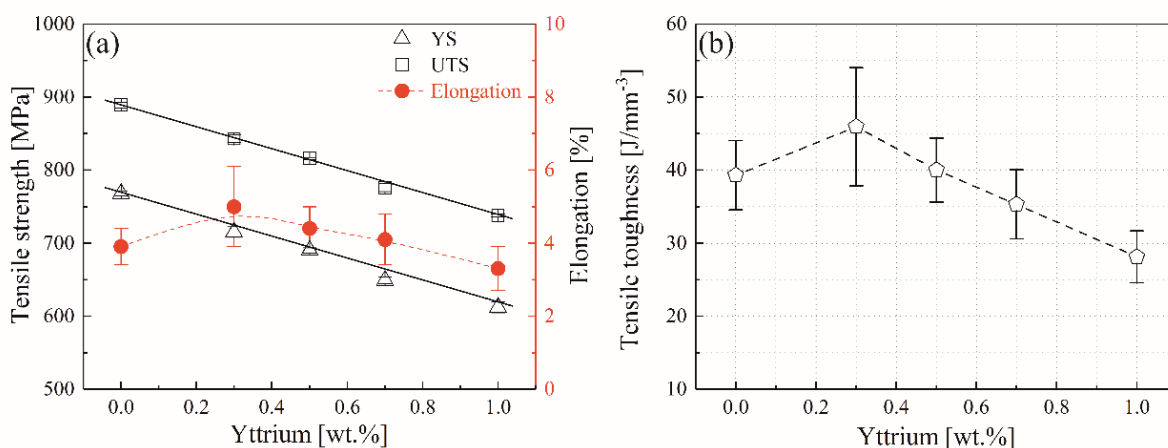


Figure 25 - (a) Influence of yttrium (Y) concentration on the tensile strength (incl. YS and UTS) and elongation to fracture (ϵ_f) of MIM-processed TZN20-xY alloys; (b) Tensile toughness of TZN20-xY alloys [191].

The tensile strength decreases monotonously with increase of the Y concentration. At first glance, this decrease is surprising, since a more refined microstructure is found in the TZN20 alloys with Y addition. However, the grain size appears not to contribute much in this case. The most likely reason is the evidently increased porosity as well as reduced solid solution strengthening by interstitially dissolved oxygen, which overcompensates any positive effects

of the smaller grain size. Corresponding ductility (**Figure 25 (a)**) and tensile toughness (**Figure 25 (b)**) show a similar tendency. Scavenging of oxygen by Y addition can improve the ductility of MIMed TZN20-xY by effecting the deformation mode (see Section 1.3.3). However, excessively high porosity (more than 6%) and the presence of interconnected pores largely degrade the ductility as well as the fracture toughness if the Y concentration is increased too much. A reduced ductility caused by an excess amount of Y can completely obliterate the enhancement of the deformation capability of the Ti-lattice that otherwise will benefit from oxygen scavenging.

4.2 Design of TiC redistribution sintering cycle

4.2.1 Carbon contamination sources

The results on basic impurity levels of as-sintered and CSRAed TZN20(-0.1Y) alloys and TZN18-0.1Y alloys (reference group) are listed in **Table 14**. The carbon contents were essentially the same, varying over a small range near 0.05 wt.%, which is considered as the standard amount of carbon residual for Ti-MIM. Residual amounts of carbon derived from several sintering cycles exhibit a basically repeatable level. Also, the minor differences of their oxygen or nitrogen concentrations are negligible. There seems to be no significant influence of the extra CSRA exposure and the slightly varying alloy compositions on interstitial contents. Moreover, the volume fractions of TiC_x in TZN20 series were essentially constant (≈ 0.5 vol.%) regardless of CSRA or Y, whereas the TZN18 series just shows almost half of the amount in comparison to the TZN20 series. That is because that as the Nb content increases in β -Ti alloys, the carbon solubility decreases, thereby raising more TiC_x particles [84]

Table 14 - Impurity levels and TiC_x volume fraction of as-sintered and CSRAed MIM-TZN alloys [107].

Samples	Carbon/ wt.%	Oxygen/ wt.%	Nitrogen/ wt.%	TiC_x fraction/ %
TZN20	0.047 ± 0.003	0.265 ± 0.001	0.082 ± 0.003	0.53 ± 0.05
TZN20-CSRA ¹	0.049 ± 0.002	0.258 ± 0.004	0.085 ± 0.005	0.51 ± 0.04
TZN20-0.1Y ²	0.053 ± 0.005	0.249 ± 0.010	0.076 ± 0.007	0.48 ± 0.10
TZN20-0.1Y&CSRA ³	0.043 ± 0.002	0.245 ± 0.006	0.050 ± 0.006	0.50 ± 0.09
TZN18-0.1Y ²	0.043 ± 0.011	0.275 ± 0.003	0.076 ± 0.002	0.25 ± 0.05
TZN18-0.1Y&CSRA ³	0.042 ± 0.003	0.279 ± 0.004	0.079 ± 0.002	0.24 ± 0.08

¹ CSRA has an extra sintering cycle step, which was programmed into the last step of the conventional sintering cycle.

² 0.1 wt.% Y powder was added into the metallic powder mixture.

³ Both CSRA¹ and Y² processes were carried out.

Comparing the results on carbon contents in **Table 15** indicates to what extent starting powders, debinding process and sintering atmosphere contributed to carbon contamination in the final MIM β Ti-alloys components. Unexpectedly, the final carbon residuals in binderless pressed and sintered parts were higher than in the binder-based MIM parts. Oxygen residue was in line with this tendency as well (≈ 0.32 wt.%, extra 0.05 wt.% oxygen). It may imply that the improper thermal pyrolysis of polymers in the debinding process did not contribute too strongly to carbon contamination, but sintering atmosphere plays the critical role. Previously, it was reported that sintering (incl. atmosphere and support) contributed to the majority of oxygen contamination in Ti-6Al-4V (<45 μm -sized pre-alloyed powder) [120]. Although a burn-out step is carried out prior to sintering cycle of MIM, ashes of organic materials may still remain trapped in the complex-shaped inner walls of the chamber of the debinding-sintering furnaces. In this case, it was difficult for the pressed and sintered parts, obtained by lower pressure molding, to attain a powder loading as high as the MIM technology. Consequently, comparatively low densification ($\approx 90\%$) and large external surface of the pressed and sintered Ti-parts lead to a higher possibility of atmospheric exposure and accordingly contamination than for the MIM-parts. Ebel et al. [193], advised that placing oxygen traps like titanium sponge with high surface area is helpful for reducing the contamination uptake from sintering atmosphere. It can be expected that the same means work to trap carbon.

Table 15 - Carbon residuals of powder metallurgical TZN20(-0.1Y) specimens under various conditions [107].

Sample type	Conditions	TZN20/ wt.%	TZN20-0.1Y/ wt.%
i) Starting materials	unsintered	0.007 ± 0.001	0.007 ± 0.001
ii) Pressed and sintered parts	binderless ($\approx 10\%$ sintered porosity)	0.070 ± 0.002	0.068 ± 0.004
iii) MIM-processed parts	binder-based ($5\sim 6\%$ sintered porosity)	0.047 ± 0.003	0.053 ± 0.004

4.2.2 Analyses of particle characteristics of TiC_x

OM

Figure 26 shows the optical micrographs of all MIM β Ti-alloys involved in the TiC_x redistribution sintering cycle investigation in as-sintered and as-CSRAed state.

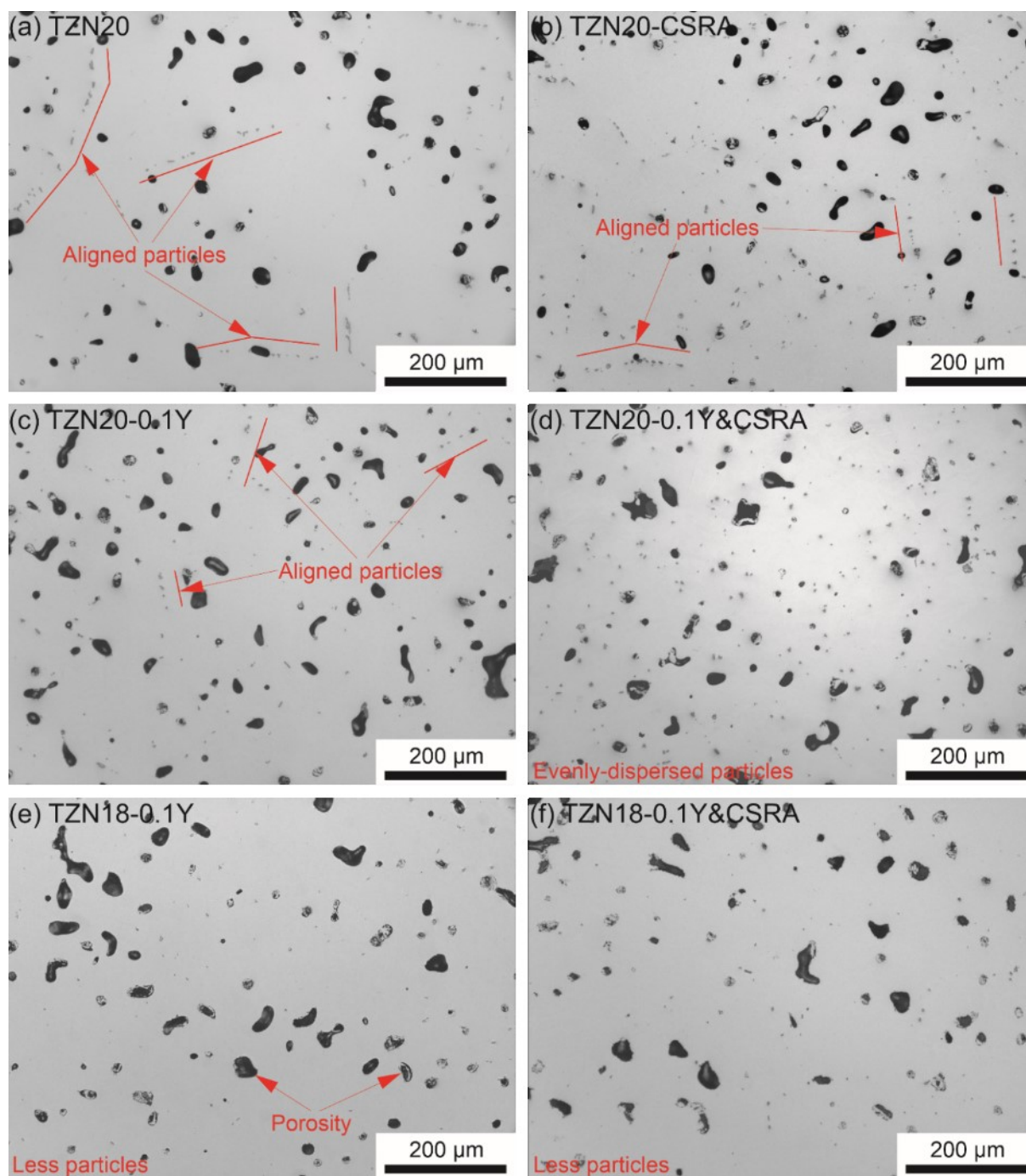


Figure 26 - Optical micrographs of metastable β Ti-MIM-TZN alloys with different particle distributional patterns. Like most PM β Ti-alloys, (a) conventional-sintered TZN20 alloys also have an aligned distribution pattern of platelet-shaped particles with rather large size; (b) and (c) images show a basically aligned particles distribution mode in TZN20&CSRA and TZN20-0.1Y; (d) to (f) TZN20-0.1Y&CSRA and TZN18-0.1Y(&CSRA) alloys exhibit an uniformly dispersed mode [107].

Platelet-shaped particles with rather large size are distributed in an aligned mode in conventional-sintered TZN20 (see **Figure 26** (a)). This distributional feature is practically the same as in many previous reports [19, 20, 99, 110, 146, 150, 194]. By contrast, the particles in TZN20&CSRA and TZN20-0.1Y indicate a neutral distribution mode; a few aligned particles were visible in some cases, but not as many as in TZN20, as marked by arrows in **Figure 26** (b) and (c). Whereas, it can be observed that rather tiny dispersoids are evenly-dispersed throughout TZN20-0.1Y&CSRA (**Figure 26** (d)). The uniform particle distribution of TZN18-0.1Y(&CSRA) alloys is basically the same as in TZN20-0.1Y&CSRA, but the number of particles is obviously lower (**Figure 26** (e) and (f)). Because the particle distribution of TZN18 series is not significantly affected by CSRA, they were specifically designed and introduced into this study as a reference group for discussion in Section 5.2.3. Besides, there was a slightly higher porosity in the alloys with Y addition, which may be due to the fact that large Y and yttria powder particles degrade sinterability [109], which has been elaborated in Section 4.1.2.

EDS preliminarily chemical analysis

As described above, the particle distributions in TZN20 (conventional sintering cycle) and TZN20-0.1Y&CSRA (TiC_x redistribution sintering cycle) were extremely different, specifically aligned-agglomerated and evenly-dispersed patterns, respectively. In this report, we confine the preliminary characterization of the particles on their stoichiometry and morphology, reporting first about stoichiometry in this section. Investigations of the crystalline configuration of TiC_x have been extensively performed by other authors in the past decades [71, 110, 141, 144, 146, 179, 195, 196].

The average values \pm variance of the chemical compositions of these aligned and dispersed particles determined for 10 sites of each type (i.e. TZN20 and TZN20-0.1Y&CSRA) are summarized in **Table 16**. Taking the variances into account, the minor differences between aligned and dispersed particles can be neglected. Therefore, the particles were assumed to be of the same chemistry and thus probably also same structure.

Table 16 - EDS quasi-quantitative chemical analyses of TiC_x with different particle distributional patterns determined for 10 spots [107].

Distributional pattern	Samples	C/ at.%	O/ at.%	Ti/ at.%	Nb/ at.%	Zr/ at.%
Aligned TiC_x	TZN20	15.7 ± 0.9	6.4 ± 0.7	68.3 ± 0.9	1.7 ± 0.6	7.9 ± 0.8
Dispersed TiC_x	TZN20 -0.1Y&CSRA	16.8 ± 1.5	5.3 ± 1.2	66.7 ± 2.2	2.0 ± 0.8	9.2 ± 1.5

A simple reasonability check for the results is deduced in the following. A value for the carbon concentration in present TiC_x was estimated on the basis of the densities ($\rho_{\text{TZN20}}=4.95 \text{ g/cm}^3$, $\rho_{\text{TiC}}=4.93 \text{ g/cm}^3$), and we assumed as a premise that all carbon atoms in the particles were bound in TiC_x form (0.05 wt.% C formed 0.5 vol.% TiC_x), i.e. no carbon was dissolved in Ti-matrix. An upper limit of carbon concentration of TiC_x of 32 at.% (i.e. $x < 0.48$ in TiC_x) was calculated. Apparently not all carbon atoms are contained within precipitates, accordingly the concentration is supposed to be lower than 32 at.%. The measured values of approximately 16 at.% are thus in a reasonable range, i.e. about half of the carbon atoms are dissolved in the Ti-matrix. It means that a carbon solubility limit of ≈ 0.025 wt.% is estimated in TZN20 series. This limit was thought also to be in fairly good agreement with the predicted maximum carbon limit of 0.023 wt.% in Ti-16Nb [141], which may be more or less similar with TZN20 (Ti-10Zr-20Nb), due to Zr increasing carbon solubility [110] but a higher Nb content acting in the opposite direction. In addition, a similar initial precipitation temperature ($\approx 900^\circ\text{C}$ in β phase region) of TiC_x in Ti-16Nb implies essentially the same lattice constant which might determine the solubility limit of interstitial carbon atom [110].

Furthermore, SEM-BSE and EDS maps of areas surrounding the particles in two different distributions, i.e. aligned mode in TZN20 and dispersed mode in TZN20-0.1Y&CSRA, are displayed in **Figure 27** and **Figure 28** respectively; the weight percentages of elements incl. carbon, titanium, niobium and zirconium were expressed by color intensity.

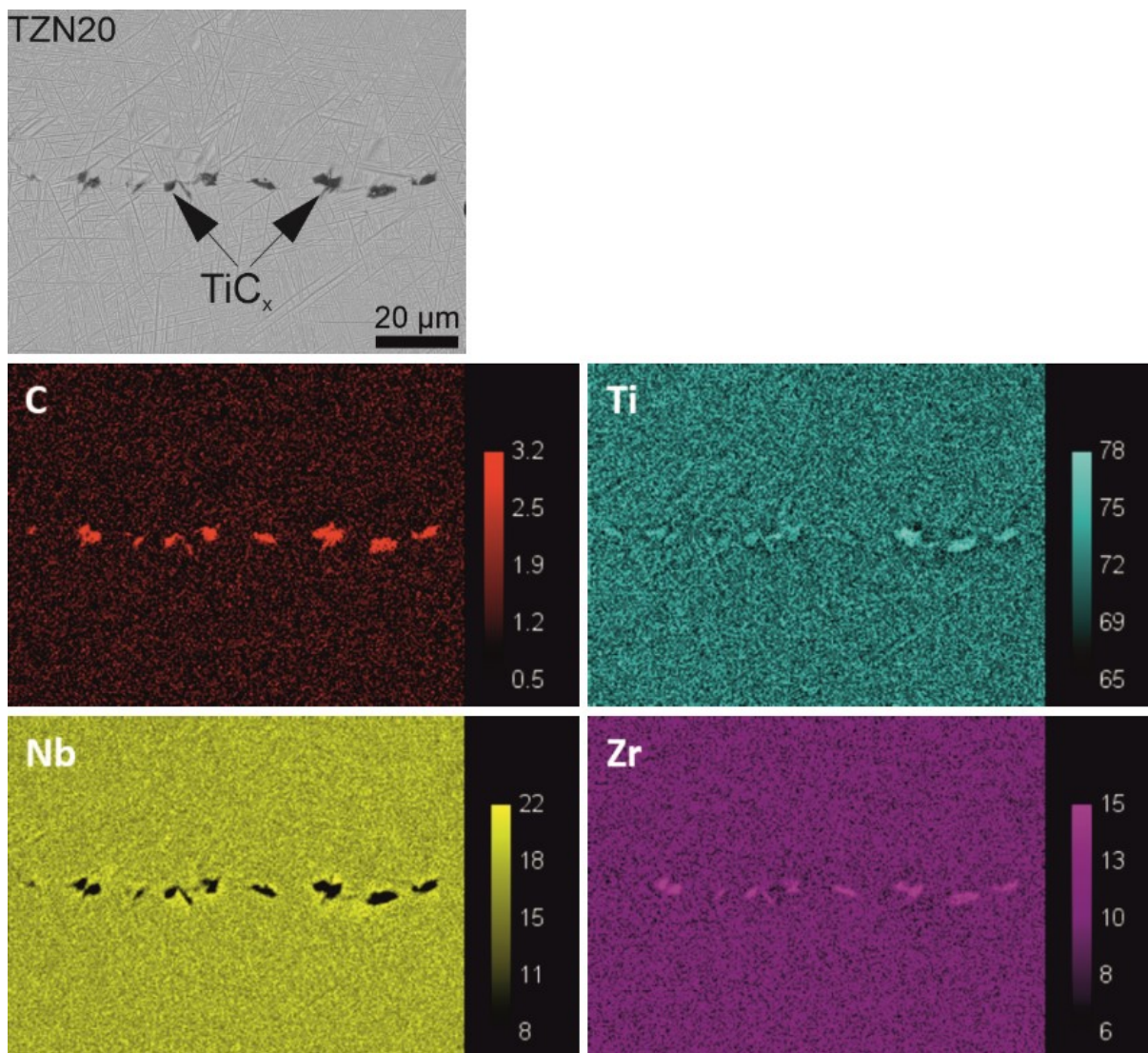


Figure 27 - SEM-BSE images and chemical element mappings of an area of TZN20 with aligned particles [107].

Interestingly, TiC_x contained strikingly more Zr and less Nb than the Ti-matrix. A possible explanation is given here; Zr atoms expand the β Ti-lattice [110], while Nb decreases it [194]. Furthermore, the lattice space of fcc- TiC_x supercells enlarges with increasing number of carbon atoms [197]. It is reasonable to suppose that the TiC_x superlattice tends to capture Zr atoms that are diffusing near TiC_x to substitute Ti atoms (or likely Nb) in order to achieve a localized lowest lattice deformation energy. This substitution associated with the fact that Zr also is a strong carbide former in some cases are responsible for the observed hybrid TiC_x ($Ti_aZr_bC_xO_c$).

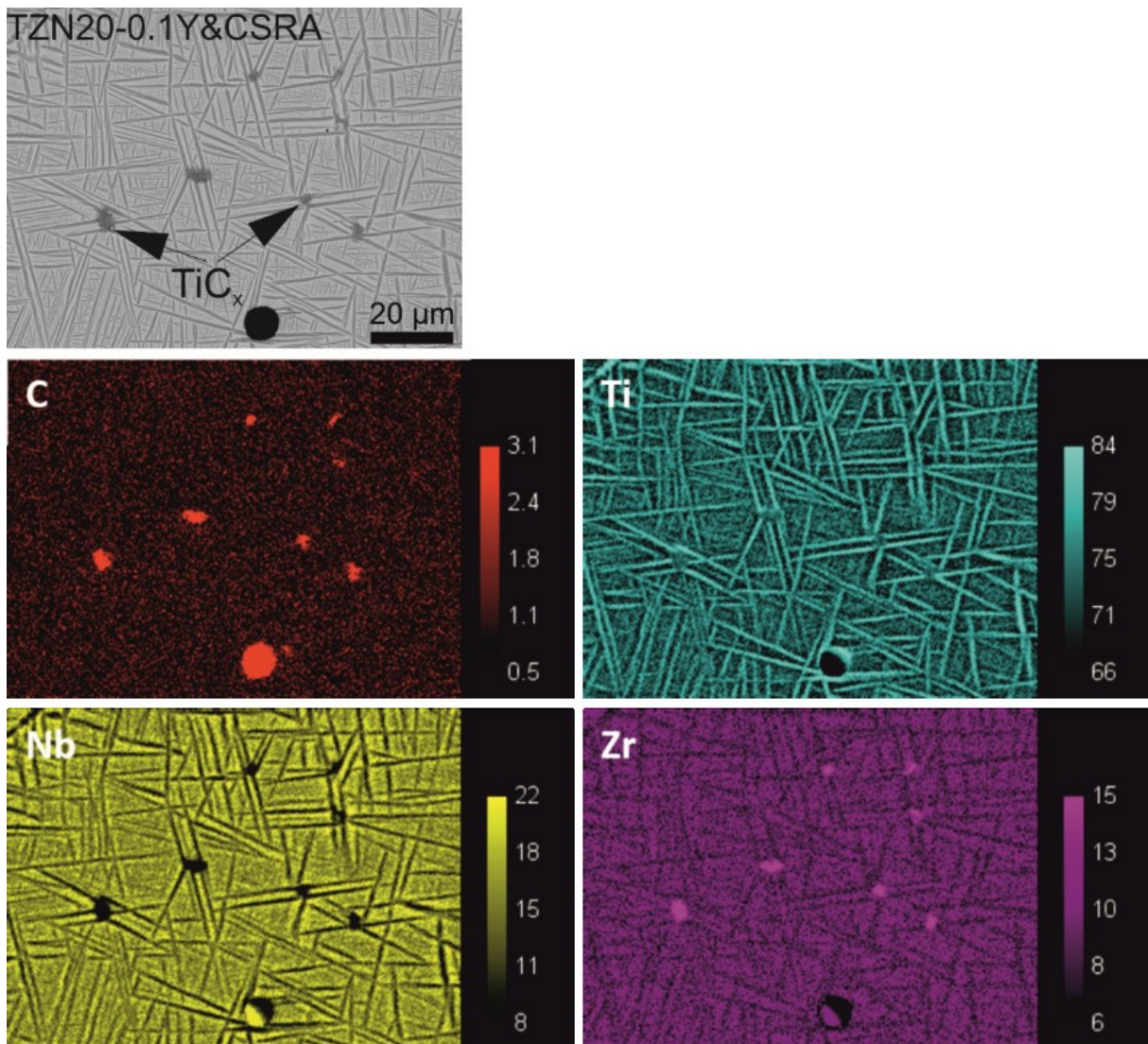


Figure 28 - SEM-BSE images and chemical element mappings of an area of TZN20-0.1Y&CSRA with dispersed particles [107].

EBSD

The TiC_x precipitation location is either at the grain boundaries or inside prior β grains, i.e. either GB- TiC_x or intragranular TiC_x second phases, can be identified from EBSD (**Figure 29**). The left side of each image shows β phase for indicating β grain boundaries; the right side shows the titanium carbide (TiC_x) phase.

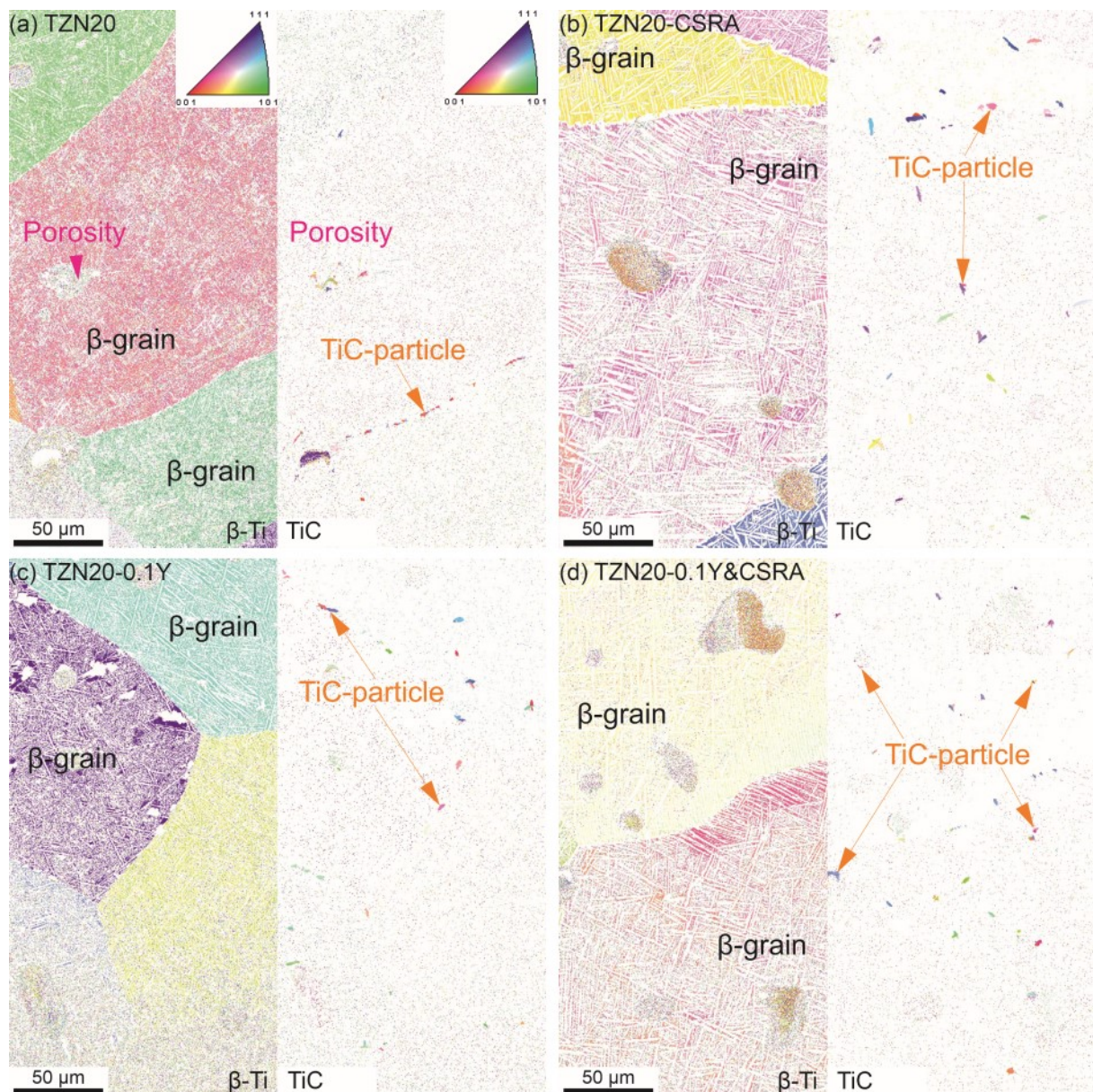


Figure 29 - Inverse pole figure (IPF) maps of β -Ti phase (left) and TiC_x phase (right) in (a) TZN20; (b) TZN20-CSRA; (c) TZN20-0.1Y; (d) TZN20-0.1Y&CSRA, in order to identify the precipitation location of TiC_x phases, i.e. either GB- TiC_x or intragranular TiC_x [107].

In the conventional sintered TZN20, the majority of TiC_x particles distributed rigorously in alignment along β grain boundaries, which are GB- TiC_x , as displayed in **Figure 29** (a); this is the aligned-agglomerated distribution pattern and widely recognized for TiC_x particles in powder metallurgically sintered β Ti-alloys. **Figures 34** (b) and (c) seem to represent a sort of transition, specifically almost half of the TiC_x particles are found inside the β grains, the rest is located at grain boundaries. However, the inspection of **Figure 29** (d), for TZN20-0.1Y&CSRA produced by TiC_x redistribution sintering cycle, indicates that a substantial

amount of TiC_x dispersoids is embedded in the interior of grains (intragranular TiC_x) in a rather uniform mode; only few particles were found at the grain boundaries. It is therefore conceivable that TiC_x existing mainly in the form of GB- TiC_x led to the aligned particle distributional pattern, whereas the situation in the form of intragranular TiC_x exhibited the dispersed particle distributional pattern. In brief, the precipitation sites of TiC_x phase might determine the final TiC_x particles distribution pattern. This observation combined with **Figure 28** with higher magnification (than **Figure 29**) suggests that the intragranular TiC_x particles tend to precipitate at the bundles of coarse laths of secondary α -phase or their intersections rather than randomly. More detailed discussion associated with synchrotron results is done in Section 5.2.1.

Geometrical morphology of TiC_x phases

The essential particle characteristics are summarized in **Table 17**.

Table 17 - Particle characteristics of TiC_x in the MIM-TZN alloys (determined by using Image J analysis software for approximately sampling 200 TiC_x particles in each alloy) [107].

Samples	Mean aspect ratio/ unitless	Mean particle size/ μm
TZN20	2.55	6.6
TZN20-CSRA	1.95	6.5
TZN20-0.1Y	2.28	5.8
TZN20-0.1Y&CSRA	1.72	5.4
TZN18-0.1Y	1.85	4.3
TZN18-0.1Y&CSRA	1.91	4.6

To start with the mean aspect ratio of TiC_x particles, it significantly drops after CSRA and is moderately decreased by Y addition in TZN20 series. On the other hand, the impact of CSRA on average particle size is negligible, but it can be fairly lowered by Y addition. On the whole, the maximum values of aspect ratio and particle size were found for aligned TiC_x particles (see TZN20), by contrast, the minimum was exhibited by dispersed TiC_x particles (see TZN20-0.1Y&CSRA). This is in agreement with the optical impressions (see **Figure 26**).

However, for TZN18 series (reference group) the volume fractions in **Table 14** are almost half the value of the TZN20 series. This lower total amount of TiC_x is possibly difficult to promote the formation of large particles. By comparing TZN18 series before and after CSRA, we found

a slight difference in aspect ratio, which is considered as a possible measurement error originated from the technical limitation, due to that the particle characteristics in the series are too similar to distinguish by merely sampling 200 particles.

4.2.3 Mechanical properties

The tensile properties associated with the two kinds of particle distribution patterns are illustrated in **Figure 30** and the detailed tensile and microstructural properties with average and experimental errors are specified in **Table 18**. The MIM-parts with fully and partially aligned TiC_x particles basically showed relatively low elongation to fracture (ϵ_f) (see the left side of **Figure 30**), whereas the materials with dispersed TiC_x particles provided values for ϵ_f as high as 8% (right side). Furthermore, elongation in TZN20 series was significantly improved after CSRA, but not much by only Y addition. A striking enhancement of $\approx 113\%$ in elongation was attained from conventional-sintered TZN20 to particle-redistributed TZN20-0.1Y&CSRA produced by the novel-designed TiC_x redistribution sintering cycle. However, ϵ_f in TZN18 series (reference group) did not exhibit an apparent increase owing to CSRA. It was because the TiC_x particle distributional pattern was already dispersed before CSRA and no obvious change in distribution was found after CSRA.

Yield strength (YS) declined marginally by CSRA in all conditions likely owing to the combination of slight stress relieving and microstructure change, while it was virtually unchanged by Y addition. Moreover, comparing TZN20-0.1Y and TZN18-0.1Y suggests a moderate decline in YS, around 70 MPa. This decrease in strength was basically caused by degraded the strengthening effects of Nb by deforming the Ti-based lattice. Additionally, the effect of TiC_x particle reinforcement partially shifting to solid solution strengthening by dissolved carbon interstitials (6.9 MPa/0.01 wt.% in Ti [198]) on YS remains unclear.

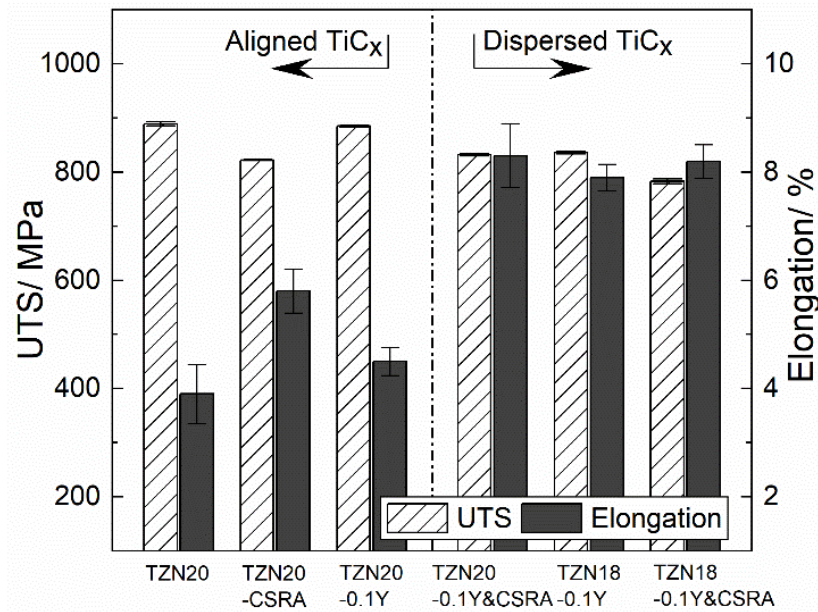


Figure 30 - Ultimate tensile strength (σ_{UTS}) and elongation to fracture (ϵ_f) of MIM-TZN alloys with different TiC_x particle distributional patterns. Fully and partially aligned TiC_x particles on the left side and dispersed TiC_x particles on the right side [107].

Table 18 - Tensile and microstructural properties of MIM-TZN alloys at room temperature [107].

Samples	σ_{YS} / MPa	σ_{UTS} / MPa	Elongation (ϵ_f) / %	E-Modulus / GPa	Grain size / μm	Porosity / %
TZN20	768 ± 3.9	889 ± 3.9	3.9 ± 0.5	70.9 ± 2.9	373 ± 12	5.0
TZN20-CSRA	704 ± 1.6	822 ± 1.0	5.8 ± 0.4	75.3 ± 3.3	384 ± 16	5.0
TZN20-0.1Y	779 ± 0.9	885 ± 1.2	4.5 ± 0.3	68.5 ± 2.4	301 ± 19	6.0
TZN20-0.1Y&CSRA	742 ± 4.1	832 ± 2.1	8.3 ± 0.6	65.7 ± 4.6	317 ± 15	6.0
TZN18-0.1Y	708 ± 3.3	836 ± 2.2	7.9 ± 0.2	78.4 ± 1.2	325 ± 5	5.5
TZN18-0.1Y&CSRA	681 ± 4.6	783 ± 4.8	8.2 ± 0.3	76.9 ± 5.7	340 ± 21	5.5

In addition, Young's moduli of the present MIM-TZN alloys (**Table 18**) were far below the majority of specified Ti-alloys [3, 11]. Their β -stabilizer Nb contents are close to the first valley value (the minor Nb content) of Young's modulus in Ti-Nb system [199]. Interestingly, the "neutral element" Zr and " α -stabilizing element" O are by some authors considered to stabilize β -phase when they are added in β Ti-alloys [17, 35]. Zr and O are also able to suppress the ω phase and martensitic transformation effecting low Young's modulus [17, 200]. Low moduli can weaken the stress shielding effect in orthopedic applications.

The true stress-strain curves of MIM-processed TZN β Ti-alloys converted from the engineering stress-strain curves are given in **Figure 31**, which reflect a fairly low work hardenability of the Ti-biomaterials.

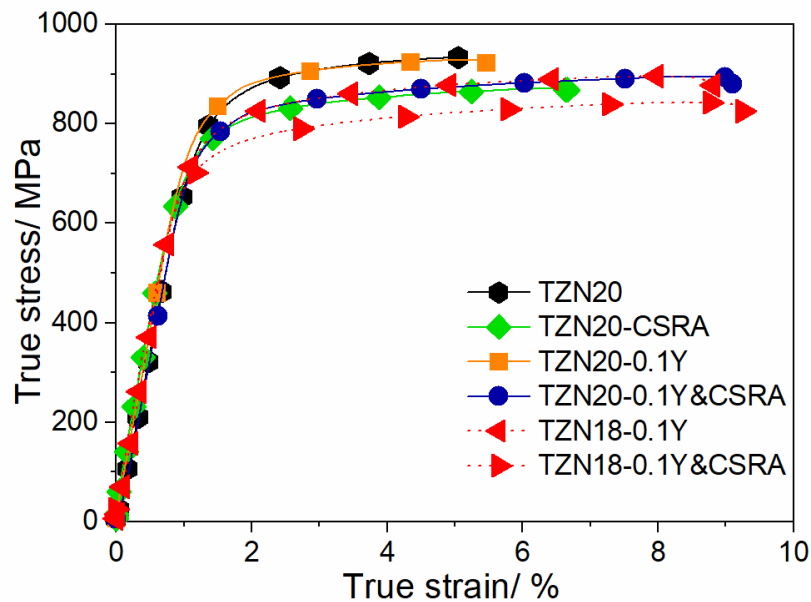


Figure 31 - True stress-strain curves of MIM-TZN alloys (5~6% porosity) at room temperature show low hardening rates [107].

4.2.4 Fractography

Fracture profiles of specimens with different particles distributions

In order to reveal the influence of particle distributional patterns of TiC_x on toughness to strain of MIM-TZN alloys, tensile fracture profiles (**Figure 32**) of TZN20 (aligned particles) and of TZN20-0.1Y&CSRA (dispersed particles) were examined.

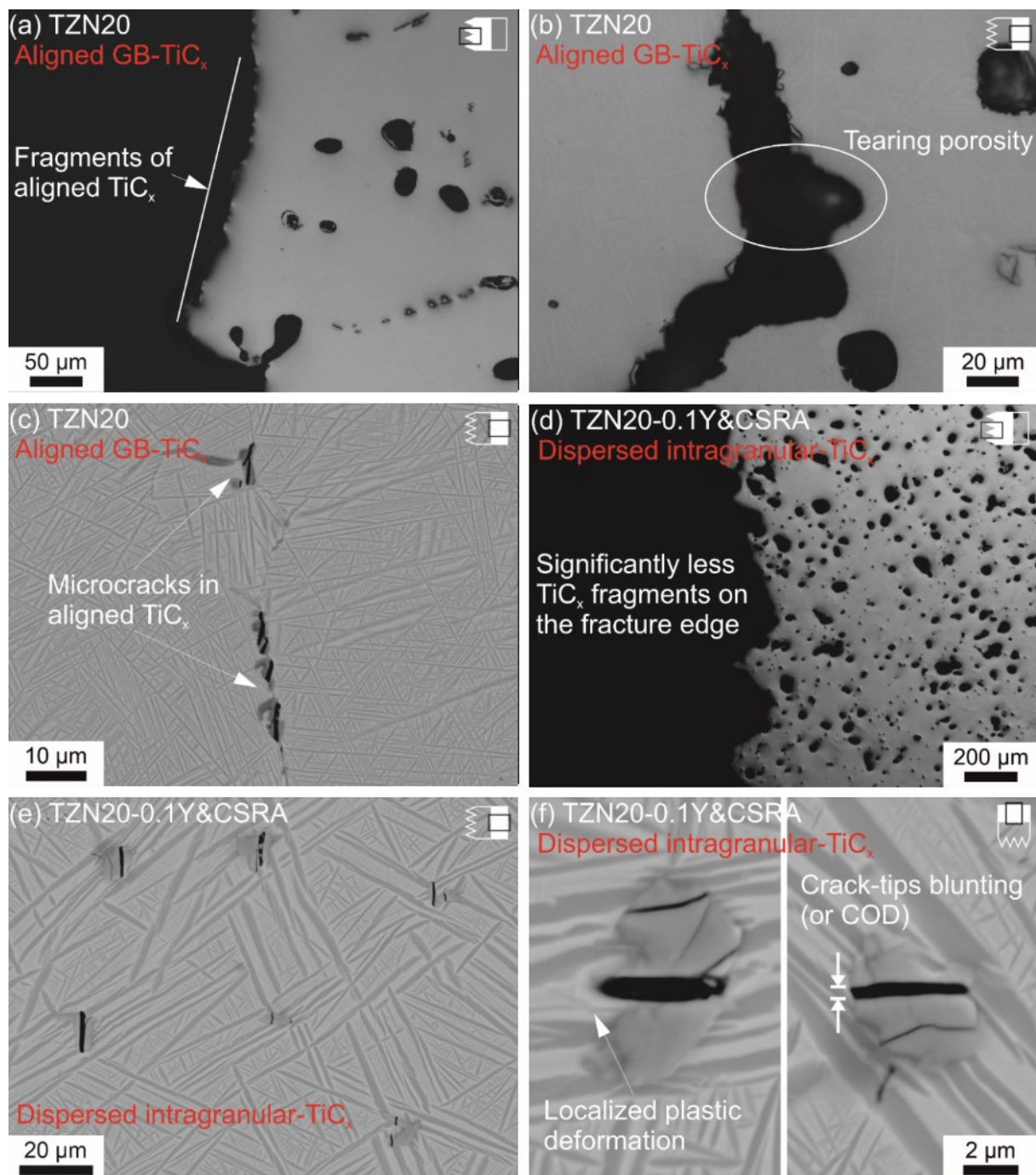


Figure 32 - OM/SEM-BSE fractographic profiles of TZN20 with aligned GB-TiC_x and TZN20-0.1Y&CSRA with dispersed intragranular TiC_x: (a) the fragments of TiC_x are in alignment; (b) a typical internal macroscopic crack; (c) aligned microcracks (TiC_x) are close together; (d) less TiC_x fragments on the winding fracture edge and uniformly distributed TiC_x particles in the interior; (e) microcracks in dispersed TiC_x particles; (f) crack-tips blunting or crack opening displacement (COD) and localized plastic deformation [107].

In the aligned case in TZN20, particle-fragments were in near-alignment with the fracture edge (see **Figure 32** (a)). This suggests that these fragments were consistently aligned-agglomerated TiC_x particles distributed along prior β grain boundaries. Moreover, a few torn large-sized cracks were found generally near the fracture edge; a typical interior macro-crack is visible in **Figure 32** (b). It can be inferred that several cracks were growing concurrently, even so, the majority of cracks remained below the critical crack size. Additionally, porosity is believed to likely facilitate these cracks, because smooth cambered surfaces or arcs can be repeatedly seen at the fracture edge. From **Figure 32** (c) it can be deduced that aligned TiC_x particles were frequently ruptured; the upper arrow marks a position where two cracks linked together and the lower arrow indicates other relatively large cracks quite close. The crack growth path in TZN20-0.1Y&CSRA is very winding (see **Figure 32** (d)). Neither macrocracks similar to **Figure 32** (b) nor connected microcracks as marked by arrow in **Figure 32** (c) were discovered in the interior of TZN20-0.1Y&CSRA with dispersed TiC_x (as shown in **Figure 32** (d)). This implies that very few microcracks grew during plastic deformation. Nonetheless, there is a large amount of fractured TiC_x particles, which are randomly embedded in the Ti-matrix (see **Figure 32** (e)). The magnified images of typical fractured TiC_x particles are shown in **Figure 32** (f); obvious localized plastic deformation and crack-tip blunting, i.e. large crack opening displacement (COD), are visible. Also, multiple cracked TiC_x particles can be found.

On the whole, no pulled-out intact TiC_x particles were discovered. Nor has decohesion at the particle-matrix interfaces been observed. The appearance of only internal fracture suggests that the cohesion between TiC_x particles and Ti matrix was sufficiently strong. Cracking occurred virtually perpendicular to the tensile-load direction.

Fractography of specimens with different particles distributions

The fractographic images support the idea that the present MIM-TZN alloys can be classified into two different fracture modes corresponding to their different particle distribution patterns, as illustrated by **Figure 33**.

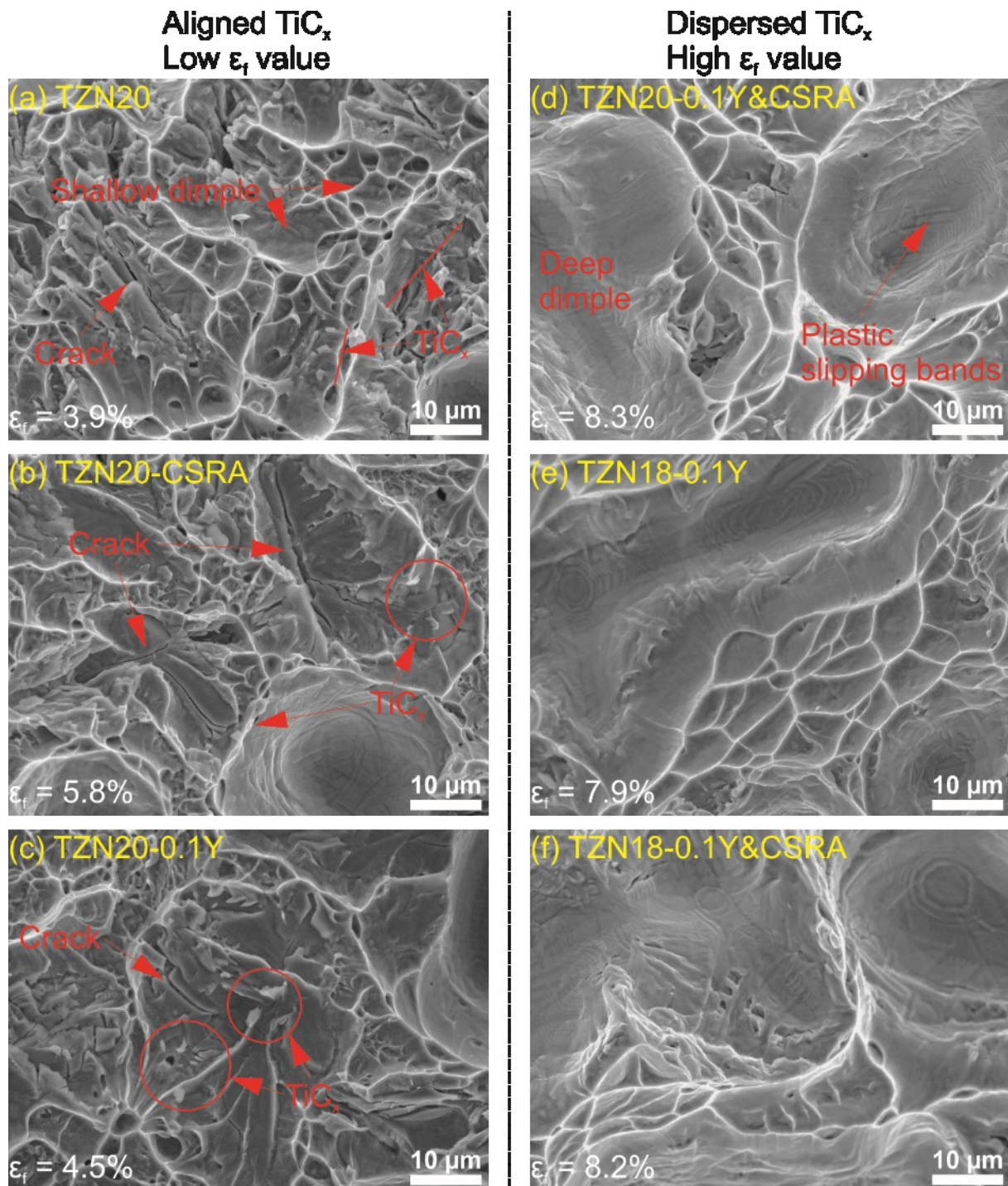


Figure 33 - SEM-SE images, indicating the implication of TiC_x particles in fractographs of MIM-TZN alloys. A lot of TiC_x particles or their fragments, large cracks and quasi-cleavage facets were observed in aligned TiC_x cases: (a) TZN20; (b) TZN20-CSRA; (c) TZN20-0.1Y. Few TiC_x particles and deeper dimples with plastic deformation slipping bands were found in dispersed TiC_x cases: (d) TZN20-0.1Y&CSRA; the reference group (e) TZN18-0.1Y and (f) TZN18-0.1Y&CSRA [107].

It was observed in cases of aligned carbides that numerous platelet-shaped TiC_x particles (fragments) and visible cracks with a particularly large size occurred on the fracture surface, as denoted by arrows in **Figure 33** (a) to (c). These visible cracks were likely the branches of major cracks running below the surface. In general, the fractography in case of aligned particles showed quasi-cleavage planes characterizing a relatively brittle fracture mode, occasionally decorated with several rather shallow dimples. By contrast, MIM-TZN alloys with dispersed TiC_x particles demonstrated a basically ductile fracture mode ($\epsilon_f \approx 8\%$) with a large number of deep dimples, where plastic slipping bands are visible, as shown in **Figure 33** (d) to (f). TiC_x fragments were seldom seen in these cases. Fairly small-sized cracks or microvoids can be found in some occasions. All in all, the fracture surface of the aligned particles case exhibits excessive TiC_x fragments and cracking branches, whereas the dispersed manifests only few fragments but deep dimples.

4.2.5 Precipitation evolution of TiC particles

The percentages of TiC_x precipitation of TNZ20 and TNZ20-0.1Y in relation to the temperature during cooling determined by *in situ* high energy X-ray diffraction are plotted in **Figure 34**. The starting temperature of TiC_x precipitation in the case of the 0.1wt.% Y containing alloy was much lower than for TZN20. Importantly, TiC_x evolution in TZN20 demonstrated a three-step process: a strong precipitation-type reaction at higher temperatures, afterwards a moderate dissolution-type reaction between about 770 to 670 °C and a re-precipitation reaction at lower temperatures. This moderate dissolution-type reaction corroborates that the high-temperature α phase has a higher solubility of carbon, which is in general agreement with the Ti-C phase diagrams reported in the literature [141, 201]. Corresponding to the phase diagram, the HEXRD results reveal two non-adjacent TiC_x precipitation-type reactions occurring in the high temperature β phase region (Region I) and in the low temperature $\alpha + \beta$ region (Region III). These regions sandwich a dissolution-type region (Region II) just below α/β transus. At sufficiently low cooling rate (2K/min) in the CSRA step or during the synchrotron experiment, there is more time available for the dissolution-type reaction in Region II (≈ 156 mins in CSRA, ≈ 73 mins in synchrotron experiment) compared to the conventional sintering cycle (≈ 15 mins) enabling a sufficient dissolution of the carbides formed in Region I. Thus, to some extent, TiC_x was dissolved into the Ti matrix and subsequently reprecipitated at low temperature in Region III. By contrast, the amount of precipitating TiC_x in TZN20-0.1Y increased monotonously and at much lower temperature than the starting precipitating temperature of TiC_x in TZN20.

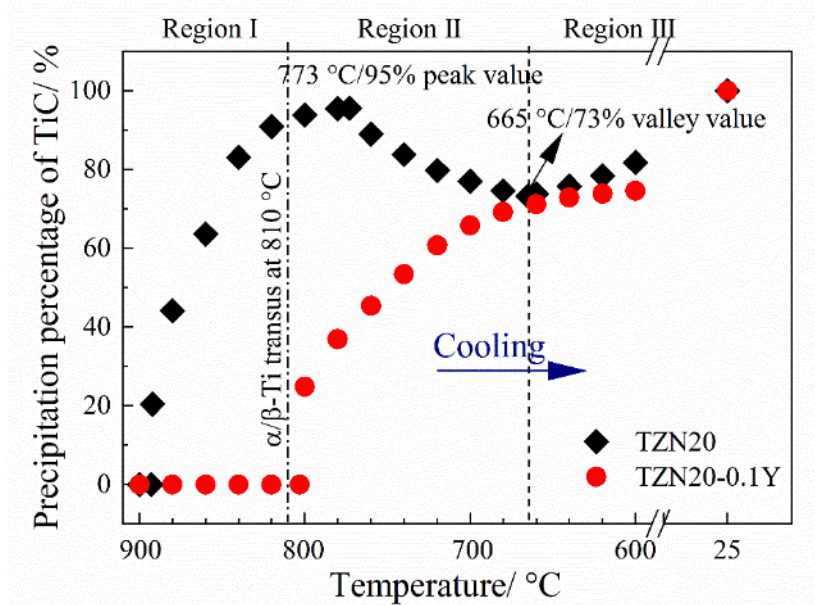


Figure 34 - The curves of precipitation percentage (the ratio of the volume fraction at a given temperature to the volume fraction at room temperature.) of TiC_x in relation to the temperature during cooling in TZN20(-0.1Y) alloys measured by HEXRD [107].

5. Discussion

5.1 Rationality of using Y-containing sintering in PM/MIM β Ti-alloys

The influence brought from the RE-series sintering cycle, e.g. Y-containing method herein, on the tensile properties of PM β Ti-alloys, e.g. MIM Ti-10Zr-20Nb, is quite complicated. The commercially available Y elemental powders normally are rather large-sized (e.g. 325 mesh or $D_{90} = 45 \mu\text{m}$), and irregular-shaped powder particles. Hence, Y addition generally introduces some factors, consisted of yttria (Y_2O_3) particles, grain refinement effect, microstructural adjustment of Ti-matrix (e.g. the morphology of GB α phase (α_{GB}) and/or secondary α phase (α_s)), oxygen-scavenging effect, increased residual porosity and more interconnected pores, no matter how much quantity of Y is added. As a result, the strengthening mechanisms, deformation modes, and fracture mechanics of PM β Ti-alloys produced by the Y-containing methods have changed to some extent. However, to achieve sufficient damage tolerance by Y addition, it makes sense to optimize the Y-containing (sintering cycle) in a strategic and tailored way.

5.1.1 Mechanisms influencing tensile properties

In terms of tensile properties of materials, a more detailed analysis is conducted in the following in order to explore whether it is possible to further optimize the Y-containing method.

Tensile strength

As already mentioned, the present MIM-processed TZN20-xY alloys have nearly the same oxygen equivalent O_{eq} of around 0.455 wt.% (see **Figure 19**). Also, the particle strengthening effect at ambient temperature provided by moderate-sized RE oxides has been found to be fairly limited [164]. The geometric morphology of α_{GB} and α_s did not change significantly. Therefore, only parameters that show significant changes such as solid solution oxygen equivalent ($O_{\text{sseq.}}$), relative density and prior β grains diameter are taken into consideration. The effects of these features were attempted to be separated and plotted into **Figure 35** based on known relationships (from the literature [102, 127, 128, 169]) between them, i.e. ultimate tensile strength (UTS) vs. solid solution oxygen equivalent ($O_{\text{sseq.}}$) in **Figure 35** (a); vs. relative density (or residual porosity) in **Figure 35** (b); and vs. mean β grain size in **Figure 35** (c). Apart from that, the reference materials shown in the same figure are selected from Refs. [102,

127, 169] for MIM Ti-6Al-4V, which is marked by the red color, and Ref. [128] for MIM Ti-6Al-7Nb, which is marked by the blue color, fabricated by exactly the same production line via the pre-alloyed powder method.

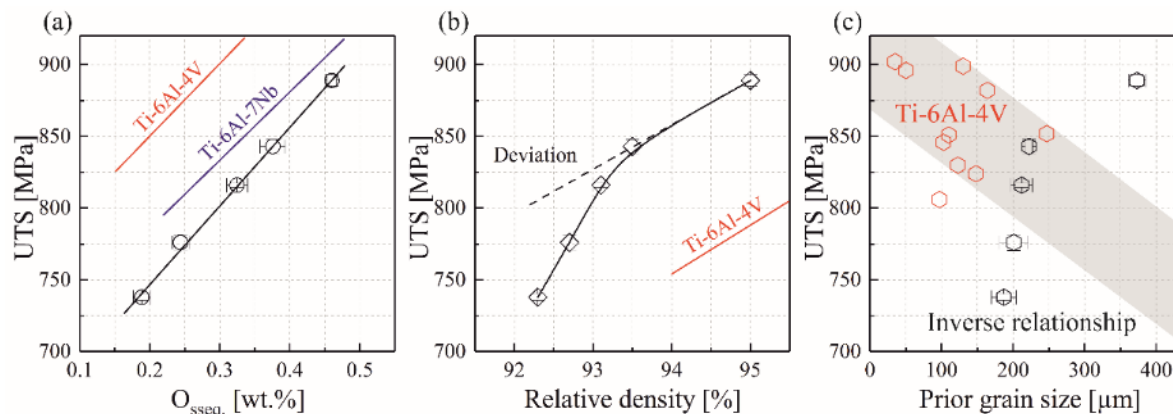


Figure 35 - The relationships of ultimate tensile strength (UTS) and its possible impact factors that exhibit marked changes: (a) vs. solid solution oxygen equivalent ($O_{sseq.}$); (b) vs. relative density (or residual porosity); and (c) vs. mean β grain size. The reference materials are obtained from MIM Ti-6Al-4V and MIM Ti-6Al-7Nb [191].

There is a definite linear relationship between ultimate tensile strength (UTS) and solid solution oxygen equivalents ($O_{sseq.}$) as revealed in **Figure 35** (a). Such results are consistent with the literature [127, 128]. In those studies, linear relationships between the solid solution oxygen equivalent and tensile strength are detected, but no obvious oxide particles are found. Furthermore, it has been widely accepted that the decrease in relative density (or increase in residual porosity) weakens tensile strength [56]. Inspection of **Figure 35** (b) indicates that the strength-reducing effect (i.e. the slope of the curve in the range of 93.5% – 95% relative density) is in good agreement with the trend in MIM Ti-6Al-4V [127], as shown by the red line. However, with a higher porosity from 92.5% to 93.5%, there is an accelerating trend for UTS to decrease, deviating from the original linear relationship. This behavior is likely caused by excessive irregular or interconnected porosity that is more detrimental and reduces tensile strength to a greater extent. Interestingly, the beneficial effect of grain refinement on strength is not evident or even opposite (see **Figure 35** (c)). Note that this merely could imply that strengthening by grain refinement due to Y additions is overcompensated by the effects of residual porosity and solid solution oxygen equivalent. Therefore, a behavior according to the classic Hall–Petch relationship was not detected [202, 203]. The previous studies, where

MIMed Ti-6Al-4V with similar porosities (2.3%~3.6%) and oxygen contents (0.19~0.23 wt.%) was fabricated, as shown by red hexagons in **Figure 35** (c) [102, 127, 169], weakly reflect the trend based on the Hall–Petch relationship, but on a fairly wide scatter band. To some extent, this is in general agreement with the present study, i.e. the effect is not clearly evident. Simply speaking, it is reasonable to deduce that even if the prior β grains are refined to only half of their original average grain diameter Hall-Petch strengthening is negligible in the range of grain sizes investigated here (e.g. 180 μm ~ 380 μm) if compared to effects of solid solution oxygen equivalent or residual porosity.

Tensile ductility

Among the aforementioned three main factors changing significantly by adding Y elemental powder, in general only the refined β grains and the decreased oxygen levels in Ti-matrix are beneficial to the ductility of Ti-alloys. Whereas, the increased porosity deteriorates sharply the elongation to fracture of PM Ti alloys. The deterioration effect is so strong that when merely 0.5 wt.% Y powder is added and the porosity consequently increases by around 2%, this deteriorating effect has already completely counteracted the positive effects provided by oxygen-scavenging and refinement of prior β grains. The appearance of stiff particles, such as stiff yttria (Y_2O_3) particles in this study, is normally believed to lead to extra microcracks due to stress concentration, thereby worsening the ductility. However, no crack initiation, neither inside these particles nor on the particle-matrix interface, led by loading strain was found in MIM-processed TZN20-xY alloys.

The effects of the Y-containing method in the present MIM β Ti-alloys on the tensile properties of TZN20-xY alloys are systematically summarized below. First, by using the Y-containing method, owing to the high affinity between RE Y and oxygen atoms, Y is able to scavenge oxygen atoms from the Ti-matrix to form yttria particles, thus achieving a reduction in the solid solution oxygen equivalent O_{seq} in β Ti-alloys. However, yttria to date has not proven to increase the tensile strength of Ti alloys but instead, promotes fracture failure induced by strain loading. Therefore, from the perspectives of oxygen-scavenging, the usage of Y-containing method can improve the ductility and toughness of PM β Ti-alloy. However, with the decrease of the solid solution amount of oxygen in the Ti-matrix, the interstitial strengthening effect provided by oxygen atoms is reduced and the tensile strength of β Ti-alloy is lowered.

Furthermore, by using elemental Y powders with a rather large particle size, as yttria degrades sinterability, the residual porosity was significantly increased. What is more, very detrimental interconnected pores and many pore-yttria particles arose. These pore-yttria particles as well as increasing porosity, mainly contributed to the grain refinement effect through inhibiting β grain growth. The contribution to grain refinement from the interior-yttrias working as extra nucleation sites is unconfirmed yet and is currently only assumed. Nevertheless, no matter what mechanism causes the grain refinement, the effect offered by Y-containing method is definitely limited in practice and much weaker than that of boron sintering cycle. E.g. with the addition of 0.5 wt.% in both cases, boron sintering cycle is capable of refining by one order of magnitude (from $\approx 150 \mu\text{m}$ to $\approx 15 \mu\text{m}$ [115]), while that from Y-containing method is less than half (specifically from $373 \mu\text{m}$ to $212 \mu\text{m}$) even if the initial grain diameter is much larger. This is basically consistent with the previous studies regarding MIM Ti-6Al-4V alloys [80, 81]. As the effect of Y on grain refinement is insufficient, thus the limited improvement of strength and ductility due to this can be ignored. On the contrary, increased porosity significantly deteriorates the tensile properties of PM Ti alloys and should be avoided as much as possible. Based on an acceptable porosity is critical, the ineffective β -grains refining effect provided by Y addition is supposed to be abandoned.

5.1.2 Optimized Y-containing method and its significance for application

It is well known that the shrinkage and closure of pores during sintering is caused by element diffusion driven by the minimization of particle surface energy, as shown in **Figure 9**. Refractory elements such as Nb can increase porosity owing to their slow diffusion rates even at elevated temperatures [84, 99]. The reason for the decreased densities in the Y-added TZN20 samples, however, is different. It is generally accepted that Y atoms are extremely reactive with oxygen atoms. The effect of oxygen scavenging from the Ti-matrix accelerates dramatically in the range of $800 \text{ }^\circ\text{C}$ to $900 \text{ }^\circ\text{C}$ during heating of the Y-containing method. This effect ends at about $1025 \text{ }^\circ\text{C}$ as all elemental Y is consumed at that point [112]. Therefore, during sintering of the Y-added TZN20 at high temperature, Y powder particles should only exist in the form of yttria (Y_2O_3) particles. Unlike the Ti, Nb and Zr atoms, Y atoms do not practically participate in large-scale elemental diffusion (i.e. volume diffusion). Instead, based on the stable chemical structure of yttria (Cubic cI80 crystal structure [204]), the effect of Y on elemental diffusion may be negative, e.g. to obstruct the pore closing during sintering; a clear evidence is given later in **Figure 36** (c), indicating its effective shielding effect on materials diffusion.

To unveil the effect of particle size of yttria on residual porosity and prior β grain growth, the particle size distributions of interior-yttria and pore-yttria were investigated separately. The results are given in **Figure 36** (b). Before Y reacts with oxygen to form yttria (i.e. before the sintering cycle reaches about 800 °C ~ 900 °C), the solubility of Y in the Ti-matrix is very low with less than 0.02 wt.% [201]. Since early-formed yttria is rather stable during sintering, no yttria larger than the starting Y powder size (<45 μm) can be found. Therefore, it is reasonable to assume that Y powder hardly undergoes mass diffusion in the course of sintering, and the particle size of yttria in the as-sintered microstructure could represent the original Y powder particle size. From the results of the pore-yttria and interior-yttria, yttria particles of large size (e.g. $\approx 23 \mu\text{m}$) are more likely to cause porosity. Meanwhile, the interior-yttria particles are below 15 μm . These findings suggest that the usage of larger Y particles should be avoided; however, a size of below 15 μm may be acceptable with respect to residual porosity.

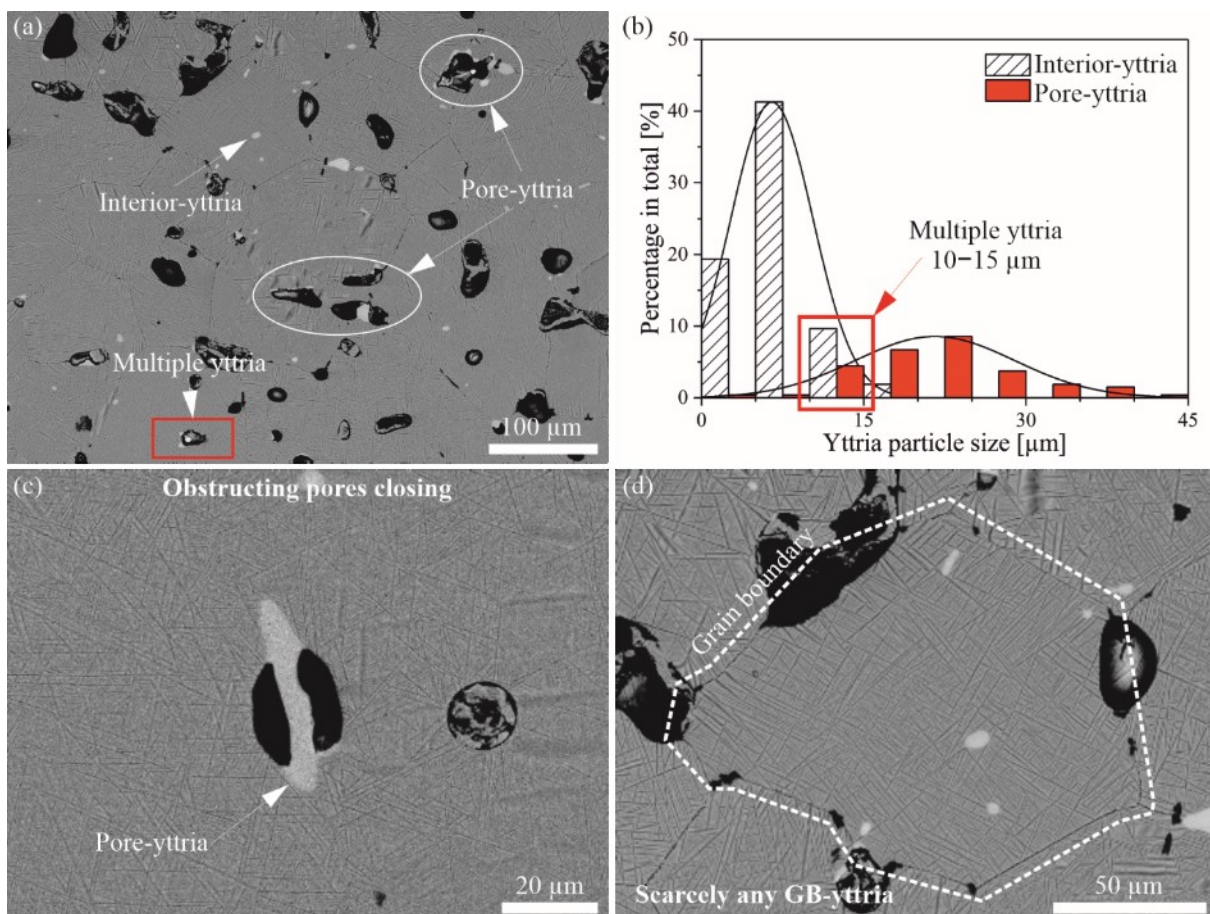


Figure 36 - SEM-images of two kinds of yttria and their particle size distribution. (a) Yttria distribution; (b) Particle size distributions of interior-yttria and pore-yttria, note that the small-sized pore-yttria, e.g. 10–15 μm , example marked by red rectangle in **Figure 36** (a), usually are compounds of multiple yttria

particles; (c) typical large yttria obstructs pore closing; and (d) Individual yttria away from porosity pinning at GBs is hardly discovered [191].

Based on the discussion of the effect of Y sintering cycle on tensile properties of MIM TZN20-xY alloys, an evaluation of the application significance on PM β Ti-alloys and a strategic optimization for RE-series sintering cycle are proposed here. On the whole, it can be concluded that the predominant function of RE-series sintering cycle is to scavenge the dissolved oxygen atoms from the Ti-matrix, thereby enhancing ductility and toughness through controlling oxygen levels, compared with the traditional sintering cycle.

Since the commercialization of the starting powders of β Ti-alloys is not as mature as that of Ti-6Al-4V, etc., their impurity levels such as oxygen generally are much higher, especially the refractory elements (Nb, Zr, Ta, etc.), which can be seen in **Table 3** and **Table 4**. Therefore, in order to achieve sufficient ductility in PM β Ti-alloys, the tailored usage of the RE-series sintering cycle to restrict the solid solution oxygen equivalent below the critical level is necessary. This prevents structural materials from brittle fracture failure. However, the current Y-containing method also brings about some obvious disadvantages, e.g. increased porosity, in terms of mechanical properties. Upgrading the Y-containing method, therefore, is very important. For the addition of Y powder, powder with the maximum particle size of 12 μm (i.e. 1200 mesh) should be selected. Irregular shaped particles are acceptable because no premature fracture due to stress concentration induced by particle geometry has been found. Regarding the weight percentage of Y addition, the solid solution oxygen equivalent ($O_{\text{sseq.}}$) has to be restricted to just below ≈ 3760 ppm like in the case of 0.3 wt.% Y addition in the present study. This is beneficial to obtain the best toughness and elongation to fracture and retain the original tensile strength.

5.2 TiC_x redistribution sintering cycle for MIM β Ti-alloys

5.2.1 Particle redistribution behavior

In this study, it is thought that carbon contamination in Metal-Injection-Molding technology originates from the sintering atmosphere (the main source), the debinding process (mainly thermal debinding) and the starting powders. These unavoidable carbon contamination sources

cause the precipitation of titanium-carbides (TiC_x). These titanium-carbides precipitate along prior β grain boundaries (GB), i.e. in the form of an aligned GB- TiC_x distribution, as displayed in **Figure 37** in MIM-processed β Ti-alloys (Ti-10Zr-20Nb, in wt.%) produced by a conventional-sintering cycle. This distributional feature is practically the same as in many previous reports [19, 20, 99, 110, 146, 150, 194] and can be considered as the most common type of titanium carbides precipitation in PM β Ti-alloys.

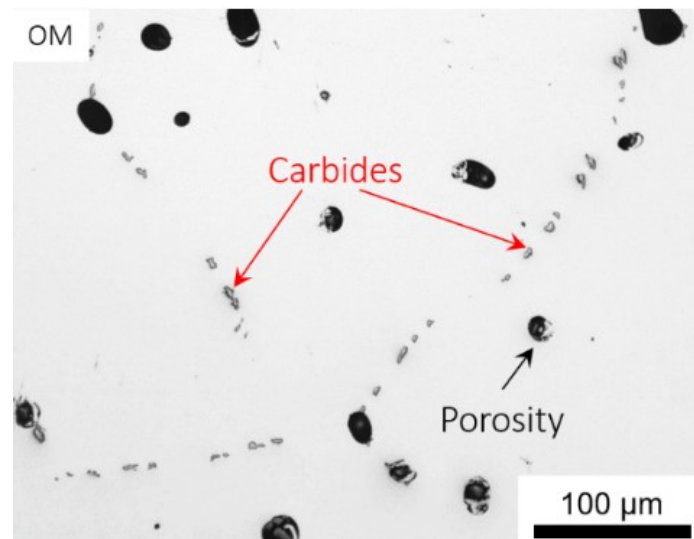


Figure 37 - Titanium-carbides (TiC_x) precipitate along prior β grain boundaries (GB), i.e. in the form of GB- TiC_x in MIM Ti-10Zr-20Nb.

It was shown, that by a combination of adding 0.1 wt.% Y (or Y-addition) and CSRA the adjustment of the distributional pattern is changed from aligned platelet-shaped GB- TiC_x to dispersed spheroidal intragranular TiC_x particles. Additionally, the majority of intragranular TiC_x particles still has a precipitation preference on the bundles of α_s -laths and walls of pores rather than being purely random. A schematic diagram of TiC_x redistribution behavior effected by Y-addition and CSRA is shown in **Figure 38**.

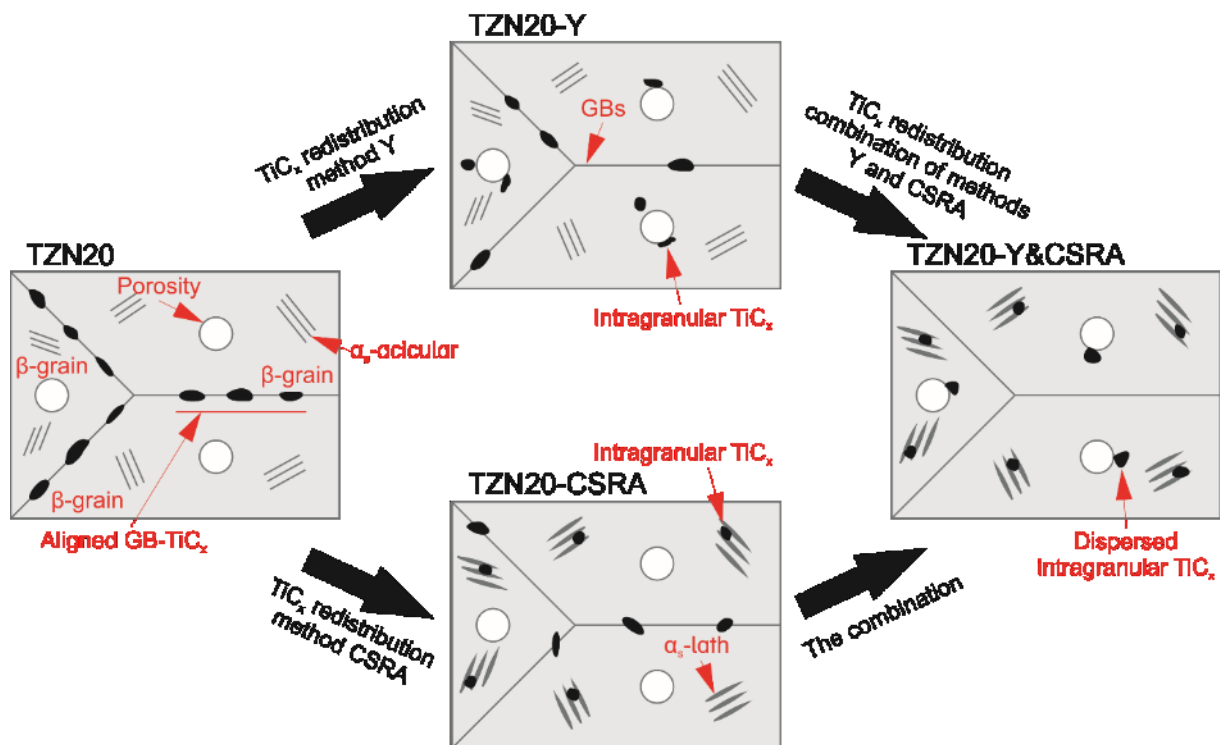


Figure 38 - Schematic diagram of mechanisms to adjust TiC_x particle distributional patterns by controlling TiC_x precipitation location by using methods of Y addition, CSRA, and their combination [107].

An explicit clarification of this TiC_x redistribution mechanism is needed in order to control the TiC_x particle distribution and to design appropriate procedures to achieve it. The particle redistribution by CSRA is an interplay between TiC_x dissolution and reprecipitation as elucidated in the following. The corresponding temperature ranges of the Regions of TiC_x -related reactions are also illustrated by **Figure 39**.

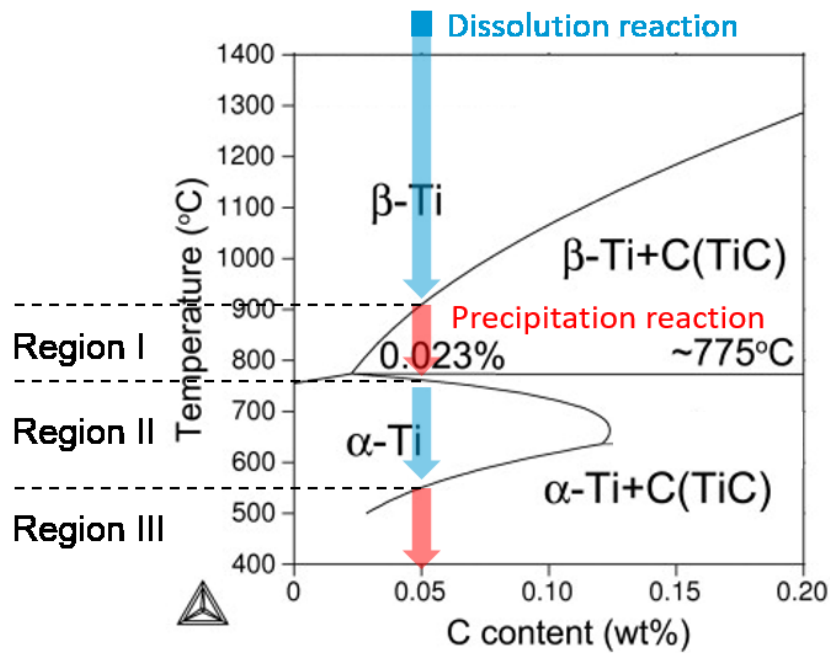


Figure 39 - The β Ti-C quasi binary phase diagram [141] indicates the corresponding temperature ranges of the Regions of TiC_x -related reactions (dissolution or precipitation reactions).

- i) Above α/β Ti transus (Region I), due to the shrinkage of the β -Ti lattice during cooling carbon atoms begin to gather at β -Ti grain boundaries. This effect is the well-documented precipitation evolution of GB- TiC_x [146, 179, 194] (can also see **Figure 34**). Carbon atoms in GB- TiC_x are generally released from β -Ti phase, which is the so-called “inherent precipitating parent”.
- ii) As the temperature drops below α/β transus (Region II), secondary α -Ti phase grows inside of the prior β -Ti grains [6, 200, 205-207]. The hcp α -Ti phase offers lattice sites that are more effective to dissolve carbon atoms than the interstices provided by bcc β -Ti, as already discussed in the introduction. During sufficiently slow cooling or holding at the respective temperatures (e.g. CSRA), carbon atoms that resided in β phase prefer to diffuse into these octahedral interstitial sites in the forming α -Ti phase. In Region II, the carbon solubility in Ti-matrix is significantly increased and accordingly TiC_x particles (carbon atoms) dissolve. In this regard, it is conceivable that “interstitial diffusion” occurred during this carbon diffusion process. In Region II, breaking of Ti-C bonds, growth of acicular secondary α -phases and dissolving GB- TiC_x by intragranular coarse laths of α -phases likely take place simultaneously. However, these processes, and the diffusion of carbon

atoms from the GBs into the interior of prior β grains, are time-consuming, while the lattice steadily shrinks as the temperature drops. It is associated with the delay of TiC_x precipitation peak, i.e. the peak value is reached at a slightly lower temperature (see **Figure 34**) rather than exactly at the α/β transus (810 °C). This process continues until the increased carbon solution capability of α -Ti due to its octahedral voids is counterbalanced by continuous lattice space shrinking due to temperature decrease.

- iii) Shortly after that, the intragranular TiC_x reprecipitates at a significantly lower temperature (Region III). In this case, carbon atoms to form intragranular TiC_x mostly are released from the precipitating parent of α -Ti. The intragranular TiC_x particles precipitate nearby the bundles of laths of secondary α -Ti (interior of β -Ti) by a slow diffusion rate, since carbon diffusion rate at low temperature region is by far smaller than in high temperature region I. This trapping (i.e. slow diffusion) is not only related to relatively low temperature, but also to a structurally lower atomic diffusivity in hcp α -Ti with its closed packed crystal structure compared to bcc β -Ti. Note that α -Ti lath bundles might be a prerequisite for intragranular precipitation, in addition to a sufficient carbon saturation of the α -Ti phase for TiC_x particle nucleation and growth. Hence, it is assumed that this CSRA method is limited to metastable β Ti-alloys with a certain fraction of secondary α -Ti. Stable β Ti-alloys with no or only a small fraction of secondary α -Ti might be not appropriate for designing such a special sintering cycle.

The redistribution behavior after adding Y is likely affected by the much lower precipitation temperature of TiC_x . Consequently, the extremely low diffusion rate of carbon atoms is a strong barrier for the formation of GB- TiC_x on the exterior of β -Ti grains. As reported by Chen et al. [146], intragranular TiC_x particles were observed in β -Ti alloys containing Ta and V as β -stabilizers. It was claimed that owing to their larger lattice interstitial sites, carbon atoms can remain dissolved in the Ti matrix during the cooling procedure until a relatively low temperature is reached, where TiC_x begins to precipitate. A possible explanation for lowering the precipitating temperature of TiC_x by Y could be that both Y and TiC_x are oxygen getters. In principle, 0.1 wt.% Y getter can scavenge up to 60 at.% of oxygen, while ≈ 0.5 wt.% TiC_x getter basically contains below 10 at.% oxygen [57]. It seems to indicate that the solubility of carbon at high temperatures in Ti-alloys can be affected by the oxygen concentration of the Ti-matrix. Oxygen atoms at grain boundaries, in turn, are likely necessary for the formation of GB- TiC_x [123, 208], due to TiC_x in PM Ti alloys actually is a hybrid phase including oxygen

atoms. However, grain boundary oxygen is easily scavenged by Y due to short-circuit diffusion. In this case, TiC_x may nucleate elsewhere, e.g. on porosity with a relatively high oxygen content and lattice flaws. An obvious example is given below (see **Figure 40**). This influence will be investigated in more detail in future work.

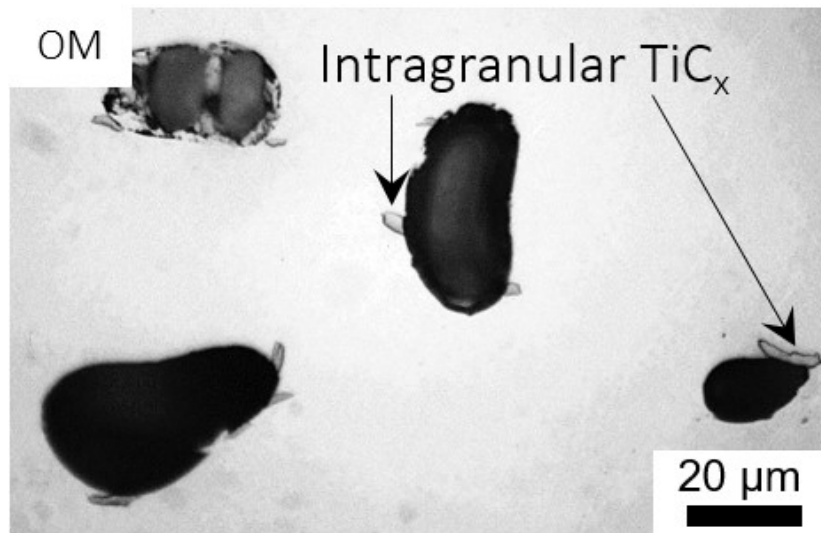


Figure 40 - Clear evidence of TiC_x phases nucleating e.g. on porosity with a relatively high oxygen content and lattice flaws. It is frequently found that TiC_x phases are formed in the walls of the porosity in Y-added TZN β Ti-alloys.

5.2.2 Microcrack initiation and crack propagation mechanisms in specimens with different TiC_x partial distributional patterns

We have shown that two strikingly different tensile fracture behaviors occur in MIM Ti-10Zr-20Nb alloys with aligned-agglomerated and evenly-dispersed TiC_x particle distributional patterns. The aligned pattern strongly degrades elongation to fracture in comparison to the dispersed ones. It has been fairly well-established in this study that “early-existing” microcracks initiate in TiC_x particles and the cracks coalesce along the continuously aligned GB- TiC_x particles.

Microcrack initiation mechanism

Cracking is hardly ever found in the soft Ti-matrix away from TiC_x . Microcracks only exist either in a singular particle (dispersed TiC_x) or frequently connected between GB- TiC_x particles (aligned TiC_x). The critical cracking of the whole specimen invariably originated from TiC_x .

No microvoids or other types of defects of the β Ti-matrix could be found as possible crack initiation sites; while the ruptured TiC_x particles represent “early-existing” microcracks responsible for fracture of the whole specimen.

Previous studies have shown that the tensile fracture of MIMed Ti-Nb is accompanied by a large number of ruptured TiC_x already at as low tensile strains as 1.4% [84, 99]. Analogously, in literatures [209, 210], it has been found via *in situ* microscopy that TiC particles and TiB whiskers begin to crack even before reaching the overall yield stress in unalloyed titanium. Thus, it can be assumed that TiC_x particles in present MIM Ti-10Zr-20Nb alloys begin to fracture early at a rather low strain. This is because of load-sharing effects transferring force from the soft Ti-matrix to the stiff TiC_x [211, 212] (≈ 180 GPa in carbon-deficient carbides [141]). Due to the brittle nature and the high crystallographic symmetry of TiC_x , a rapid through-thickness cracking occurring in TiC_x particle takes easily place. The formation of such cracks is typical for microcrack initiation of the whole MIM-TZN material.

Multiple cracking (e.g. see **Figure 32** (f)) of TiC_x particles is possibly a consequence of dislocation pileups (local stress concentration). These dislocation pile-ups were mainly generated from i) geometrically necessary dislocations arising from strain incompatibility, ii) processing residuals (e.g. minor thermal stress, etc.) and iii) dislocations stopped at TiC_x particles from Ti-matrix plastic deformation via dislocation flow [213-215]. Both the premier microcracks and repeated cracks of TiC_x basically possess the same potential to contribute to crack coalescence propagation in the whole material.

Crack propagation modes in MIM-TZN alloys with aligned GB- TiC_x and dispersed intragranular TiC_x

The great extent of crack-tips blunting or large COD (crack opening displacement) ahead of “early-existing” microcracks indicate that crack propagation was contained within stiff TiC_x particles rather than immediately penetrating into the soft Ti-matrix. Large COD is the consequence of severe localized plastic strain of the Ti-matrix emanated from crack-tips. Providing such large localized plastic deformation suggests the β matrix of MIM-TZN possesses a good inherent toughness.

In general, there exist distinctly different thresholds for crack propagation in ductile Ti-matrix and brittle ceramic TiC_x -particles [216, 217]. The trigger of crack propagation in ductile metals can be expressed by the A. Wells empirical equation based on an elastic-plastic fracture model [218].

$$\delta = 2\pi e a_i$$

Where δ is a constant in ductile materials and is the critical COD, e is the nominal strain and a_i is the initial crack length, i.e. the ruptured TiC_x in this study.

Therefore, a large COD ahead of “early-existing” microcracks indicates that a large nominal strain e is required to trigger crack propagation. Furthermore, it is widely recognized that Ti-alloys have a rather low work-hardening rate. As a paradox, this is advantageous to restrict stress localization ahead of crack-tips, but simultaneously leads to severe strain localization [151]. This synergy results in the observed localized severe plastic deformation ahead of crack-tips. With the strain increasing, when the critical COD is reached, “early-existing” microcracks, which were trapped in TiC_x particles, eventually propagate into the β -matrix.

For the cases of aligned GB- TiC_x particles, crack propagation takes place by connecting the continuously aligned “early-existing” microcracks. In brief, this is a combination of crack propagation modes consisting of microcracks coalescence mode and crystal defects cleavage fracture mode. Their detailed mechanisms are given here. First of all, there are relatively high impurity levels (Fe, P, Cl, S and so forth [219]) and lattice defects present at grain boundaries, which typically offer significantly poorer atomic bonding. Furthermore, crack coalescence commonly seeks the shortest path to link these “early-existing” cracks due to the lowest tearing energy consumption. Therefore, it is theoretically impossible that the critical crack bypasses these “early-existing” cracks (voids) in GBs and tore the strong atomic bonds of the Ti-matrix. This combination of fracture modes observed here is in good agreement with existing intrinsic mechanisms of damage (cleavage fracture and micro-voids coalescence) promoted crack advance [151, 220, 221]. This is shown schematically in the diagram in **Figure 41** (a).

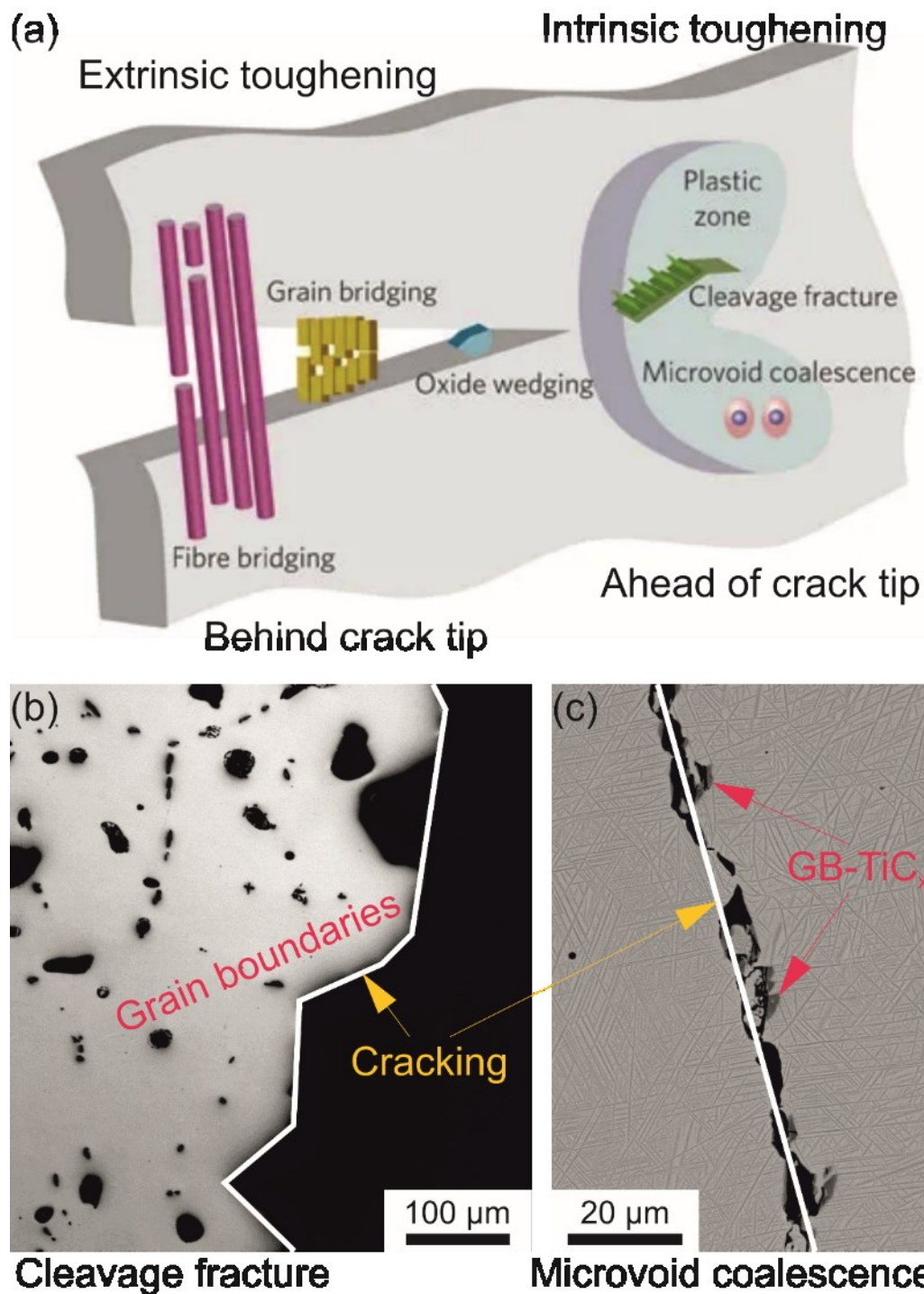


Figure 41 - Schematic diagram of a combination of crack propagation modes containing microcracks coalescence mode and crystal defects cleavage fracture mode caused by aligned TiC_x second phases [221].

By contrast, in evenly-dispersed particle distributions paths to connect “early-existing” microcracks are more twisting and require an appreciable higher tearing energy. Moreover, the crack bridging effect and atomic bonding in the interior of β -grains are strong. Thus, crack

propagation is much more difficult in MIM-TZN with evenly-dispersed TiC_x particle distribution. Because their strength is nearly equivalent, the toughness of MIM-TZN alloys with different TiC_x particle distribution patterns is mirrored by their elongation to fracture (ϵ_f) from 3.9% in the aligned TiC_x cases to 8.3% in the dispersed ones. Furthermore, different precipitation locations of TiC_x second phases lead to extremely different particle distributional patterns. This apparent difference linking to fracture toughness of MIM TZN alloys are illustrated in **Figure 42**.

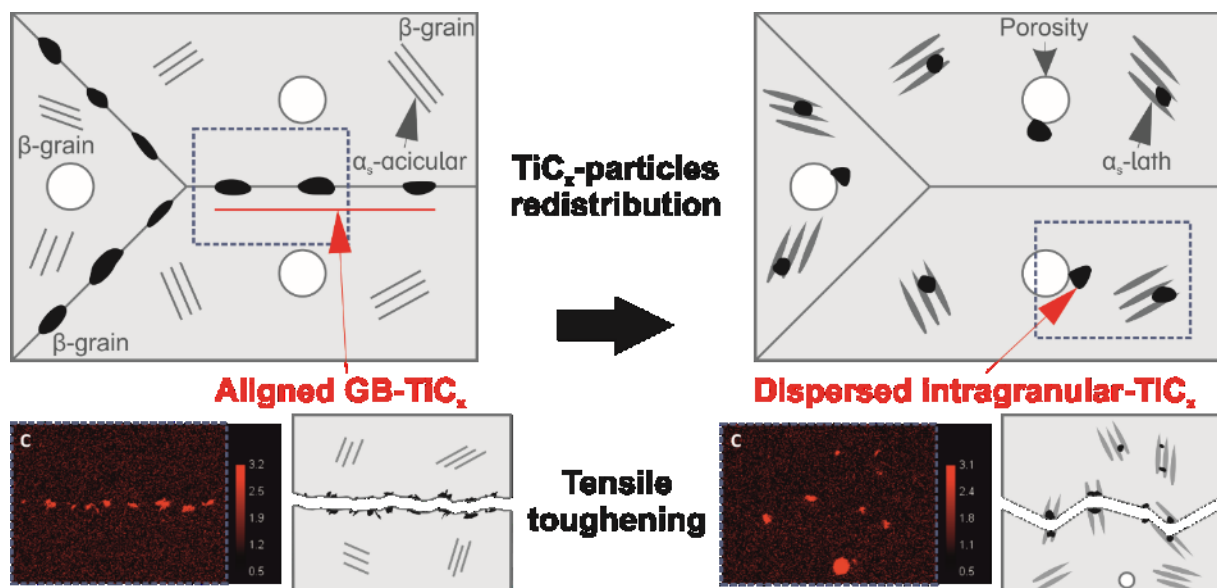


Figure 42 - Illustration of different particle distributional patterns of TiC_x second-phase and the corresponding fracture propagation modes of MIM TZN alloys [107].

From the comparison of the tensile properties in **Figure 43**, the elongation of TiC_x -redistributed TZN20 is much higher than the majority of reported MIM β Ti-alloys [21, 84, 99, 150, 222-226]. Compared with pre-alloyed powder prepared Ti-24Nb-4Zr-8Sn [150] and Ti-15V-3Al-3Sn-3Cr [223] with the same level of elongation, it could offer a 120 ~ 180 MPa higher tensile strength.

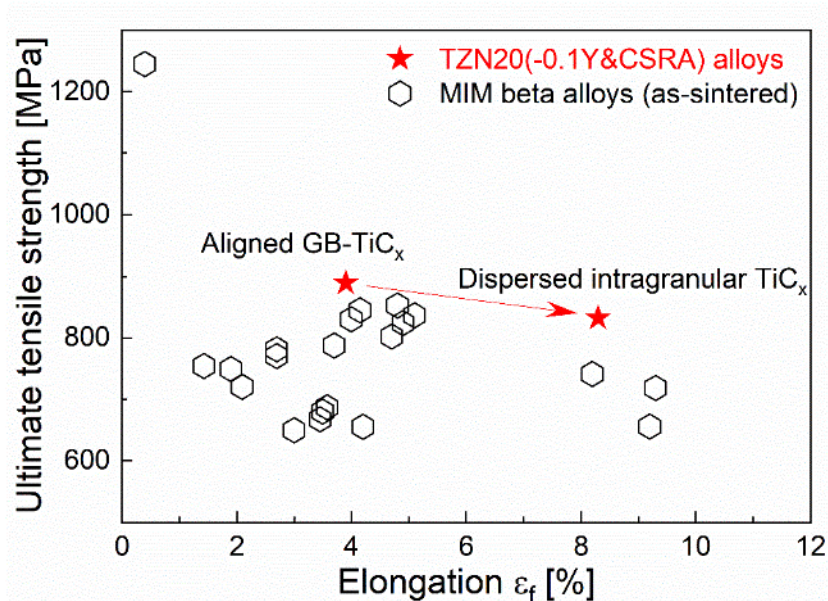


Figure 43 - Comparison of elongation to fracture (ϵ_f) and ultimate tensile strength (σ_{UTS}) of different MIM-processed β Ti-alloys from literature and present MIM-TZN20 alloys with different TiC_x particle distributional patterns [107].

5.2.3 Additional effects of CSRA and Y addition on the Ti-matrix except for TiC_x redistribution

In order to determine the impact of particle redistribution on tensile toughening without interference from other possible impact factors caused by the treatment methods, we took other effects of these TiC_x redistribution methods into consideration. They are separately discussed in this section.

The prolonged exposure to a rather high temperature during CSRA might have an influence on Ti-matrix, e.g. stress relieve of the low residual stresses of as-sintered material. In this study, in order to distinguish those additional effects, the same CSRA step was applied to the reference group TZN18-0.1Y(&CSRA). Both variants with dispersed TiC_x were basically equal in terms of particle distribution pattern because of a low TiC_x fraction (see **Table 14**). An evaluation of the toughening (improvement of ϵ_f) mechanisms in MIM-TZN alloys after CSRA is shown in **Figure 44**. We only can see a negligible increment of elongation in the reference group. It is evident from the results that TiC_x redistribution behavior induced by CSRA contributes mainly to the toughening effect in the TZN20 series.

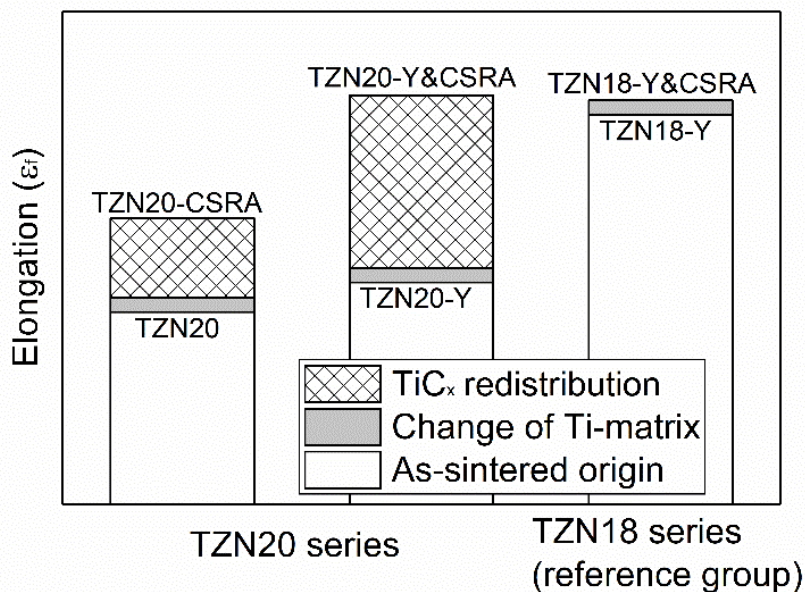


Figure 44 - Illustration for detailed effects (incl. TiC_x redistribution and the extra) of CSRA on the elongation improvement of MIM-TZN alloys [107].

Other effects on the microstructural-scale related to Y addition are summarized in **Table 19**. The porosity, oxygen level and prior β grain size were slightly altered (see the lower half of **Table 19**). The early-formed large yttria particles obstruct material diffusion in sintering, resulting in increasing porosity. Generally acknowledged, porosity is detrimental to tensile elongation. Thus, especially large-sized elemental Y powder should be used with some reservation. The addition of 0.1 wt.% Y could scavenge oxygen atoms and the resulting slightly lower oxygen level (0.027 wt.%) of the Ti-matrix may improve ductility [109]. Nonetheless, it has been widely accepted that β Ti alloys can tolerate a relatively higher oxygen concentration (≈ 0.8 wt.%) without a slump in elongation [124]. Thus, the effects of a possible decrease in oxygen level in this case might be insignificant. In addition, a smaller average grain size suppresses crack initiation, whereas a large grain size could resist crack growth, which is more important in toughening [1]. Consequently, a quite negative effect of porosity caused from Y addition is likely to offset a certain degree of improvement on elongation arising from TiC_x redistribution behavior.

Table 19 - Overview of multiple impact factors of Y addition on tensile toughness (here, represented by ε_f) of MIM-TZN20 with respect to TiC_x -particle and Ti-matrix [107].

Aspect	Impact factor	TZN20 ($\varepsilon_f = 3.9\%$)	TZN20-0.1Y ($\varepsilon_f = 4.5\%$)
TiC_x - particle	Volume fraction	0.53 vol.%	0.48 vol.%
	Mean particle size	6.6 μm	5.8 μm
	Mean aspect ratio/ unitless	2.55	2.28
	Particle distributional pattern	basically aligned	partially aligned
	Location of precipitation	basically along GBs	partially along GBs
Ti- matrix	Porosity	5.0%	6.0%
	Oxygen in solid solution*	0.265 wt.%	0.224 wt.%
	Prior β -grain size	373 μm	301 μm
	Secondary α -phase morphology	fine, acicular	fine, acicular

*0.1 wt.% Y particles can scavenge ≈ 0.027 wt.% O atoms from Ti-matrix to form yttria (Y_2O_3) during the sintering process. Therefore, the oxygen in solid solution decreased in TZN20-0.1Y.

5.2.4 Influence of geometrical characteristics of TiC_x particles

From the perspective of crack initiation, a high volume fraction of hard particles may provide a high-density of early-existing microcracks. The particle size in some cases correlates to the size of flaws. Although such characteristics typically degrade intrinsic toughening mechanisms, the reinforcements can also cause crack deflection or crack bridging as extrinsic toughening mechanisms during crack growth [151]. Nevertheless, as it is often the case, toughening is merely due to decelerated crack growth rather than crack initiation [221], especially when microcracks initiate fairly early. As illustrated by **Figure 45**, volume fraction and particle size do not show a pure monotonic linear relationship with elongation. It is unclear if the influence of them is either positive or negative on tensile toughness, but at least they are not the dominating factors.

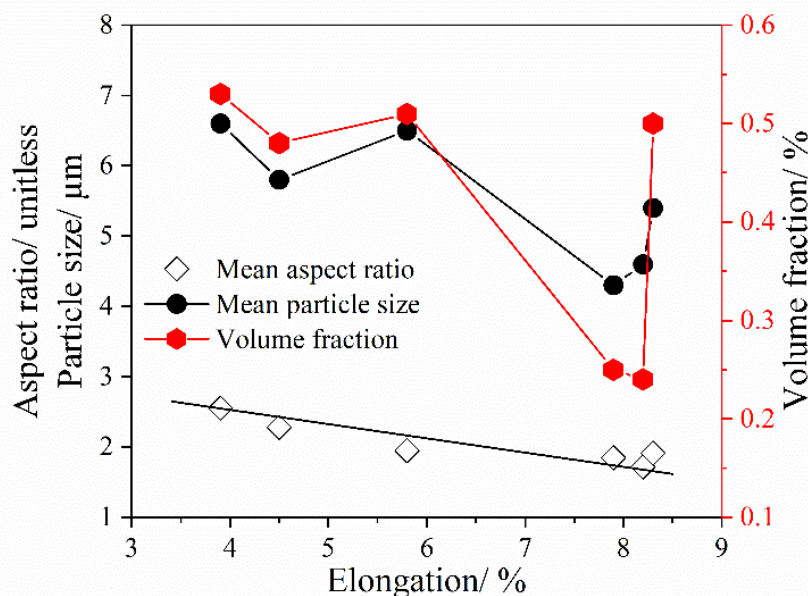


Figure 45 - Elongation to fracture (ϵ_f) in relation to TiC_x particle characteristics (incl. volume fraction, mean aspect ratio and particle size) of the MIM-TZN alloys [107].

Large aspect ratio of GB- TiC_x is commonly caused by grain boundaries being area defects and their according influence on nucleation [113, 227-229]. However, GB- TiC_x could exhibit slightly different geometrical morphologies, which is either elongated-shape in the alloys with high volume fraction of TiC_x (e.g. ≈ 3 vol.%) [110, 141, 146, 194] or platelet-shaped particles in alignment when the volume fraction of TiC_x is low as in TZN20 of this study or Ti-24Nb-4Zr-8Sn (≈ 1 vol.%) [150]. By contrast, intragranular TiC_x shows a small aspect ratio. Interestingly, the aspect ratio of TiC_x in TZN20 series was found to be much reduced after CSRA (see **Figure 46** (a)-(b)), due to GB- TiC_x being transformed to intragranular TiC_x .

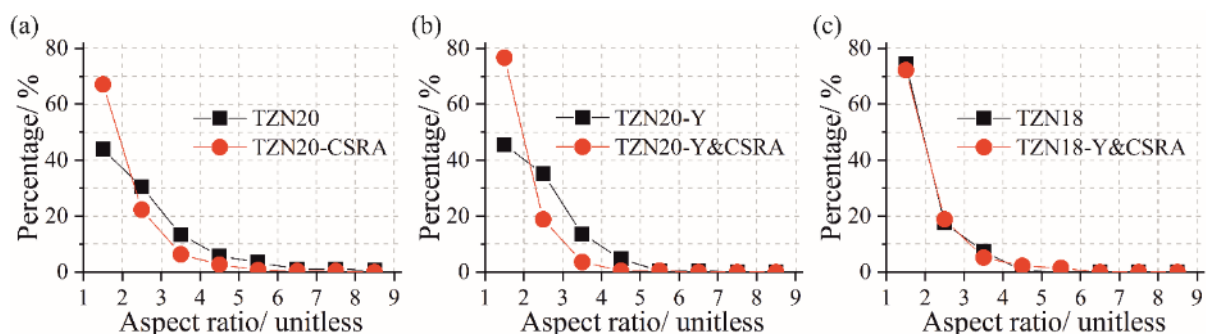


Figure 46 - Influence of CSRA on the aspect ratio distribution of TiC_x particle in (a) TZN20 and TZN20-CSRA; (b) TZN20-0.1Y and TZN20-0.1Y&CSRA; (c) TZN18-0.1Y and TZN18-0.1Y&CSRA (reference group) [107].

However, it is thought that there is not much practical impact on toughening offered directly from aspect ratio itself, unless a considerably large aspect ratio or elongated shape might have more or less influence on crack initiation that is not so important compared with microcracks coalescence mode and crystal defects cleavage fracture mode in this study.

6. Technical perspectives

6.1 A comparison among various powder metallurgical processing of β Ti-alloys

In the past ten years, the research and development on β Ti-alloys fabricated via powder metallurgical routes has significantly increased. Initially, it was designed to manufacture complex-shaped Ti-components with a high “performance-to-cost” ratio and/or some special functions (e.g. high specific strength and low Young’ modulus) in a streamlined and industrial way (i.e. mass production). Nevertheless, as aforementioned in Section 1.3, the three major processing defects strongly degrade the specific mechanical properties of the material. Amid them, the most concerning for PM β Ti-alloys in engineering structural applications are the deterioration of toughness and fatigue. Therefore, the materials fracture failure caused by the three major processing defects exists in these materials during service under static and/or dynamic loading.

According to the state-of-the-art, a number of solutions to the four aspects (as listed in the following) have been reported. They are capable of mitigating the mechanically detrimental factors (or defects) and enhancing Ti alloys performance. In this regard, these solutions mainly include (i) altering processing technology (such as forming techniques, consolidation means, and sintering pathways), (ii) exploiting technical precautions (e.g. burn-out, oxygen traps, sintering supports and contamination-shielding facilities), (iii) upgrading raw materials and devices (starting powders, binder system, and special furnace), and (iv) employing post-treatment (HIP, WQ, TMP, and cold working).

Consequently, it is of interest to compile an overview of PM β Ti-alloys correlating the elements of “processing technic”, “microstructure & composition” and “mechanical performance”. Through comparing and discussing these various routes or means in the literature and the present study, a comprehensive understanding can be gained. This can be helpful to identify the optimal powder metallurgical processing strategies, which can provide satisfactory mechanical properties or the tailored PM β Ti-alloys, with special mechanical performance.

From the literature records, for PM β Ti-alloys, a MIM Ti-13Mn alloy with an additional cold rolling post-sintering treatment gave the highest ultimate tensile strength (UTS) of 1852 MPa. That is because the cold mechanical processing is always capable to close residual porosity, refine the prior β grain structure and provide plentiful dislocations which consequently contribute to the considerably high tensile strength. By contrast, as-built Ti-25Nb-3Zr-3Mo-2Sn via SLM without any post heat treating exhibited a as high as 37% elongation to fracture [93]. With respect to the excellent ductility, as basically shown in the SLM β Ti-alloy, the absence of three major processing defects and the nature of good deformation ability in β phase structure of β Ti-alloys can account for the fairly high elongation.

The level of impurities and relative density between SPM and FPM show a very different tendency. This can be mainly attributed to the duration at high temperature during powder consolidation and the usage of different starting powders, which involves a contamination uptake issue. Simply speaking, these β Ti-alloys fabricated by FPM routes normally reach more than a 99.5% relative density as well as possess a fairly low impurities level. Furthermore, between these two PM routes (SPM and FPM), there are some differences including residual processing stresses and phase precipitation (second-phase, generally acicular secondary α -phases) strengthening, which both are mostly caused by cooling rate, can also lead to a big discrepancy in mechanical performance.

In order to get a more concise picture on how processing routes affect the mechanical properties, the strength and ductility of SPM (MIM, conventionally pressed and sintering, etc.) and FPM (incl. SLM, EBM and LMD) β Ti-alloys are summarized in a mechanical property map given in **Figure 47** and compared with values reported in literature for wrought-processed (WP) β Ti-alloys and as-sintered Ti-6Al-4V. As indicated in **Figure 47**, SPM β Ti-alloys have the potential to reach very high strength, but normally give a rather low ductility. However, there is basically no embrittlement problem in FPM-produced β Ti-alloys, while they still possess a satisfactory strength performance. Different with PM routes processing, the β Ti-alloys manufactured by WP routes show a balanced combination of strength and ductility. For ingot metallurgy route, it is generally acknowledged that β type Ti-alloys (β alloys) have a better toughness than traditional $\alpha+\beta$ type Ti-alloys (e.g. Ti-6Al-4V). In the case of PM, as shown in **Figure 47**, the results show the opposite. A possible reason for this could be the premature fracture induced by GB-TiC_x during tensile tests, which has been elaborated before. Though the present investigation of optimizing Y-containing and novel TiC_x redistribution sintering

cycle, a new border for the combination of strength and elongation of as-sintered β Ti-alloys is reached, as showed by a pentastar. Adjusting the TiC_x particles distribution pattern can significantly reduce the adverse effects of aligned GB- TiC_x phases. However, minimally negative effects of them still exist.

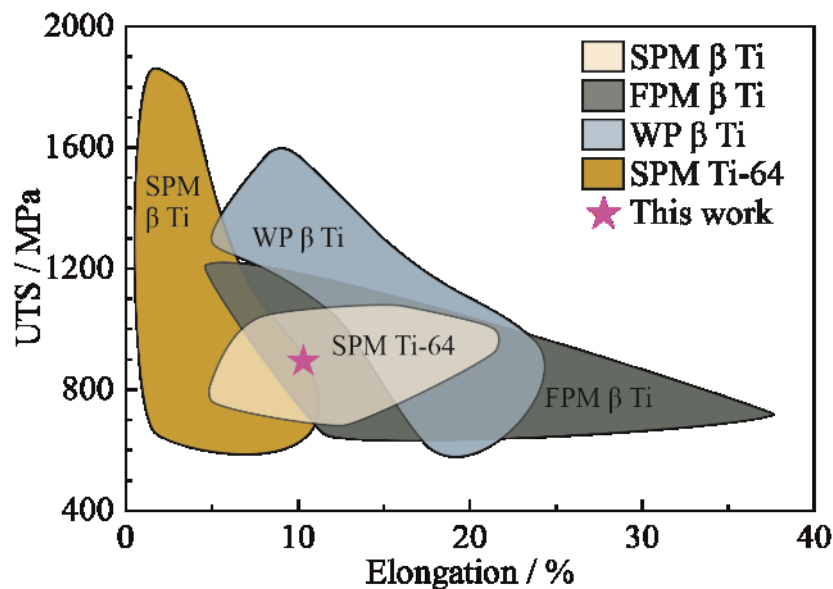


Figure 47 – A mechanical property map (SPM β Ti, incl. this study, and FPM β Ti) compared with literature-reported values for wrought-processed β Ti-alloys (WP β Ti) and traditional PM Ti-6Al-4V (SPM Ti-64).

*SPM: sintering-based powder metallurgy; FPM: fusion-based powder metallurgy; WP: Wrought processing

6.2 Comparison with literature of MIM β Ti-alloys and effectiveness assessment for post-sintering treatments

Metal injection molding (MIM), as a powder forming technology, is part of SPM routes. Likewise, unsatisfactory damage tolerance (or low elongation to fracture) is a main concern for MIM β Ti-alloys as well. Up to now, regarding the solutions for the embrittlement problem of MIM β Ti-alloys in the literature, the post-sintering treatment, incl. hot isostatic pressing (HIP), water quenching (WQ) and thermo-mechanical processing (TMP), is frequently employed to improve crack resistance. This is done through (i) dissolving/crushing the toughness-unfavorable phases (GB- TiC_x precipitates); (ii) closing the internal porosity; (iii) refining the originally coarse β grains.

Certainly, many technical precautions like high-purity starting powders, the use of pre-alloyed (PA) powders (beneficial for densification and reduced impurity levels), high-concentration alloying to increase carbon solubility, optimized binder system, and special furnaces, etc. have been put into effect with the purpose of improving the damage tolerance of MIM β Ti-alloys. Even though they are effective to some extent, they are not the focus of the technical discussion in this section. The focus of our discussion is on non-technical preventive means.

The values of strength and ductility of MIM β Ti-alloys which experienced different post sintering treatments from literature [19, 20, 61, 62, 84, 99, 150, 179, 194, 222-225, 230-234] are compared with the results of the present study and are plotted in **Figure 48**.

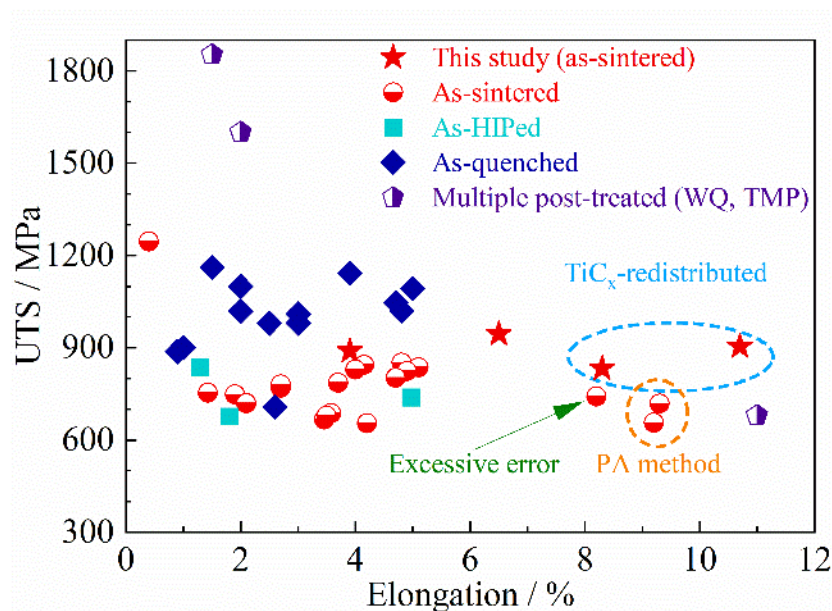


Figure 48 – Mechanical properties of MIM β Ti-alloys with various post treatments. In addition, the points with high elongation to fracture are explained.

We can see that as-sintered MIM β Ti-alloys marked by the red color, in most cases, exhibit an intermediate strength of less than 850 MPa, and a low elongation below 5%, which are common results in many reports [84, 99, 194, 230, 232], except good elongation results from PA method fabricated alloys and rather large deviations. The hot isostatic pressing (HIP) post-treatment (see As-HIPed cases marked by cyan square) can effectively close the standard residual pores, and it gives an apparent improvement in the porosity from the original sintered state but neither

improves strength nor ductility as expected [84, 99, 230]. The structural coarsening behavior in prior β grains and secondary α phases likely counteracts the increased strength derived from the closure of porosity, while GB-TiC_x still exists and continues to deteriorate the materials fracture resistance. Using solid solution followed by water quenching (WQ) can generate residual thermal stress and hard martensitic phases in some cases, thereby increasing the strength of MIM β Ti-alloys (see As-quenched). Quenching post treatment is often used in PM β Ti-alloys, to solve the GB-TiC_x problem. In general, the stiff and unfavorable phases of GB-TiC_x, will disappear in the as-quenched state. Nonetheless, the newly introduced internal stresses and hard martensitic structure will largely worsen the ductility. The best ductility of MIM β Ti-alloys in **Figure 48** ($\approx 11\%$) comes from Ti-22Nb alloy with a multiple post treatment of HIP followed by WQ. It is by far the most effective solution, but rather complicated and energy-intensive.

In comparison with these solutions from literature, the novel sintering pathway, using the means proposed by the present project, produced as-sintered β Ti-alloys without any post-sintering processing which provided a significant improvement to elongation. This can be seen in **Figure 49**. Simultaneously, when a mild technical precaution strategy is used, such as using optimized MA (master-alloy) and elemental powder, the elongation to fracture can reach a higher value. The MIM-TZN alloys with a $\approx 3\%$ porosity achieved the highest tensile toughness (UTS = 904 MPa, $\epsilon_f = 10.7\%$) among all published MIMed β Ti alloys (incl. the post-sintering treated cases). The supplementary MIM-TZN alloys with the low porosity (reaching a standard MIM-sintered porosity) were prepared by $<45 \mu\text{m}$ Ti-42Nb spherical master-alloyed (MA) powder, $<45 \mu\text{m}$ Zr spherical powder, etc.; whereas the ones with 5–6% porosities were prepared by $<63 \mu\text{m}$ Ti-42Nb spherical MA powder, $<45 \mu\text{m}$ Zr angular powder, etc. (only note their differences here, for other details refer to Section 3.2.1).

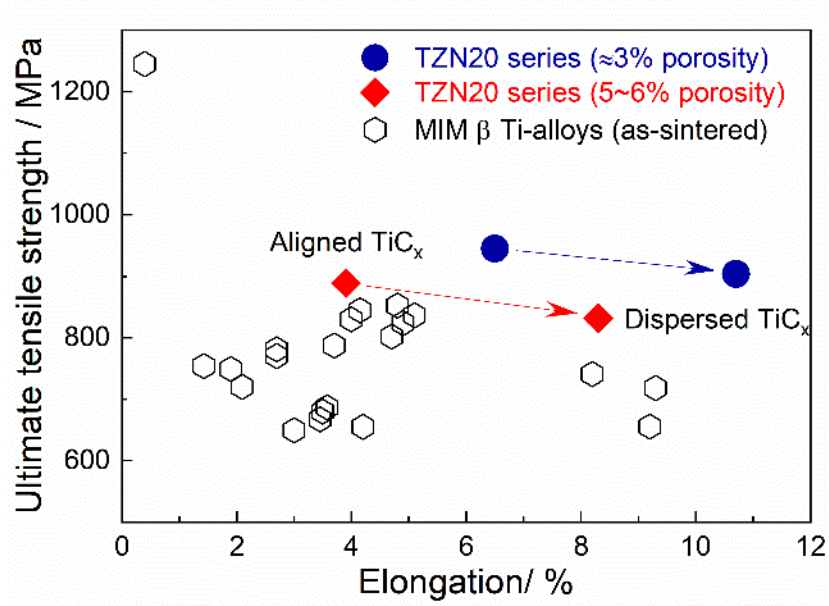


Figure 49 – Tensile toughening in the MIM-TZN alloys with low and high porosities by adjusting particle distribution pattern [107].

7. Conclusions and future work

Optimizing RE-series sintering cycle

From the examination of metal-injection-molded Ti-20Nb-10Zr (MIM-TZN20) biomedical β Ti-alloys manufactured by rare earth (RE) sintering cycle, it was found that employing the Y (RE-element) sintering cycle can enhance the toughness of MIM-TZN20 alloys. In addition the Y (RE-element) sintering cycle has still potential for further improvement through optimization. Specifically, MIM-TZN20 alloys with diverse Y additions were fabricated by metal injection molding. The effects of Y-induced oxygen scavenging, microstructure refinement and increased porosity on tensile properties were systematically investigated.

The addition of Y elemental powder with a particle size of more than $\approx 15 \mu\text{m}$ leads to an increase in residual porosity and causes irregular and interconnected pores in the MIM-prepared Ti-Nb-Zr alloys. The large-sized Y is believed to form pore-area yttria which hinder elemental diffusion at elevated temperatures preventing pore closing. Grain boundary pinning by yttria was not found in this study. To scavenge oxygen from the Ti-matrix, Y elemental powder with a maximum particle size of less than $15 \mu\text{m}$ (e.g. $12 \mu\text{m}$ or 1200 mesh) is more appropriate and without significant detrimental effects on the as-sintered density. When the concentration of Y powder of a large particle size is more than 0.5 wt.%, degradation of ductility caused by excessive porosity becomes significant.

Y addition generally degrades the tensile strength, proportional to the Y concentration introduced. This degradation is mainly resulting from the increase in overall porosity, irregular sized pores, and the decrease in the solid-solution state oxygen (dissolved-O). Although, a grain size refinement is quite obvious (down to $187 \mu\text{m}$ from $373 \mu\text{m}$), a beneficial effect of it on tensile strength was not found.

Y addition in MIM-TZN20 alloys causes no observable effect on the area fraction of the TiC_x phase; in other words, oxygen concentration has no practical effect on carbon solubility at ambient temperature.

Engineering novel TiC_x redistribution sintering pathway

Metastable β -type Ti-Nb-Zr biotolerant materials were tailored and fabricated using metal injection molding (MIM) with ≈ 0.05 wt.% carbon residuals, which is a normal carbon contamination level for Ti-MIM. Identification for carbon contamination sources of this binder-based powder technology shows that improper thermal pyrolysis of polymers is not as critical as normally assumed. Instead, carbon uptake from sintering atmosphere is found more likely to play a significant role.

TiC_x redistribution methods, i.e. the combination of trace yttrium addition (Y) and carbide spheroidization reprecipitation annealing (CSRA), changed an aligned TiC_x distribution (obtained by conventional sintering program) to a dispersed TiC_x distribution in MIM-processed Ti-Nb-Zr alloys. It is found by EBSD that this adjustment of particle distributional patterns means, essentially, that aligned TiC_x particles along grain boundaries (GB-TiC_x) are dissolved and in the interior of β grains dispersed intragranular TiC_x is formed. HEXRD experiments using synchrotron radiation reveal that Y lowers the initial precipitation temperature of TiC_x, while CSRA effects the amount of partial GB-TiC_x second-phases that are dissolved within the Ti-matrix. In a word, TiC_x reprecipitates at a much lower temperature; intragranular TiC_x is thereby generated in a higher fraction via these methods.

Tensile toughness of MIM-TZN alloys with aligned and dispersed TiC_x particle distributional patterns are significantly different. The alloys with aligned GB-TiC_x exhibit premature intergranular fracture ($\varepsilon_f = 3.9\%$), whereas the alloys with dispersed TiC_x show a significant enhancement of toughness ($\approx 113\%$ increment in ε_f to 8.3%, the strength remains nearly equivalent). Inspections of fracture modes indicate that prematurely ruptured TiC_x particles act as “early-existing” microcracks. In addition, in GBs, crack propagation modes (incl. microcracks coalescence mode and crystal defects cleavage fracture mode) occur in these aligned “early-existing” microcracks as the dominant crack growth mechanism at rather low strain. The low tearing energy of these two negative crack growth modes causes low toughness of the alloys with aligned GB-TiC_x. Dispersed intragranular TiC_x requests more winding crack growth and possess stronger atomic bonding in the interior of β -grains than at GBs, acting as intrinsic toughening mechanisms.

To conclude, a novel toughening strategy to adjust particle distribution pattern (TiC_x phases redistribution) by regulating the precipitation evolution of TiC_x was successfully established. TiC_x redistribution methods are capable of eliminating aligned GB- TiC_x particles and can be applied to effectively toughen powder metallurgical β Ti-alloys (β alloys). This project aimed to establish a practical solution for the GB- TiC_x -induced embrittlement of PM β -Ti alloys due to the unavoidable carbon contamination issue. Replacing rigorous technical precautions and energy intensive post-treatments against carbon contamination and TiC_x formation by proper adjustment of TiC_x phases spatial distribution is an incentive for ongoing research.

References

- [1] C. Leyens, M. Peters, *Titanium and Titanium Alloys: Fundamentals and Applications*, Wiley-VCH, Weinheim, Germany, 2003.
- [2] I.V. Okulov, H. Wendrock, A.S. Volegov, H. Attar, U. Kühn, W. Skrotzki, J. Eckert, High strength beta titanium alloys: New design approach, *Materials Science and Engineering: A* 628 (2015) 297-302.
- [3] M. Niinomi, M. Nakai, J. Hieda, Development of new metallic alloys for biomedical applications, *Acta Biomaterialia* 8(11) (2012) 3888-3903.
- [4] A. Mishra, J. Davidson, P. Kovacs, R. Poggie, *Beta Titanium in the 1990's*, TMS, Warrendale, PA (1993) 61-72.
- [5] P. Bania, *Beta Titanium Alloys and their Role in the Titanium Industry*, Beta Titanium Alloys in the 90's, TMS Publications, Warrendale, PA, 1993.
- [6] F. Froes, H. Bomberger, The beta titanium alloys, *JOM* 37(7) (1985) 28-37.
- [7] R. Boyer, H. Rosenberg, *Beta titanium alloys in the 80's*, TMS-AIME publications, Warrendale, PA 1 (1984).
- [8] A. Vassel, Microstructural instabilities in beta titanium alloys, *Beta titanium alloys in the 1990's* 1993.
- [9] D. Eylon, A. Vassel, Y. Combres, R. Boyer, P. Bania, R. Schutz, Issues in the development of beta titanium alloys, *JOM* 46(7) (1994).
- [10] T. Saito, T. Furuta, J.-H. Hwang, S. Kuramoto, K. Nishino, N. Suzuki, R. Chen, A. Yamada, K. Ito, Y. Seno, Multifunctional alloys obtained via a dislocation-free plastic deformation mechanism, *Science* 300(5618) (2003) 464-467.
- [11] M. Niinomi, Mechanical properties of biomedical titanium alloys, *Materials Science and Engineering: A* 243(1-2) (1998) 231-236.
- [12] M. Niinomi, Recent research and development in titanium alloys for biomedical applications and healthcare goods, *Science and technology of advanced Materials* 4(5) (2003) 445.
- [13] M. Geetha, A.K. Singh, R. Asokamani, A.K. Gogia, Ti based biomaterials, the ultimate choice for orthopaedic implants—a review, *Progress in materials science* 54(3) (2009) 397-425.
- [14] S. Ankem, S. Seagle, Heat treatment of metastable beta titanium alloys, *Beta Titanium Alloys in the 80's* (1984) 107-126.
- [15] M. Bönisch, *Structural properties, deformation behavior and thermal stability of martensitic Ti-Nb alloys*, 2016.
- [16] L.-F. Huang, B. Grabowski, J. Zhang, M.-J. Lai, C.C. Tasan, S. Sandlöbes, D. Raabe, J. Neugebauer, From electronic structure to phase diagrams: A bottom-up approach to understand the stability of titanium–transition metal alloys, *Acta materialia* 113 (2016) 311-319.
- [17] M. Abdel-Hady, K. Hinoshita, M. Morinaga, General approach to phase stability and elastic properties of β -type Ti-alloys using electronic parameters, *Scripta Materialia* 55(5) (2006) 477-480.
- [18] F.H.S. Froes, M. Qian, A perspective on the future of titanium powder metallurgy, *Titanium Powder Metallurgy*, Elsevier 2015, pp. 601-608.
- [19] K. Cho, M. Niinomi, M. Nakai, H. Liu, P.F. Santos, Y. Itoh, M. Ikeda, T. Narushima, Improvement in mechanical strength of low-cost β -type Ti–Mn alloys fabricated by metal injection molding through cold rolling, *Journal of Alloys and Compounds* 664 (2016) 272-283.
- [20] P.F. Santos, M. Niinomi, K. Cho, H. Liu, M. Nakai, T. Narushima, K. Ueda, Y. Itoh, Effects of Mo addition on the mechanical properties and microstructures of Ti-Mn alloys fabricated by metal injection molding for biomedical applications, *Materials Transactions* 58(2) (2017) 271-279.
- [21] J.-E. Bidaux, R. Pasquier, M. Rodriguez-Arbaizar, H. Girard, E. Carreño-Morelli, Low elastic modulus Ti–17Nb processed by powder injection moulding and post-sintering heat treatments, *Powder Metallurgy* 57(5) (2014) 320-323.
- [22] C. Liu, L. Yu, A. Zhang, X. Tian, D. Liu, S. Ma, Beta heat treatment of laser melting deposited high strength near β titanium alloy, *Materials Science and Engineering: A* 673 (2016) 185-192.
- [23] R.R. Boyer, An overview on the use of titanium in the aerospace industry, *Materials Science and Engineering: A* 213(1-2) (1996) 103-114.
- [24] D. Dimiduk, Gamma titanium aluminide alloys—an assessment within the competition of aerospace structural materials, *Materials Science and Engineering: A* 263(2) (1999) 281-288.

- [25] M. Peters, J. Kumpfert, C.H. Ward, C. Leyens, Titanium alloys for aerospace applications, *Advanced Engineering Materials* 5(6) (2003) 419-427.
- [26] R. Boyer, R. Briggs, The use of β titanium alloys in the aerospace industry, *Journal of Materials Engineering and Performance* 14(6) (2005) 681-685.
- [27] M.J. Krane, A. Jardy, R.L. Williamson, J.J. Beaman, *Proceedings of the 2013 International Symposium on Liquid Metal Processing and Casting (LMPC)*, John Wiley & Sons 2013.
- [28] X. Zhang, Y. Chen, J. Hu, Recent advances in the development of aerospace materials, *Progress in Aerospace Sciences* 97 (2018) 22-34.
- [29] S.R. Soundararajan, J. Vishnu, G. Manivasagam, N.R. Muktinutalapati, *Processing of Beta Titanium Alloys for Aerospace and Biomedical Applications, Titanium Alloys-Novel Aspects of Their Manufacturing and Processing*, IntechOpen 2018.
- [30] H. Schwab, F. Palm, U. Kühn, J. Eckert, Microstructure and mechanical properties of the near-beta titanium alloy Ti-5553 processed by selective laser melting, *Materials & Design* 105 (2016) 75-80.
- [31] E. Eisenbarth, D. Velten, M. Müller, R. Thull, J. Breme, Biocompatibility of β -stabilizing elements of titanium alloys, *Biomaterials* 25(26) (2004) 5705-5713.
- [32] M.F. Semlitsch, H. Weber, R.M. Streicher, R. Schön, Joint replacement components made of hot-forged and surface-treated Ti-6Al-7Nb alloy, *Biomaterials* 13(11) (1992) 781-788.
- [33] M. Semlitsch, F. Staub, H. Weber, Titanium-Aluminium-Niobium alloy, *Development for biocompatible, high strength surgical implants-Titan-Aluminium-Niob-Legierung, entwickelt für körpervertägliche, hochfeste Implantate in der Chirurgie*, *Biomedizinische Technik/Biomedical Engineering* 30(12) (1985) 334-339.
- [34] A. Biesiekierski, J. Wang, M.A.-H. Gepreel, C. Wen, A new look at biomedical Ti-based shape memory alloys, *Acta Biomaterialia* 8(5) (2012) 1661-1669.
- [35] M. Abdel-Hady, H. Fuwa, K. Hinoshita, H. Kimura, Y. Shinzato, M. Morinaga, Phase stability change with Zr content in β -type Ti-Nb alloys, *Scripta Materialia* 57(11) (2007) 1000-1003.
- [36] M. Geetha, A. Singh, K. Muraleedharan, A. Gogia, R. Asokamani, Effect of thermomechanical processing on microstructure of a Ti-13Nb-13Zr alloy, *Journal of Alloys and Compounds* 329(1-2) (2001) 264-271.
- [37] X. Tang, T. Ahmed, H. Rack, Phase transformations in Ti-Nb-Ta and Ti-Nb-Ta-Zr alloys, *Journal of Materials Science* 35(7) (2000) 1805-1811.
- [38] M. Niinomi, Recent biocompatible metallic materials, *Structural Biomaterials for the 21st Century* (2001) 3-14.
- [39] K. Wang, L. Gustavson, J. Dumbleton, *Titanium '92: science and technology*, Warrendale TMS (1993) 2697.
- [40] S. Steinemann, P. Mausli, S. Szmukler-Moncler, M. Semlitsch, O. Pohler, H. Hintermann, *Beta titanium in the 1990s*. Warrendale, Pennsylvania: The Mineral, Metals and Materials Society (1993) 2689-96.
- [41] D. Kuroda, M. Niinomi, M. Morinaga, Y. Kato, T. Yashiro, Design and mechanical properties of new β type titanium alloys for implant materials, *Materials Science and Engineering: A* 243(1-2) (1998) 244-249.
- [42] T. Ahmed, M. Long, J. Silvestri, C. Ruiz, H. Rack, *Titanium 95: Science and Technology*, ed, PA Blenkinsop, WJ Evans, and HM Flower (London: IoM, 1995) (1996) 1760-1767.
- [43] M. Tane, S. Akita, T. Nakano, K. Hagihara, Y. Umakoshi, M. Niinomi, H. Nakajima, Peculiar elastic behavior of Ti-Nb-Ta-Zr single crystals, *Acta Materialia* 56(12) (2008) 2856-2863.
- [44] Z. Guo, J. Fu, Y. Zhang, Y. Hu, Z. Wu, L. Shi, M. Sha, S. Li, Y. Hao, R. Yang, Early effect of Ti-24Nb-4Zr-7.9 Sn intramedullary nails on fractured bone, *Materials Science and Engineering: C* 29(3) (2009) 963-968.
- [45] M. Tane, T. Nakano, S. Kuramoto, M. Hara, M. Niinomi, N. Takesue, T. Yano, H. Nakajima, Low Young's modulus in Ti-Nb-Ta-Zr-O alloys: Cold working and oxygen effects, *Acta Materialia* 59(18) (2011) 6975-6988.
- [46] Y. Liu, S. Li, H. Wang, W. Hou, Y. Hao, R. Yang, T. Sercombe, L.C. Zhang, Microstructure, defects and mechanical behavior of beta-type titanium porous structures manufactured by electron beam melting and selective laser melting, *Acta materialia* 113 (2016) 56-67.

- [47] Y. Liu, H. Wang, S. Li, S. Wang, W. Wang, W. Hou, Y. Hao, R. Yang, L. Zhang, Compressive and fatigue behavior of beta-type titanium porous structures fabricated by electron beam melting, *Acta materialia* 126 (2017) 58-66.
- [48] L.C. Zhang, Y. Liu, S. Li, Y. Hao, Additive manufacturing of titanium alloys by electron beam melting: a review, *Advanced Engineering Materials* 20(5) (2018) 1700842.
- [49] H.Y. Kim, S. Hashimoto, J.I. Kim, H. Hosoda, S. Miyazaki, Mechanical properties and shape memory behavior of Ti-Nb alloys, *Materials Transactions* 45(7) (2004) 2443-2448.
- [50] X. Zhao, M. Niinomi, M. Nakai, J. Hieda, T. Ishimoto, T. Nakano, Optimization of Cr content of metastable β -type Ti-Cr alloys with changeable Young's modulus for spinal fixation applications, *Acta Biomaterialia* 8(6) (2012) 2392-2400.
- [51] X. Zhao, M. Niinomi, M. Nakai, J. Hieda, Beta type Ti-Mo alloys with changeable Young's modulus for spinal fixation applications, *Acta Biomaterialia* 8(5) (2012) 1990-1997.
- [52] X. Zhao, M. Niinomi, M. Nakai, G. Miyamoto, T. Furuhashi, Microstructures and mechanical properties of metastable Ti-30Zr-(Cr, Mo) alloys with changeable Young's modulus for spinal fixation applications, *Acta Biomaterialia* 7(8) (2011) 3230-3236.
- [53] Z.Z. Fang, J.D. Paramore, P. Sun, K.R. Chandran, Y. Zhang, Y. Xia, F. Cao, M. Koopman, M. Free, Powder metallurgy of titanium—past, present, and future, *International Materials Reviews* 63(7) (2018) 407-459.
- [54] R. German, Titanium powder injection moulding: a review of the current status of materials, processing, properties and applications, *PIM International* 3(4) (2009) 21-37.
- [55] R. German, Progress in titanium metal powder injection molding, *Materials* 6(8) (2013) 3641-3662.
- [56] T. Ebel, V. Friederici, P. Imgrund, T. Hartwig, Metal injection molding of titanium, *Titanium powder metallurgy*, Elsevier 2015, pp. 337-360.
- [57] M. Qian, F.H. Froes, Titanium powder metallurgy: science, technology and applications, Butterworth-Heinemann 2015.
- [58] G. Wen, P. Cao, B. Gabbitas, D. Zhang, N. Edmonds, Development and design of binder systems for titanium metal injection molding: An overview, *Metallurgical and Materials Transactions A* 44(3) (2013) 1530-1547.
- [59] R.M. German, Powder injection molding, (1990).
- [60] D.F. Heaney, Handbook of metal injection molding, Woodhead Publishing 2018.
- [61] A. Dehghan-Manshadi, M. Bermingham, M. Dargusch, D. StJohn, M. Qian, Metal injection moulding of titanium and titanium alloys: Challenges and recent development, *Powder Technology* 319 (2017) 289-301.
- [62] A. Dehghan-Manshadi, D. StJohn, M. Dargusch, Y. Chen, J. Sun, M. Qian, Metal injection moulding of non-spherical titanium powders: Processing, microstructure and mechanical properties, *Journal of Manufacturing Processes* 31 (2018) 416-423.
- [63] H. Ye, X.Y. Liu, H. Hong, Fabrication of metal matrix composites by metal injection molding—A review, *Journal of Materials Processing Technology* 200(1-3) (2008) 12-24.
- [64] F.S. Froes, Advances in titanium metal injection molding, *Powder Metallurgy and Metal Ceramics* 46(5-6) (2007) 303-310.
- [65] A. Devaraj, V.V. Joshi, A. Srivastava, S. Manandhar, V. Moxson, V.A. Duz, C. Lavender, A low-cost hierarchical nanostructured beta-titanium alloy with high strength, *Nature communications* 7 (2016) 11176.
- [66] C. Schulze, M. Weinmann, C. Schweigel, O. Keßler, R. Bader, Mechanical properties of a newly additive manufactured implant material based on Ti-42Nb, *Materials* 11(1) (2018) 124.
- [67] J.D. Paramore, Z.Z. Fang, M. Dunstan, P. Sun, B.G. Butler, Hydrogen-enabled microstructure and fatigue strength engineering of titanium alloys, *Scientific reports* 7 (2017) 41444.
- [68] F. Froes, D. Eylon, Powder metallurgy of titanium alloys, *International Materials Reviews* 35(1) (1990) 162-184.
- [69] C. Liu, X. Tian, H. Tang, H. Wang, Microstructural characterization of laser melting deposited Ti-5Al-5Mo-5V-1Cr-1Fe near β titanium alloy, *Journal of Alloys and Compounds* 572 (2013) 17-24.
- [70] C.-M. Liu, H.-M. Wang, X.-J. Tian, H.-B. Tang, D. Liu, Microstructure and tensile properties of laser melting deposited Ti-5Al-5Mo-5V-1Cr-1Fe near β titanium alloy, *Materials Science and Engineering: A* 586 (2013) 323-329.

- [71] S. Xu, C. Zhou, Y. Liu, B. Liu, K. Li, Microstructure and mechanical properties of Ti-15Mo-xTiC composites fabricated by in-situ reactive sintering and hot swaging, *Journal of Alloys and Compounds* 738 (2018) 188-196.
- [72] Y.J. Liu, S.J. Li, H.L. Wang, W.T. Hou, Y.L. Hao, R. Yang, T.B. Sercombe, L.C. Zhang, Microstructure, defects and mechanical behavior of beta-type titanium porous structures manufactured by electron beam melting and selective laser melting, *Acta Materialia* 113 (2016) 56-67.
- [73] Y.J. Liu, Y.S. Zhang, L.C. Zhang, Transformation-induced plasticity and high strength in beta titanium alloy manufactured by selective laser melting, *Materialia* 6 (2019) 100299.
- [74] C.M. Liu, H.M. Wang, X.J. Tian, H.B. Tang, D. Liu, Microstructure and tensile properties of laser melting deposited Ti-5Al-5Mo-5V-1Cr-1Fe near β titanium alloy, *Materials Science and Engineering: A* 586 (2013) 323-329.
- [75] B. He, J. Li, X. Cheng, H.-M. Wang, Brittle fracture behavior of a laser additive manufactured near- β titanium alloy after low temperature aging, *Materials Science and Engineering: A* 699 (2017) 229-238.
- [76] T. Ebel, O.M. Ferri, W. Limberg, M. Oehring, F. Pyczak, F.P. Schimansky, Metal injection moulding of titanium and titanium-aluminides, *Powder Metallurgy of Titanium: Powder Processing, Consolidation and Metallurgy of Titanium* 520 (2012) 153-160.
- [77] E. Carreño-Morelli, S. Martinerie, C. Jacq, T. Maeder, S. Vionnet-Menot, P. Ryser, Development of pressure sensors by powder technology, *Proceedings, Euro PM2007 European Powder Metallurgy Conference, Toulouse (FR), 2007*, pp. 393-398.
- [78] W. contributors, Metal injection molding, *Wikipedia, The Free Encyclopedia*, 2020.
- [79] W. Limberg, R. Willumeit, F. Pyczak, T. Ebel, Metal injection moulding (MIM) of Ti-6Al-4V HDH-powder with high oxygen content, achieving high strength and high ductility by addition of yttrium, *European Congress and Exhibition on Powder Metallurgy. European PM Conference Proceedings, The European Powder Metallurgy Association*, 2018.
- [80] W. Limberg, T. Ebel, Metal injection moulding of Ti-6Al-4V with yttrium addition, *Key Engineering Materials* 704 (2016) 20-27.
- [81] W. Limberg, T. Ebel, K. Kainer, Addition of rare earth elements to MIM-processed TiAl6V4, *European Congress and Exhibition on Powder Metallurgy. European PM Conference Proceedings, The European Powder Metallurgy Association*, 2014.
- [82] A.A. Hidalgo, T. Ebel, W. Limberg, F. Pyczak, Influence of oxygen on the fatigue behaviour of Ti-6Al-7Nb alloy, *Key Engineering Materials* 704 (2016) 44-52.
- [83] D.P. Zhao, K.K. Chang, T. Ebel, M. Qian, R. Willumeit, M. Yan, F. Pyczak, Titanium carbide precipitation in Ti-22Nb alloy fabricated by metal injection moulding, *Powder Metallurgy* 57(1) (2014) 2-4.
- [84] D. Zhao, K. Chang, T. Ebel, M. Qian, R. Willumeit, M. Yan, F. Pyczak, Microstructure and mechanical behavior of metal injection molded Ti-Nb binary alloys as biomedical material, *Journal of the Mechanical Behavior of Biomedical Materials* 28 (2013) 171-182.
- [85] M. Yan, M. Qian, C. Kong, M.S. Dargusch, Impacts of trace carbon on the microstructure of as-sintered biomedical Ti-15Mo alloy and reassessment of the maximum carbon limit, *Acta Biomaterialia* 10(2) (2014) 1014-1023.
- [86] B. Vrancken, L. Thijs, J.-P. Kruth, J. Van Humbeeck, Microstructure and mechanical properties of a novel β titanium metallic composite by selective laser melting, *Acta Materialia* 68 (2014) 150-158.
- [87] H. Schwab, K.G. Prashanth, L. Löber, U. Kühn, J. Eckert, Selective laser melting of Ti-45Nb alloy, *Metals* 5(2) (2015) 686-694.
- [88] S.L. Sing, W.Y. Yeong, F.E. Wiria, Selective laser melting of titanium alloy with 50 wt% tantalum: Microstructure and mechanical properties, *Journal of Alloys and Compounds* 660 (2016) 461-470.
- [89] H. Schwab, M. Bönisch, L. Giebeler, T. Gustmann, J. Eckert, U. Kuehn, Processing of Ti-5553 with improved mechanical properties via an in-situ heat treatment combining selective laser melting and substrate plate heating, *Materials & Design* 130 (2017) 83-89.
- [90] H. Azizi, H. Zurob, B. Bose, S.R. Ghiaasiaan, X. Wang, S. Coulson, V. Duz, A. Phillion, Additive manufacturing of a novel Ti-Al-V-Fe alloy using selective laser melting, *Additive Manufacturing* 21 (2018) 529-535.

- [91] C. Yang, Z. Zhang, S. Li, Y. Liu, T. Sercombe, W. Hou, P. Zhang, Y. Zhu, Y. Hao, Z. Zhang, Simultaneous improvement in strength and plasticity of Ti-24Nb-4Zr-8Sn manufactured by selective laser melting, *Materials & Design* 157 (2018) 52-59.
- [92] W. Chen, C. Chen, X. Zi, X. Cheng, X. Zhang, Y.C. Lin, K. Zhou, Controlling the microstructure and mechanical properties of a metastable β titanium alloy by selective laser melting, *Materials Science and Engineering: A* 726 (2018) 240-250.
- [93] Y. Liu, Y. Zhang, L. Zhang, Transformation-induced plasticity and high strength in beta titanium alloy manufactured by selective laser melting, *Materialia* 6 (2019) 100299.
- [94] D. Herzog, V. Seyda, E. Wycisk, C. Emmelmann, Additive manufacturing of metals, *Acta Materialia* 117 (2016) 371-392.
- [95] J.J. Lewandowski, M. Seifi, Metal Additive Manufacturing: A Review of Mechanical Properties, *Annual Review of Materials Research* 46(1) (2016) 151-186.
- [96] Y. Liu, S. Li, W. Hou, S. Wang, Y. Hao, R. Yang, T.B. Sercombe, L.-C. Zhang, Electron beam melted beta-type Ti-24Nb-4Zr-8Sn porous structures with high strength-to-modulus ratio, *Journal of Materials Science & Technology* 32(6) (2016) 505-508.
- [97] E. Yasa, J.P. Kruth, Microstructural investigation of Selective Laser Melting 316L stainless steel parts exposed to laser re-melting, *Procedia Engineering* 19 (2011) 389-395.
- [98] R. German, Carbon Control: An important discriminant in Metal Injection Molding, *Powder Metallurgy Technology* (5) (2016) 13.
- [99] D. Zhao, K. Chang, T. Ebel, H. Nie, R. Willumeit, F. Pyczak, Sintering behavior and mechanical properties of a metal injection molded Ti-Nb binary alloy as biomaterial, *Journal of Alloys and Compounds* 640 (2015) 393-400.
- [100] B. Cherukuri, R. Srinivasan, S. Tamirisakandala, D.B. Miracle, The influence of trace boron addition on grain growth kinetics of the beta phase in the beta titanium alloy Ti-15Mo-2.6 Nb-3Al-0.2 Si, *Scripta Materialia* 60(7) (2009) 496-499.
- [101] R.M. German, STATUS OF METAL POWDER INJECTION MOLDING OF TITANIUM, *International Journal of Powder Metallurgy* 46(5) (2010).
- [102] O. Ferri, T. Ebel, R. Bormann, Influence of surface quality and porosity on fatigue behaviour of Ti-6Al-4V components processed by MIM, *Materials Science and Engineering: A* 527(7-8) (2010) 1800-1805.
- [103] Z. He, J. Ma, Densification and grain growth during interface reaction controlled sintering of alumina ceramics, *Ceramics International* 27(3) (2001) 261-264.
- [104] O.M. Ferri, T. Ebel, R. Bormann, Influence of surface quality and porosity on fatigue behaviour of Ti-6Al-4V components processed by MIM, *Materials Science and Engineering: A* 527(7) (2010) 1800-1805.
- [105] O.M. Ferri, T. Ebel, R. Bormann, High cycle fatigue behaviour of Ti-6Al-4V fabricated by metal injection moulding technology, *Materials Science and Engineering: A* 504(1) (2009) 107-113.
- [106] P. Xu, T. Ebel, F. Pyczak, Effects of processing defects on damage tolerance of sintered β titanium alloys under static and dynamic loading, *European Congress and Exhibition on Powder Metallurgy. European PM Conference Proceedings, The European Powder Metallurgy Association, Lisbon, Portugal, 2020.*
- [107] P. Xu, F. Pyczak, M. Yan, W. Limberg, R. Willumeit-Römer, T. Ebel, Tensile toughening of powder-injection-molded β Ti-Nb-Zr biomaterials by adjusting TiC particle distribution from aligned to dispersed pattern, *Applied Materials Today* 19 (2020) 100630.
- [108] O.M. Ferri, T. Ebel, R. Bormann, High cycle fatigue behaviour of Ti-6Al-4V fabricated by metal injection moulding technology, *Materials Science and Engineering a-Structural Materials Properties Microstructure and Processing* 504(1-2) (2009) 107-113.
- [109] W. Limberg, T. Ebel, Metal Injection Moulding of Ti-6Al-4V with Yttrium addition, *Key Engineering Materials* 704 (2016).
- [110] T. Ebel, T. Beißig, S. Ebner, X. Luo, A.B. Nagaram, D. Zhao, Reduction of the embrittlement effect of binder contamination in MIM processing of Ti alloys, *Powder Metallurgy* 60(3) (2017) 157-166.
- [111] Y. Yang, S. Luo, G. Schaffer, M. Qian, Impurity scavenging, microstructural refinement and mechanical properties of powder metallurgy titanium and titanium alloys by a small addition of cerium silicide, *Materials Science and Engineering: A* 573 (2013) 166-174.

- [112] W. Limberg, R. Willumeit-Römer, F. Pyczak, T. Ebel, A. Stark, Enhancement of fatigue-properties of MIM-processed Ti-6Al-4V by addition of yttrium and characterization by in situ X-ray scattering, European Congress and Exhibition on Powder Metallurgy. European PM Conference Proceedings, The European Powder Metallurgy Association, 2017.
- [113] P. Xu, T. Ebel, W. Limberg, A.A. Hidalgo, F. Pyczak, R. Willumeit-Römer, MIM-Processed High-Ductility β -type Ti-Nb-Zr-Y Alloy for Biomaterial Applications, European Congress and Exhibition on Powder Metallurgy. European PM Conference Proceedings, The European Powder Metallurgy Association, Bilbao, Spain, 2018.
- [114] Y. Liu, Y. Liu, B. Wang, J. Qiu, B. Liu, H. Tang, Microstructures evolution and mechanical properties of a powder metallurgical titanium alloy with yttrium addition, *Materials and Manufacturing Processes* 25(8) (2010) 735-739.
- [115] O.M. Ferri, T. Ebel, R. Bormann, The Influence of a Small Boron Addition on the Microstructure and Mechanical Properties of Ti-6Al-4V Fabricated by Metal Injection Moulding, *Advanced Engineering Materials* 13(5) (2011) 436-447.
- [116] Z.Z. Fang, P. Sun, H. Wang, Hydrogen sintering of titanium to produce high density fine grain titanium alloys, *Advanced Engineering Materials* 14(6) (2012) 383-387.
- [117] R. Jaffee, H. Ogden, D. Maykuth, Alloys of titanium with carbon, oxygen and nitrogen, *Transactions of the American Institute of Mining and Metallurgical Engineers* 188(10) (1950) 1261-1266.
- [118] H. Ogden, R. Jaffee, The effects of carbon, oxygen, and nitrogen on the mechanical properties of titanium and titanium alloys, TML Report No. 20, Battelle Memorial Institute, 1995.
- [119] J. Murray, H. Wriedt, The O-Ti (oxygen-titanium) system, *Journal of Phase Equilibria* 8(2) (1987) 148-165.
- [120] E. Baril, L. Lefebvre, Y. Thomas, Interstitial elements in titanium powder metallurgy: sources and control, *Powder Metallurgy* 54(3) (2011) 183-186.
- [121] H. Miura, Y. Itoh, T. Ueamsu, K. Sato, The influence of density and oxygen content on the mechanical properties of injection molded Ti-6Al-4V alloys, *Advances in Powder Metallurgy and Particulate Materials* 1 (2010) 46-53.
- [122] J. Lim, C. McMahan, D. Pope, J. Williams, The effect of oxygen on the structure and mechanical behavior of Aged Ti-8 Wt pct Al, *Metallurgical Transactions A* 7(1) (1976) 139-144.
- [123] M. Yan, H. Tang, M. Qian, Scavenging of oxygen and chlorine from powder metallurgy (PM) titanium and titanium alloys, *Titanium powder metallurgy*, Elsevier2015, pp. 253-276.
- [124] M. Yan, W. Xu, M. Dargusch, H. Tang, M. Brandt, M. Qian, Review of effect of oxygen on room temperature ductility of titanium and titanium alloys, *Powder Metallurgy* 57(4) (2014) 251-257.
- [125] M. Tane, T. Nakano, S. Kuramoto, M. Niinomi, N. Takesue, H. Nakajima, ω Transformation in cold-worked Ti-Nb-Ta-Zr-O alloys with low body-centered cubic phase stability and its correlation with their elastic properties, *Acta Materialia* 61(1) (2013) 139-150.
- [126] M. Niinomi, M. Nakai, M. Hendrickson, P. Nandwana, T. Alam, D. Choudhuri, R. Banerjee, Influence of oxygen on omega phase stability in the Ti-29Nb-13Ta-4.6 Zr alloy, *Scripta Materialia* 123 (2016) 144-148.
- [127] T. Ebel, O. Milagres Ferri, W. Limberg, M. Oehring, F. Pyczak, F.P. Schimansky, Metal injection moulding of titanium and titanium-aluminides, *Key Engineering Materials*, Trans Tech Publ, 2012, pp. 153-160.
- [128] A.A. Hidalgo, T. Ebel, W. Limberg, F. Pyczak, Influence of oxygen on the fatigue behaviour of Ti-6Al-7Nb alloy, *Key Engineering Materials*, Trans Tech Publ, 2016, pp. 44-52.
- [129] N.G. Turner, W. Roberts, *The Fatigue Behaviour of Titanium*, University of Birmingham, 1967.
- [130] H. Liu, M. Niinomi, M. Nakai, S. Obara, H. Fujii, Improved fatigue properties with maintaining low Young's modulus achieved in biomedical beta-type titanium alloy by oxygen addition, *Materials Science and Engineering: A* 704 (2017) 10-17.
- [131] G. Yoder, L. Cooley, T. Crooker, Fatigue crack propagation resistance of beta-annealed Ti-6Al-4V alloys of differing interstitial oxygen contents, *Metallurgical Transactions A* 9(10) (1978) 1413-1420.
- [132] M. Bache, W. Evans, M. McElhone, The effects of environment and internal oxygen on fatigue crack propagation in Ti-6Al-4V, *Materials Science and Engineering: A* 234 (1997) 918-922.

- [133] M. Hagiwara, Y. Kaieda, Y. Kawabe, S. Miura, Fatigue property enhancement of α - β titanium alloys by blended elemental P/M approach, *ISIJ International* 31(8) (1991) 922-930.
- [134] G. Wu, C. Shi, W. Sha, A. Sha, H. Jiang, Microstructure and high cycle fatigue fracture surface of a Ti-5Al-5Mo-5V-1Cr-1Fe titanium alloy, *Materials Science and Engineering: A* 575 (2013) 111-118.
- [135] G. Wu, C. Shi, W. Sha, A. Sha, H. Jiang, Effect of microstructure on the fatigue properties of Ti-6Al-4V titanium alloys, *Materials & Design* 46 (2013) 668-674.
- [136] D.F. Heaney, *Handbook of metal injection molding*, Elsevier 2012.
- [137] J.C. Slater, Atomic radii in crystals, *The Journal of Chemical Physics* 41(10) (1964) 3199-3204.
- [138] R. Jaffee, H. Ogden, D. Maykuth, Alloys of titanium with carbon, oxygen, and nitrogen, *JOM* 2(10) (1950) 1261-1266.
- [139] H. Conrad, Effect of interstitial solutes on the strength and ductility of titanium, *Progress in Materials Science* 26(2-4) (1981) 123-403.
- [140] M. Chandran, P. Subramanian, M.F. Gigliotti, Energetics of interstitial oxygen in β -TiX (X= transition elements) alloys using first principles methods, *Journal of Alloys and Compounds* 571 (2013) 107-113.
- [141] M. Yan, M. Qian, C. Kong, M. Dargusch, Impacts of trace carbon on the microstructure of as-sintered biomedical Ti-15Mo alloy and reassessment of the maximum carbon limit, *Acta Biomaterialia* 10(2) (2014) 1014-1023.
- [142] S.C. Tjong, Y.-W. Mai, Processing-structure-property aspects of particulate-and whisker-reinforced titanium matrix composites, *Composites Science and Technology* 68(3-4) (2008) 583-601.
- [143] W. Weng, A. Biesiekierski, Y. Li, C. Wen, Effects of selected metallic and interstitial elements on the microstructure and mechanical properties of beta titanium alloys for orthopedic applications, *Materialia* (2019) 100323.
- [144] D. Konitzer, M. Loretto, Microstructural assessment of Ti6Al4V-TiC metal-matrix composite, *Acta Metallurgica* 37(2) (1989) 397-406.
- [145] P. Wanjara, R. Drew, J. Root, S. Yue, Evidence for stable stoichiometric Ti₂C at the interface in TiC particulate reinforced Ti alloy composites, *Acta materialia* 48(7) (2000) 1443-1450.
- [146] Z. Chen, Y. Li, M. Loretto, Role of alloying elements in microstructures of beta titanium alloys with carbon additions, *Materials Science and Technology* 19(10) (2003) 1391-1398.
- [147] V. Moisy-Maurice, N. Lorenzelli, C. De Novion, P. Convert, High temperature neutron diffraction study of the order-disorder transition in TiC_{1-x}, *Acta Metallurgica* 30(9) (1982) 1769-1779.
- [148] H. Goretzki, Neutron diffraction studies on titanium - carbon and zirconium - carbon alloys, *physica status solidi (b)* 20(2) (1967) K141-K143.
- [149] D.B. Miracle, H.A. Lipsitt, Mechanical Properties of Fine - Grained Substoichiometric Titanium Carbide, *Journal of the American Ceramic Society* 66(8) (1983) 592-597.
- [150] F. Kafkas, T. Ebel, Metallurgical and mechanical properties of Ti-24Nb-4Zr-8Sn alloy fabricated by metal injection molding, *Journal of Alloys and Compounds* 617 (2014) 359-366.
- [151] M.E. Launey, R.O. Ritchie, On the fracture toughness of advanced materials, *Advanced Materials* 21(20) (2009) 2103-2110.
- [152] L. Huang, L. Geng, H. Peng, Microstructurally inhomogeneous composites: is a homogeneous reinforcement distribution optimal?, *Progress in Materials Science* 71 (2015) 93-168.
- [153] T. Tingskog, F. Larouche, L.-P. Lefebvre, New Titanium Alloy Feedstock for High Performance Metal Injection Molding Parts, *Key Engineering Materials* 704 (2016).
- [154] I. Sabirov, O. Kolednik, R. Valiev, R. Pippan, Equal channel angular pressing of metal matrix composites: effect on particle distribution and fracture toughness, *Acta Materialia* 53(18) (2005) 4919-4930.
- [155] S. Gorsse, D.B. Miracle, Mechanical properties of Ti-6Al-4V/TiB composites with randomly oriented and aligned TiB reinforcements, *Acta Materialia* 51(9) (2003) 2427-2442.
- [156] Z.Z. Fang, P. Sun, Pathways to optimize performance/cost ratio of powder metallurgy titanium—a perspective, *Key Engineering Materials*, Trans Tech Publ, 2012, pp. 15-23.
- [157] J.D. Paramore, Z.Z. Fang, P. Sun, Hydrogen sintering of titanium and its alloys, *Titanium powder metallurgy*, Elsevier 2015, pp. 163-182.
- [158] K. Xia, W. Li, C. Liu, Effects of addition of rare earth element Gd on the lamellar grain sizes of a binary Ti-44Al alloy, *Scripta Materialia* 41(1) (1999).

- [159] S. Bai, Z. Liu, Y. Li, Y. Hou, X. Chen, Microstructures and fatigue fracture behavior of an Al–Cu–Mg–Ag alloy with addition of rare earth Er, *Materials Science and Engineering: A* 527(7-8) (2010) 1806-1814.
- [160] Z. Hu, Y. Zhan, G. Zhang, J. She, C. Li, Effect of rare earth Y addition on the microstructure and mechanical properties of high entropy AlCoCrCuNiTi alloys, *Materials & Design* 31(3) (2010) 1599-1602.
- [161] L. Chen, X. Ma, L. Wang, X. Ye, Effect of rare earth element yttrium addition on microstructures and properties of a 21Cr–11Ni austenitic heat-resistant stainless steel, *Materials & Design* 32(4) (2011) 2206-2212.
- [162] E. Willbold, X. Gu, D. Albert, K. Kalla, K. Bobe, M. Brauneis, C. Janning, J. Nellesen, W. Czayka, W. Tillmann, Y. Zheng, F. Witte, Effect of the addition of low rare earth elements (lanthanum, neodymium, cerium) on the biodegradation and biocompatibility of magnesium, *Acta Biomaterialia* 11 (2015) 554-562.
- [163] Y. Liu, L. Chen, W. Wei, H. Tang, B. Liu, B. Huang, Improvement of ductility of powder metallurgy titanium alloys by addition of rare earth element, *Journal of Materials Science & Technology* 22(4) (2006) 465-469.
- [164] Y. Liu, Y.B. Liu, B. Wang, H. Tang, Rare earth element: is it a necessity for PM Ti alloys?, *Key Engineering Materials*, Trans Tech Publ, 2012, pp. 41-48.
- [165] D. Konitzer, B. Muddle, H. Fraser, A comparison of the microstructures of as-cast and laser surface melted Ti–8Al–4Y, *Metallurgical Transactions A* 14(10) (1983) 1979-1988.
- [166] Y. Chen, F. Kong, J. Han, Z. Chen, J. Tian, Influence of yttrium on microstructure, mechanical properties and deformability of Ti–43Al–9V alloy, *Intermetallics* 13(3) (2005) 263-266.
- [167] F. Kong, Y. Chen, F. Yang, Effect of heat treatment on microstructures and tensile properties of as-forged Ti–45Al–5Nb–0.3 Y alloy, *Intermetallics* 19(2) (2011) 212-216.
- [168] H. Tang, S. Lu, W. Jia, G. Yang, M. Qian, Selective electron beam melting of titanium and titanium aluminide alloys, *International Journal of Powder Metallurgy* 50(1) (2014) 57-64.
- [169] W. Limberg, T. Ebel, Metal Injection Moulding of Ti–6Al–4V with Yttrium addition, *Key Engineering Materials*, Trans Tech Publ, 2016, pp. 20-27.
- [170] M. Bermingham, S. McDonald, K. Nogita, D.S. John, M. Dargusch, Effects of boron on microstructure in cast titanium alloys, *Scripta Materialia* 59(5) (2008) 538-541.
- [171] M. Bermingham, S. McDonald, M. Dargusch, D. StJohn, Grain-refinement mechanisms in titanium alloys, *Journal of Materials Research* 23(1) (2008) 97-104.
- [172] M. Qian, Y. Yang, M. Yan, S.D. Luo, Design of low cost high performance powder metallurgy titanium alloys: Some basic considerations, *Key Engineering Materials*, Trans Tech Publ, 2012, pp. 24-29.
- [173] M. Yan, Y. Liu, Y. Liu, C. Kong, G. Schaffer, M. Qian, Simultaneous gettering of oxygen and chlorine and homogenization of the β phase by rare earth hydride additions to a powder metallurgy Ti–2.25 Mo–1.5 Fe alloy, *Scripta Materialia* 67(5) (2012) 491-494.
- [174] H. Wang, Z.Z. Fang, P. Sun, A critical review of mechanical properties of powder metallurgy titanium, *International Journal of Powder Metallurgy* 46(5) (2010) 45-57.
- [175] R. Gerling, E. Aust, W. Limberg, M. Pfuff, F. Schimansky, Metal injection moulding of gamma titanium aluminide alloy powder, *Materials Science and Engineering: A* 423(1-2) (2006) 262-268.
- [176] T. Okabe, K. Hirota, E. Kasai, F. Saito, Y. Waseda, K. Jacob, Thermodynamic properties of oxygen in RE–O (RE= Gd, Tb, Dy, Er) solid solutions, *Journal of Alloys and Compounds* 279(2) (1998) 184-191.
- [177] G. Thompson, P. Skeldon, X. Zhou, K. Shimizu, H. Habazaki, C. Smith, Improving the performance of aerospace alloys, *Aircraft Engineering and Aerospace Technology* 75(4) (2003) 372-379.
- [178] I. Barin, O. Knacke, O. Kubaschewski, Thermochemical properties of inorganic substances, Springer, Berlin 71 (1977) 38.
- [179] X. Luo, T. Ebel, F. Pyczak, W. Limberg, Y. Lin, Carbide evolution and its potential reduction methods in Ti–22Nb based alloys prepared by metal injection moulding, *Materials Letters* 193 (2017) 295-298.

- [180] L.J. Huang, L. Geng, A. Li, F. Yang, H. Peng, In situ TiBw/Ti–6Al–4V composites with novel reinforcement architecture fabricated by reaction hot pressing, *Scripta Materialia* 60(11) (2009) 996-999.
- [181] L.J. Huang, L. Geng, H. Peng, J. Zhang, Room temperature tensile fracture characteristics of in situ TiBw/Ti6Al4V composites with a quasi-continuous network architecture, *Scripta Materialia* 64(9) (2011) 844-847.
- [182] K. Panda, K.R. Chandran, Synthesis of ductile titanium-titanium boride (Ti-TiB) composites with a beta-titanium matrix: The nature of TiB formation and composite properties, *Metallurgical and Materials Transactions A* 34(6) (2003) 1371-1385.
- [183] K. Morsi, V. Patel, Processing and properties of titanium–titanium boride (TiB w) matrix composites—a review, *Journal of Materials Science* 42(6) (2007) 2037-2047.
- [184] M. Sato, M.A. Sambito, A. Aslani, N.M. Kalkhoran, E.B. Slamovich, T.J. Webster, Increased osteoblast functions on undoped and yttrium-doped nanocrystalline hydroxyapatite coatings on titanium, *Biomaterials* 27(11) (2006) 2358-2369.
- [185] F. Feyerabend, J. Fischer, J. Holtz, F. Witte, R. Willumeit, H. Drücker, C. Vogt, N. Hort, Evaluation of short-term effects of rare earth and other elements used in magnesium alloys on primary cells and cell lines, *Acta Biomaterialia* 6(5) (2010) 1834-1842.
- [186] O.I. Velikokhatnyi, P.N. Kumta, First-principles studies on alloying and simplified thermodynamic aqueous chemical stability of calcium-, zinc-, aluminum-, yttrium-and iron-doped magnesium alloys, *Acta Biomaterialia* 6(5) (2010) 1698-1704.
- [187] G. Obasi, O. Ferri, T. Ebel, R. Bormann, Influence of processing parameters on mechanical properties of Ti–6Al–4V alloy fabricated by MIM, *Materials Science and Engineering: A* 527(16-17) (2010) 3929-3935.
- [188] J. Soyama, M. Oehring, W. Limberg, T. Ebel, K.U. Kainer, F. Pyczak, The effect of zirconium addition on sintering behaviour, microstructure and creep resistance of the powder metallurgy processed alloy Ti–45Al–5Nb–0.2B–0.2C, *Materials & Design* 84 (2015) 87-94.
- [189] W. Limberg, T. Ebel, F. Pyczak, M. Oehring, F.P. Schimansky, Influence of the sintering atmosphere on the tensile properties of MIM-processed Ti 45Al 5Nb 0.2B 0.2C, *Materials Science and Engineering: A* 552 (2012) 323-329.
- [190] M. Holm, T. Ebel, M. Dahms, Investigations on Ti–6Al–4V with gadolinium addition fabricated by metal injection moulding, *Materials & Design* 51 (2013) 943-948.
- [191] P. Xu, F. Pyczak, M. Yan, F. Kong, T. Ebel, Impacts of yttrium on microstructure and tensile properties of biomedical β Ti-Nb-Zr fabricated by metal injection molding, *Materials Science and Engineering: A* 792 (2020) 139816.
- [192] W. Manning, O. Hunter Jr, B. Powell Jr, Elastic properties of polycrystalline yttrium oxide, dysprosium oxide, holmium oxide, and erbium oxide: room temperature measurements, *Journal of the American Ceramic Society* 52(8) (1969) 436-442.
- [193] T. Ebel, V. Friederici, P. Imgrund, T. Hartwig, 19 - Metal injection molding of titanium, in: M. Qian, F.H. Froes (Eds.), *Titanium Powder Metallurgy*, Butterworth-Heinemann, Boston, 2015, pp. 337-360.
- [194] D. Zhao, K. Chang, T. Ebel, M. Qian, R. Willumeit, M. Yan, F. Pyczak, Titanium carbide precipitation in Ti-22Nb alloy fabricated by metal injection moulding, *Powder Metallurgy* 57(1) (2014) 2-4.
- [195] S. Li, B. Sun, H. Imai, K. Kondoh, Powder metallurgy Ti–TiC metal matrix composites prepared by in situ reactive processing of Ti-VGCFs system, *Carbon* 61 (2013) 216-228.
- [196] C. Quinn, D. Kohlstedt, Solid - State Reaction Between Titanium Carbide and Titanium Metal, *Journal of the American Ceramic Society* 67(5) (1984) 305-310.
- [197] W. Pearson, *A Handbook of Lattice spacings and Structures of Metals and Alloys* Pergarnon Press, Oxfrd, 1964.
- [198] H. Ogden, R. Jaffee, The effects of carbon, oxygen, and nitrogen on the mechanical properties of titanium and titanium alloys, Battelle Memorial Inst. Titanium Metallurgical Lab., Columbus, Ohio, 1955.
- [199] T. Ozaki, H. Matsumoto, S. Watanabe, S. Hanada, Beta Ti alloys with low Young's modulus, *Materials Transactions* 45(8) (2004) 2776-2779.

- [200] D. Banerjee, J. Williams, Perspectives on titanium science and technology, *Acta Materialia* 61(3) (2013) 844-879.
- [201] A. International, A.I.A.P.D. Committee, A.I.H. Committee, ASM handbook, ASM International 1992.
- [202] E. Hall, The deformation and ageing of mild steel: III discussion of results, *Proceedings of the Physical Society. Section B* 64(9) (1951) 747.
- [203] N. Petch, The cleavage strength of polycrystals, *Journal of the Iron and Steel Institute* 174 (1953) 25-28.
- [204] Y.-N. Xu, Z.-q. Gu, W. Ching, Electronic, structural, and optical properties of crystalline yttria, *Physical Review B* 56(23) (1997) 14993.
- [205] M. Yan, Microstructural characterization of as-sintered titanium and titanium alloys, *Titanium powder metallurgy*, Elsevier 2015, pp. 555-578.
- [206] S. Balachandran, A. Kashiwar, A. Choudhury, D. Banerjee, R. Shi, Y. Wang, On variant distribution and coarsening behavior of the α phase in a metastable β titanium alloy, *Acta Materialia* 106 (2016) 374-387.
- [207] S. Van Bohemen, A. Kamp, R. Petrov, L. Kestens, J. Sietsma, Nucleation and variant selection of secondary α plates in a β Ti alloy, *Acta materialia* 56(20) (2008) 5907-5914.
- [208] M. Yan, W. Xu, M.S. Dargusch, H.P. Tang, M. Brandt, M. Qian, Review of effect of oxygen on room temperature ductility of titanium and titanium alloys, *Powder Metallurgy* 57(4) (2014) 251-257.
- [209] C. Boehlert, C. Cowen, S. Tamirisakandala, D. McEldowney, D. Miracle, In situ scanning electron microscopy observations of tensile deformation in a boron-modified Ti-6Al-4V alloy, *Scripta Materialia* 55(5) (2006) 465-468.
- [210] S. Li, K. Kondoh, H. Imai, B. Chen, L. Jia, J. Umeda, Y. Fu, Strengthening behavior of in situ-synthesized (TiC-TiB)/Ti composites by powder metallurgy and hot extrusion, *Materials & Design* 95 (2016) 127-132.
- [211] M. Piggott, *Load bearing fibre composites*, Springer Science & Business Media 2002.
- [212] G. Garces, G. Bruno, A. Wanner, Load transfer in short fibre reinforced metal matrix composites, *Acta Materialia* 55(16) (2007) 5389-5400.
- [213] M. Ashby, A. Kelly, *Strengthening methods in crystals*, Elsevier, Amsterdam (1971) 137.
- [214] M. Ashby, *Deformation of Plastically Non-Homogeneous Alloys*, *Strengthening Methods in Crystals*, 1971, 137-192 (1971).
- [215] T. Srivatsan, W. Soboyejo, R. Lederich, Tensile deformation and fracture behaviour of a titanium-alloy metal-matrix composite, *Composites Part A: Applied Science and Manufacturing* 28(4) (1997) 365-376.
- [216] A.A. Wells, *Application of Fracture Mechanics to Yielding Materials*, *Proceedings of the Royal Society of London Series a-Mathematical and Physical Sciences* 285(1400) (1965) 34-&.
- [217] F. Burdekin, M. Dawes, *Conf. on Partica Appl. of Fracture Mech*, to Press, Vessel Tech, 1971.
- [218] A. Wells, Notched bar tests, fracture mechanics and the brittle strengths of welded structures, *British Welding Journal* 12(1) (1965) 2.
- [219] M. Yan, S. Luo, G. Schaffer, M. Qian, Impurity (Fe, Cl, and P)-induced grain boundary and secondary phases in commercially pure titanium (CP-Ti), *Metallurgical and Materials Transactions A* 44(8) (2013) 3961-3969.
- [220] R.O. Ritchie, Mechanisms of fatigue-crack propagation in ductile and brittle solids, *International journal of Fracture* 100(1) (1999) 55-83.
- [221] R.O. Ritchie, The conflicts between strength and toughness, *Nature Materials* 10(11) (2011) 817-822.
- [222] D.P. Zhao, Y.K. Chen, K.K. Chang, T. Ebel, B.J.C. Luthringer-Feyerabend, R. Willumeit-Romer, F. Pyczak, Surface topography and cytocompatibility of metal injection molded Ti-22Nb alloy as biomaterial, *Transactions of Nonferrous Metals Society of China* 28(7) (2018) 1342-1350.
- [223] T. Ebel, O. Ferri, Processing of Ti-15V-3Al-3Sn-3Cr by metal injection moulding, *Proceedings of EuroPM*, 2011, pp. 265-270.
- [224] W. Xu, X. Lu, L. Wang, Z. Shi, S. Lv, M. Qian, X. Qu, Mechanical properties, in vitro corrosion resistance and biocompatibility of metal injection molded Ti-12Mo alloy for dental applications, *Journal of the Mechanical Behavior of Biomedical Materials* 88 (2018) 534-547.

- [225] J.-E. Bidaux, F. Comby, M. Rodriguez-Arbaizar, H. Girard, E. Carreño-Morelli, Powder Injection Moulding of Low Modulus Ti-13Nb-13Zr for Implant Application, European Congress and Exhibition on Powder Metallurgy. European PM Conference Proceedings, The European Powder Metallurgy Association, 2016, pp. 1-6.
- [226] E. Endo, H. Nakayama, H. Kyogoku, Effect of Sintering Conditions on Microstructures and Mechanical Properties of Ti-29Nb-13Ta-4.6 Zr Alloy Fabricated by MIM Process, European Congress and Exhibition on Powder Metallurgy. European PM Conference Proceedings, The European Powder Metallurgy Association, 2016, pp. 1-5.
- [227] R. Shi, V. Dixit, H. Fraser, Y. Wang, Variant selection of grain boundary α by special prior β grain boundaries in titanium alloys, *Acta materialia* 75 (2014) 156-166.
- [228] D. Rowenhorst, A. Lewis, G. Spanos, Three-dimensional analysis of grain topology and interface curvature in a β -titanium alloy, *Acta materialia* 58(16) (2010) 5511-5519.
- [229] R.M. German, Fundamentals of sintering, ASM International, Engineered Materials Handbook. 4 (1991) 260-269.
- [230] D. Zhao, Metal Injection Moulding of Titanium-Niobium alloys for biomedical applications, Ph.D. Thesis (2014).
- [231] P.F. Santos, M. Niinomi, H. Liu, K. Cho, M. Nakai, Y. Itoh, T. Narushima, M. Ikeda, Fabrication of low-cost beta-type Ti-Mn alloys for biomedical applications by metal injection molding process and their mechanical properties, *Journal of the Mechanical Behavior of Biomedical Materials* 59 (2016) 497-507.
- [232] A.B. Nagaram, T. Ebel, Development of Ti-22Nb-Xzr using metal injection moulding for biomedical applications, *Key Engineering Materials*, Trans Tech Publ, 2016, pp. 334-342.
- [233] J. Bidaux, F. Comby, M. Rodriguez-Arbaizar, H. Girard, E. Carreño-Morelli, Powder Injection Moulding of Low Modulus Ti-13Nb-13Zr for Implant Application, European Congress and Exhibition on Powder Metallurgy. European PM Conference Proceedings, The European Powder Metallurgy Association, 2016, pp. 1-6.
- [234] J.E. Bidaux, A.A. Hidalgo, H. Girard, M. Rodriguez-Arbaizar, L. Reynard, J. Chevallier, F. Aeby, J.C. Giachetto, E. Carreño-Morelli, Metal injection moulding of superelastic TiNi parts, *Key Engineering Materials*, Trans Tech Publ, 2016, pp. 173-182.

Journal Paper Publications

Peng Xu, Florian Pyczak, Ming Yan, Wolfgang Limberg, Regine Willumeit-Römer, and Thomas Ebel; Tensile toughening of powder-injection-molded β Ti-Nb-Zr biomaterials by adjusting TiC particle distribution from aligned to dispersed pattern. *Applied Materials Today*, 2020.

Peng Xu, Florian Pyczak, Ming Yan, Fantao Kong, and Thomas Ebel; Impacts of yttrium on microstructure and tensile properties of biomedical β Ti-Nb-Zr fabricated by metal injection molding. *Materials Science & Engineering A*, 2020.

Peng Xu, Florian Pyczak, Wolfgang Limberg, Regine Willumeit-Römer, and Thomas Ebel; Superior fatigue endurance exempt from high processing cleanliness of Metal-Injection-Molded β Ti-Nb-Zr for bio-tolerant applications. *In submission*.

Peng Xu, Florian Pyczak, Wolfgang Limberg, Regine Willumeit-Römer, and Thomas Ebel; A review: Effects of processing defects on fracture resistance of powder metallurgy β titanium alloys under quasi-static and dynamic loading. *In writing*.

Peng Xu, Wolfgang Limberg, Anna-Lena Otte, and Thomas Ebel; Optimizations on the debinding and sintering technologies of β Ti-Nb-Ta alloys processed by Metal-Injection-Molding. *In preparation*.

Conferences

October 2018: EuroPM 2018, Bilbao, Spain.

Presentation and conference paper: MIM-Processed High-Ductility β -Type Ti-Nb-Zr-Y Alloy for Biomaterial Applications

September 2019: PMTi 2019, Salt Lake City, UT, USA.

Presentation: Improving Elongation of MIM-ed β Titanium Alloys by Controlling Carbides Precipitating Evolution

June 2020: WorldPM 2020, Montreal, Canada. *cancelled*

Presentation and conference paper: High Cycle Fatigue Behavior of Metal Injection Molded Metastable Beta Titanium

October 2020: EuroPM 2020, Lisbon, Portugal. *cancelled*

Conference paper: Effects of processing defects on damage tolerance of sintered β titanium alloys under static and dynamic loading

October 2021: EuroPM 2021, Lisbon, Portugal.

Conference paper: Effects of processing defects on damage tolerance of sintered β titanium alloys under static and dynamic loading